On the Dynamics of the Solar Corona

Dissertation
zur Erlangung des Doktorgrades
der Mathematisch-Naturwissenschaftlichen Fakultäten
der Georg-August-Universität zu Göttingen

Vorgelegt von

Marilena C. Mierla

Aus Turburea / Rumänien

Göttingen, 2005

La steaua care-a rasarit
E o cale atat de lunga
Ca mii de ani i-au trebuit
Luminii sa ne-ajunga.

Poate de mult s-a stins in cer
In departari albastre.
Dar raza ei abia acum
Lucii vederii noastre.

M. Eminescu,"La Steaua", 1 Dec. 1886

DEDICATED TO
MY FAMILY

Abstract

Spectroscopic observations of the solar corona in emission lines can provide important information about the physical processes taking place there. The emission profile from forbidden transitions of Fe XIV (5303 Å) and Fe X (6376 Å) contains information on the physical parameters such as temperature, mass motion, turbulence.

The LASCO (Large Angle Spectrometric Coronagraph) C1 instrument, with its field of view from 1.1 to 3 $R_\odot$, on board the SOHO (Solar Heliospheric Observatory) spacecraft has provided unprecedented observations of these spectral lines since launch in December 1995 until June 1998. In the C1 design, a Fabry-Perot interferometer is used as a narrow passband tunable filter. It allows generating a series of images at slightly different wavelengths such that line spectra at any point of the image plane can be assembled. To our knowledge this is the first detailed work using these data.

In this work we used C1 spectral data in order to analyze the dynamics of solar corona. In particular, we studied the emergence of the slow solar wind at activity minimum (1996) and during the ascending phase of the solar cycle (1998). The main findings can be summarized as follows:

● In general the corona in 1998 had higher radiances compared with the corona in 1996.

● We found flows along the line of sight in the range from -10 to 10 km/s.

● The line widths are a measure of "effective temperatures". We found them to be much larger than those temperatures at which Fe X and Fe XIV ions form (1 MK for Fe X and 2 MK for Fe XIV). The excess is due to non-thermal motions (like turbulences, wave motions, etc.).

● In general, the corona in 1998 was "hotter" than the corona in 1996. For the data in 1998 it was noticed that closed magnetic features were cooler than open magnetic features.

● We observed that in general the width of the Fe X line was increasing with radial distance, while for the Fe XIV line it was decreasing.

● Three coronal mass ejections originating at the back side of the Sun could be detected in 1998 by large scale red shifts in the respective coronal regions.

● For coronal streamers, we could also determine substantial flows along the line of sight. As the slow solar wind is supposed to originate from regions associated with streamers, we studied these cases in detail. We found for a certain streamer in March 1998 that it originated in a region on the Sun where both closed (active regions) and open (coronal holes) magnetic fields were nearby. The streamer as seen in LASCO-C2 images changed configuration when strong blue shifts were simultaneously observed by C1. From the geometry and line-of-sight speeds, radial speeds of around 9 km/s at 1.3 $R_\odot$ could be determined.

In the 1996 time period studied here, there existed only one near-equatorial active region flanked by 2 two coronal holes. We found that the plasma flowed at the interface between the active region and the coronal holes.

We conclude that the slow solar wind near activity minimum is emerging at the interface between closed and open magnetic field regions. It is probably released by a magnetic reconnection process. In the case of the streamer in 1998 we conclude that plasma flow emerges from the cusp of the streamer.

Contents

List of Figures

List of Tables

Introduction

Observations of the green and red coronal lines help us to understand better the dynamic of the solar corona. These forbidden lines have been studied intensively in the last years by means of ground-based coronagraphs or during eclipses. In this thesis new observations of these lines done with the LASCO-C1 Fabry-Perot interferometer on board of SOHO are presented.

Spectroscopic observations of the solar corona in emission lines can provide important information about the physical processes taking place there. The emission profile from forbidden transitions of Fe XIV (5303 Å) and Fe X (6376 Å) contains information on the physical parameters such as temperature, mass motion, turbulence. Coronal emission lines at visible wavelengths have been observed using Fabry-Perot techniques or spectrographs during total solar eclipses and with coronagraphs at high altitudes (e.g., Singh 1985; Ichimoto et al. 1995; Hara and Ichimoto 1999). This kind of observations is constrained by scattering effects in the terrestrial atmosphere and rarely goes up to 1.2 $R_\odot$. The LASCO (Large Angle Spectrometric Coronagraph) (Brueckner et al. 1995) C1 instrument, with its field of view (FOV) from 1.1 to 3 $R_\odot$, on board the SOHO (Solar Heliospheric Observatory) spacecraft (Domingo et al. 1995) has provided unprecedented observations of these spectral lines since launch in December 1995 until June 1998. In the C1 design, a Fabry-Perot interferometer is used as a narrow passband, tunable filter. It has the ability to generate a series of images which are separated in wavelength. Such a scan allows an emission line to be characterized as a function of wavelength at each point in an image. The study of the obtained line profiles can be invaluable in:

a) determining the line widths and, hence, ion temperatures over the entire extent of the corona,

b) providing unambiguous evidence of mass flow in the corona from the Doppler shift of the line,

c) providing useful inputs to the 3-dimensional modelling of complex coronal structures.

The studies carried out in this work are done on sets of Fe XIV and Fe X scan data, taken with the C1 interferometer during periods of 1996 and 1998; i.e. during the minimum and the rising phase of solar cycle 23.

Outline of the Thesis

The thesis consists of seven chapters. *The first chapter* is an introduction to the characteristics of the Sun and solar corona as inferred from different wavelengths. In *the second chapter* short notes from the history of coronal spectroscopy are presented, as well as a detailed description of the two forbidden lines (Fe XIV and Fe X). The characteristics of these lines in the solar corona are also shown. In *the third chapter* the LASCO-C1 instrument is introduced with a short description of the optical components. The Fabry-Perot interferometer is presented in detail. *Chapter 4* makes us familiar with the data and the way they were taken. Also a short description of the data pre-processing is shown. In *Chapter 5* we present how the data are reduced. Before

interpreting the data, steps like: calibrating the data, removing all bad pixels, have to be done. We also describe how the profiles are computed and corrected for different influences. In *the next chapter (6)* we discuss the results. We make a comparison between the corona at minimum and maximum of activity, as well as between the active regions and the quiet Sun. We also try to explain by a simple model why the width of the green line decreases with height (a subject still controversial in this field). We present different features we can analyze with spectral data (like CMEs, loops, streamers). Further, we discuss our observations concerning the slow solar wind whose sources are not yet known. Finally, *the last chapter* summarizes the conclusions drawn from the present study.

Chapter 1 The Sun and the Solar Corona

1.1 The Sun, our Star

People have worshipped the Sun and deities who represent the Sun for all of recorded history. Hence, many beliefs and legends have been formed around this worship. It was often adored as god of truth, honesty, virtue, prophecy, intellect, vitality, and fertility. That's why when the solar eclipses (occultation of the solar disk by the moon) occurred the people were deeply impressed. With the advent of modern science, new curiosity has motivated mankind to study solar eclipses, this time as natural phenomena.

Throughout history, the human race has had a special relationship with the Sun. Primitive societies in every continent have worshipped the Sun as the god that provided warmth and made the crops grow. And sometimes, when a solar eclipse occurred they thought it was a sign of disease and death.

Stonehenge, Babylonia, Egypt - each culture developed a unique approach to eclipses. But only the Babylonians discovered the long-range prediction cycle, the S*aros (*a period of approximately 6,585.3 days*)*. An eclipse cycle can also be used to go backward in time. This technique has proven useful to historians in fixing exact dates of past events.

The earliest record of a solar eclipse comes from ancient China. The date of this eclipse, usually given as October 22, 2134 B.C., is not certain. The first certain eclipse is attested in the bible: "`And on that day,' says the Lord God, `I will make the Sun go down at noon, and darken the Earth in broad daylight'." (Amos 8:9) "That day" was June 15, 763 B.C.

In more recent times, astronomers have studied eclipses with increasingly sophisticated techniques. One of the most important results of these early studies was the discovery of an element of the periodic table (helium) during the eclipse of 16th of August 1868.

The invention of the coronagraph (Lyot 1931) allows the study of the solar corona outside eclipses, enormously increasing the availability of data. Later on the scientists sent spacecrafts with appropriate telescopes on board into space. The spectral lines at wavelengths absorbed by the Earth atmosphere can now also be observed. In this way a deep understanding of the Sun and its evolution started to develop.

Less than 5 billion years ago, in a spiral arm of our galaxy, the Milky Way, a small cloud of gas and dust began to compress under its own weight. Density and temperature within the cloud's center (core) became so high to ignite nuclear fusion. This process released tremendous amounts of energy which could then combat the compressing force of gravity; and eventually, the two forces reached equilibrium. The balance of fusion reactions versus gravitational collapse, which occurred in the cloud, formed our Sun.

At a distance of 1 AU (AU=Astronomical Unit ($1.49 \cdot 10^8$ km)) from the Earth, the Sun is a gigantic sphere of gas, with a radius of around $6.96 \cdot 10^5$ km and a mass of around $1.99 \cdot 10^{30}$ kg. Its average density is 1400 kg/m^3 and its rate of energy radiation is of $3.86 \cdot 10^{26}$ W.

The source of all the Sun's energy resides in its *core*. The Sun's core has a very high temperature, more than 15 MK, and the material in the core is very tightly packed. It is a combination of these two properties that creates an environment just right for nuclear reactions to occur.

The transport of energy from the core to the surface of the Sun is done by photons in *the radiative zone* and by convection in *the convective zone*. Throughout the radiative zone, energy, in the form of radiation, is transferred by its interaction with the surrounding atoms. Once out of the radiation zone (d > 0.7 $R_\odot$) the energy, originally produced in the core, is transferred to the surface by convection.

At the top of the convective layer there is a thin layer of around 400 - 500 km: *the photosphere* (the visible surface of the Sun). It is the transition layer between the interior and the outer atmosphere of the Sun, and the only layer of the Sun, which can be seen by human eyes. Energy is transported through the photosphere by radiation. A number of features can be observed in the photosphere with a simple telescope. These features include the dark sunspots (with a temperature of 4500 K), the faculae and small granules. Additional patterns which include supergranules, large-scale flows and oscillations, can be found by studying Doppler shifts of lines arising from the photospheric material.
The higher in the photosphere the lower the temperature is. This implies the decrease of the source function with height. Because the source function decreases outward, an absorption line is formed (Gray, 1992). The absorption lines in the photosphere lines are known as *Fraunhofer lines* (after the name of their discoverer, 1814).

The chromosphere is an irregular layer above the photosphere where the temperature rises to about 20,000° C. At these higher temperatures hydrogen emits light of a reddish color (H-alpha emission). This colorful emission can be seen in prominences that project above the limb of the sun during total solar eclipses. This is what gives the chromosphere its name (color-sphere).

The features seen in the chromosphere, when observed through a spectrograph or a filter, form the chromospheric network of magnetic field elements, bright plages around sunspots, dark filaments across the disk and prominences above the limb.
The chromosphere is also visible in the light emitted by neutral or single ionized atoms such as Ca II, in the violet part of the solar spectrum at a wavelength of 3934 Å (the calcium K line).

Above the chromosphere the temperature raises drastically from the 20,000 Kelvin of the upper chromosphere to sometimes over 2 MK in the corona. This region is called *the transition region*. In simple 1-D models this layer is only 100 km thick.
The light emitted from the transition region is dominated by ions few times ionized (C III-IV, O IV-VI, Si IV-VI, N III-V) which radiate mainly in the ultraviolet region of the solar spectrum that is only accessible from space.

The outermost layer of the Sun is called *the corona*. It gets its name from the crown like appearance evident during a total solar eclipse. The corona stretches far out into space, its expansion being known as the solar wind. The corona is very thin and faint and therefore can be seen from Earth only during a total solar eclipse or by using a coronagraph telescope which

simulates an eclipse by covering the bright solar disk. The shape of the corona is mostly determined by *the magnetic field* of the Sun (see Figure 1.1).
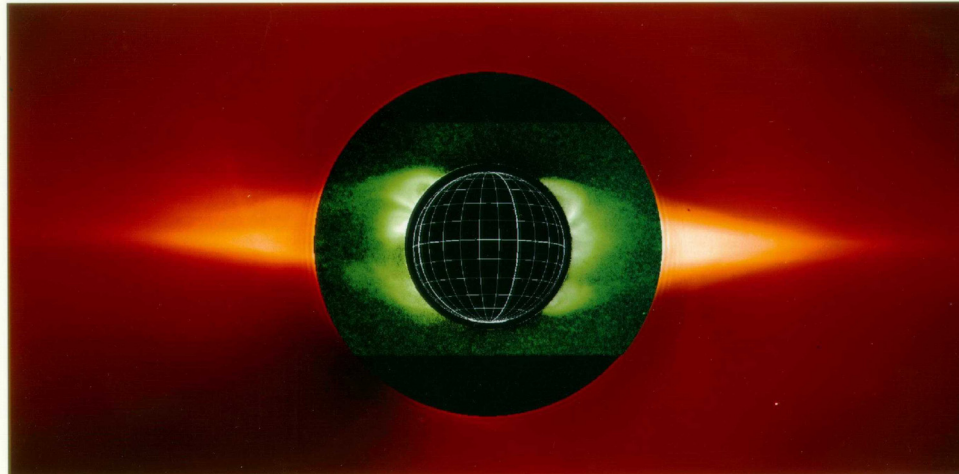
Figure 1.1 The helmet streamers of the corona as seen in a LASCO-C2 image. They are on top of the active regions (AR) represented by three loops structures in the LASCO-C1 image (the inner image).

As the study carried out in this thesis deals mostly with the solar corona and its features, a detailed description is presented in section 2.3.

Due to the high temperatures in the solar corona, the gravity cannot keep the plasma bounded to the Sun. It expands in the interplanetary medium as a continuous stream of particles. The name *"solar wind"* was invented by E. N. Parker in 1958 when developing the theory of the (continuous) solar wind. The existence of solar wind was proven by the Soviet Lunik-2 and 3 probes in 1960 after reaching out from the Earth's magnetosphere. The Mariner-2 probe confirmed the continuous flow of solar wind during its 4-month trip to the planet Venus in 1962. The solar wind is now known to be a mixture of the same elements found in the solar plasma: ionized hydrogen (electrons and protons) with a 4% component of helium (in number density) and trace amounts of heavy ions, plus an equivalent number of electrons. The flux of particles is modulated by the pressure (both magnetic and thermal) at the base of the wind in the solar corona, and to a certain extent, some of the features of the solar wind, particularly in the case of high speed streams, can be identified with specific large scale coronal features, the coronal hole structures.

Ulysses (the first spacecraft flying over the Sun's poles) confirmed what had been found earlier by the Helios solar probes (Physics of the Inner Heliosphere, Ed. R. Schwenn, E. Marsch, 1991, Gringauz et al. 1960, Newugebauer and Snyder 1966) that solar wind comes in two states: slow (~400 km/s) and fast (~ 700 km/s). This "bimodality" of the solar wind is most apparent at solar minimum. The coronal holes (CH) were identified as the source of the fast solar wind in 1973 by observational evidence (Krieger et al. 1973) and by theoretical arguments (Noci 1973). Coronal holes are regions where the corona recorded in hot lines is dark (low temperature). These features were discovered when X-ray telescopes were first flown above the Earth's atmosphere to reveal the structure of the corona across the solar disc. Waldmeier (1957) was among the first to point out that the hot line in visible spectrum, Fe XIV, is missing in coronal holes. Coronal holes are associated with "open" magnetic field lines and are often found at the Sun's poles (Broussard et al. 1978).

For the slow solar wind the origins are not well known. It may come from the boundaries (e.g. Fisk 1996, Suess and Nerney 1999, Ofman 2000) or interior (streamer stalk) (e.g. Bavassano et al. 1997, Habbal et al. 1997, Dahlburg et al. 1998, Strachan et al. 2002) of streamers. Helmet streamers are large cap-like coronal structures with long pointed peaks that usually overlie sunspots and active regions (Pneuman 1968). We often find a prominence or filament lying at the base of these structures. Helmet streamers are formed by a network of magnetic loops that connect the sunspots in active regions and help suspend the prominence material above the solar surface. The closed magnetic field lines trap the electrically charged coronal gases to form these relatively dense structures. It is not yet clear how the closed loops open. It may be the reconnection with the surrounding open magnetic field lines? This is a subject which remains to be investigated.

1.2   The Magnetism of the Sun

Magnetism is the key to understanding the Sun. The magnetic field of the Sun is generated in the convection zone. Sunspots are places where very intense magnetic lines of force break through the Sun's surface. The sunspot cycle results from the recycling of magnetic fields by the flow of material in the interior. The prominences seen floating above the surface of the Sun are supported, and threaded through, with magnetic fields. The streamers and loops seen in the corona are shaped by magnetic fields. Magnetic fields are at the root of virtually all of the features we see on and above the Sun.

1.2.1 Convection Zone

Magnetic fields are produced by electric currents in the convective zone. The Sun itself is a conducting fluid. The temperatures are so high that the atoms within it are mostly ionized. As a result, relative motions between neighboring layers of ionized gas carry currents and spawn magnetic fields. The rotational velocity of the Sun changes suddenly near the convective-radiative boundary. The velocity shear is what drives the so-called solar magnetic dynamo.

1.2.2 The Magnetic Field of the Photosphere

Magnetic features of the photosphere range from the smallest detectable magnetic elements (around 100 km and possibly smaller) to sunspots (up to 50000 km). The magnetic field strength of these features is between 1000 and 2000 Gauss. Due to the requirement of horizontal force balance and exponential decrease of gas pressure with height, the field strength also decreases rapidly with height. Sunspots are associated with strong magnetic fields (Zeeman and Winawer 1910). Furthermore, it is observed that sunspots usually come in pairs, one tending to have a magnetic field polarity that is opposite to that of the other (see Figure 1.2).
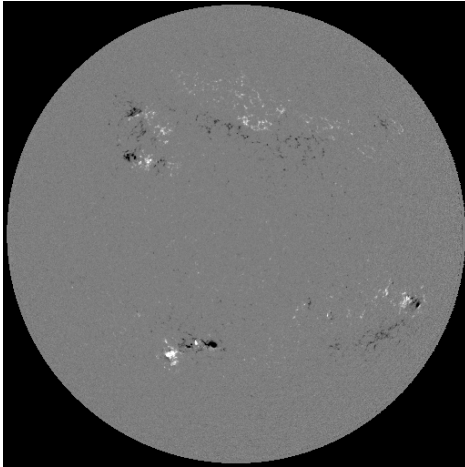
Figure 1.2 Sun magnetogram observed with SOHO/MDI. White represents positive polarities and black negative polarities.

During a given sunspot cycle, the leading sunspots in groups in the northern hemisphere of the Sun tend to have the same polarity, while the same is true for sunspots in the southern hemisphere, except that the polarity of the leading spots is reversed from that of sunspots in the northern hemisphere (see Figure 1.2).

1.2.3 The Magnetic Structure of the Chromosphere

The magnetic structures of the photosphere extend through the chromosphere into the corona (e.g. Kneer and Stolpe 1996). These structures are organized in "flux tubes" with the diameter around 0.3 Mm or less (e.g. Kneer et al. 1996). The exponential decay of gas pressure with height in the chromosphere is not matched by a similar drop-off in magnetic pressure. The magnetic field therefore spreads out laterally with height through the chromosphere, forming a magnetic "canopy" (Jones 1985, Solanki and Steiner 1990).

1.2.4 Coronal Magnetic Field

Direct magnetic field measurements are not available in the solar corona, so the coronal magnetic field must be inferred from remote measurements of photospheric or chromospheric magnetic flux, obtained from line of sight spectroscopic data, together with certain physical assumptions about the coronal plasma. The magnetic field in the solar corona is generally believed to be responsible for a wide range of phenomena — from being the carrier of MHD waves to heat the corona, to producing the gyro-synchrotron radiation in the radio wavelength range (Stix, "The Sun"). It is also the cause of the erupting phenomena (coronal mass ejections (CMEs) for example), (see Figure 1.3).
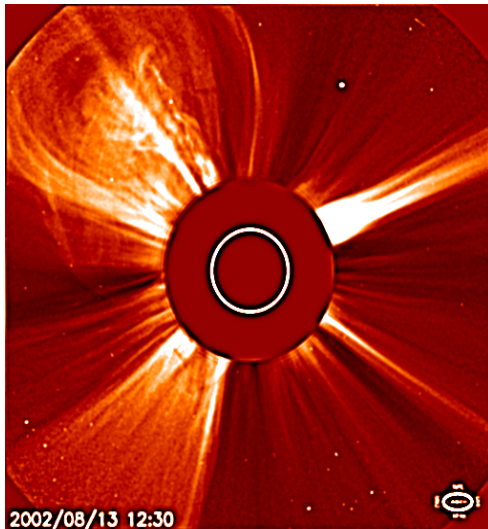
Figure 1.3 A CME observed with LASCO-C2 on 13th of August 2002. The internal structures show the twisted magnetic field. The original image (courtesy of SOHO/LASCO consortium) was processed using wavelet technique (see description in Chapter 5)

1.3   The Solar Corona

The extended outer atmosphere of the Sun is called the corona. It is a million times less bright than the photosphere, so it can only be seen when the disk of the Sun is blocked off in a total solar eclipse or by using a special instrument called coronagraph or with XUV observing methods. The corona displays a variety of features which constantly change with time.

The corona is the Sun's outer atmosphere. The white light corona is visible during total solar eclipses and by means of coronagraphs (in which the disk of the Sun is artificially blocked) (Figure 1.4).
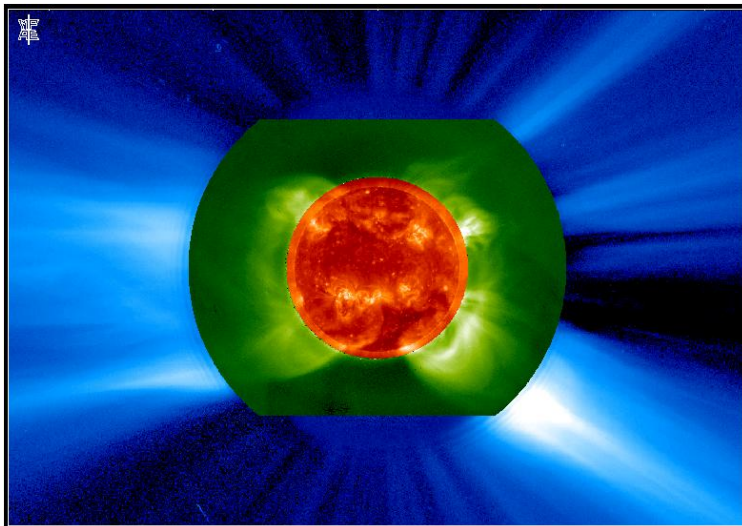
Figure 1.4 The solar corona as seen by three instruments of SOHO (EIT (at center), C1 and C2. The EIT image shows the corona in UV light with the bright regions representing the active regions on the Sun. The LASCO-C1 image is taken in the line of Fe XIV (green part) and shows the ions around the magnetic field lines (loop structures). The LASCO-C2 image (blue part) shows the extended white light corona in the form of rays and helmet streamers.

Although attempts to study the sun's UV spectrum from balloons were made during the 1920s, it was not until 1946 that rocket-borne instruments made this possible (Baum et al. 1946).

Only limited additional progress was made until 1962, when the first Orbiting Solar Observatory (OSO) satellite was launched by the National Aeronautics and Space Administration (NASA). These returned thousands of UV spectra, including the first extreme-ultraviolet (wavelengths

below 2000 Å) observations of the solar corona. Through continuous monitoring of the Sun over a 15-year period, this program enhanced our understanding of the solar atmosphere and of the 11-year sunspot cycle.

The first X-ray picture of the Sun employing a rocket-borne telescope was taken by John V. Lindsay of the NASA Goddard Space Flight Center and collaborators in 1963.

One of the satellites in the OSO series was the piloted Skylab space station, launched in 1973.

The Apollo Telescope Mount (ATM) on Skylab was first full-scale, manned astronomical observatory in space. Eight separate solar telescopes were mounted on the ATM spar. The six principal instruments were two X-ray telescopes, an extreme ultraviolet spectroheliograph, an ultraviolet spectroheliometer, an ultraviolet spectrograph, and a visible light coronagraph. Together they collected data on the Sun in wavelengths from 2 to 7000 Å which spanned the soft X-ray, ultraviolet, and visible light ranges of the electromagnetic spectrum.

In the early 1980s the United States launched the Solar Maximum Mission spacecraft to study the Sun during its most active period. The joint Japanese, U.S., and British probe Yohkoh studied solar flares through the 1990s.

A very productive solar spacecraft launched in December 1995 and operating since January 1996 is the Solar and Heliospheric Observatory (SOHO). All data used for this thesis were obtained from the instruments on SOHO, as described in detail in Chapter 3.

The free electrons in the corona move along magnetic field lines and form many different structures including:

- *helmet streamers* which can be seen as long, spiked cones in solar eclipse (Koutchmy and Livshits 1992) (Figure 1.5) and in coronagraphic images (Figure 1.4),
- *polar plumes:* long thin streamers that project outward from the Sun's north and south poles, associated with the "open" magnetic field lines at the Sun's poles (Figure 1.6),
- *coronal loops:* structures associated with the closed magnetic field lines that connect magnetic regions on the solar surface, (Figure 1.5 and Figure 1.8),
- *coronal holes* (as described above) (see Figure 1.7).
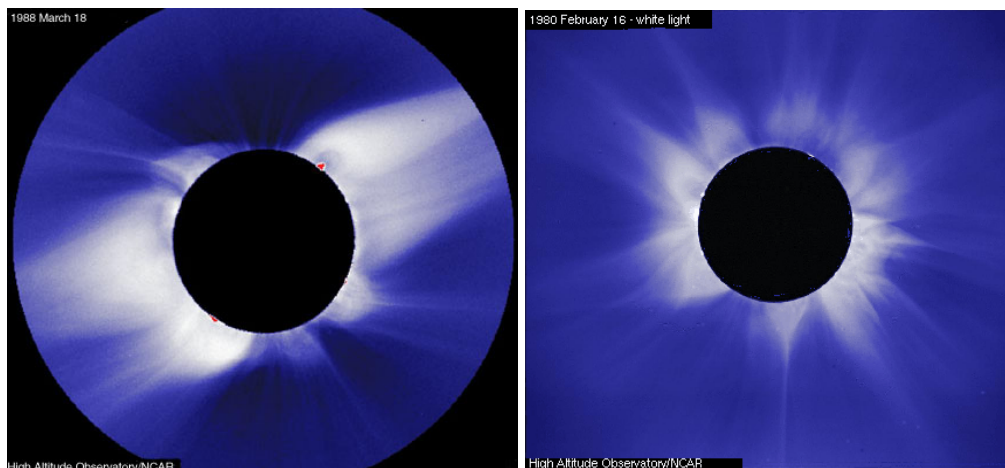
Figure 1.5 The solar corona during the 1988 solar eclipse (left) and the 1980 solar eclipse (right). The 1988 eclipse was near a solar activity minimum and polar coronal holes can be observed. The 1980 eclipse was near a maximum and bright corona is seen all around the Sun. Helmet streamers are observed in both images. (courtesy HAO).

These features change from eclipse to eclipse and the overall shape of the corona changes with the sunspot cycle (see Figure 1.5 and Figure 1.8).
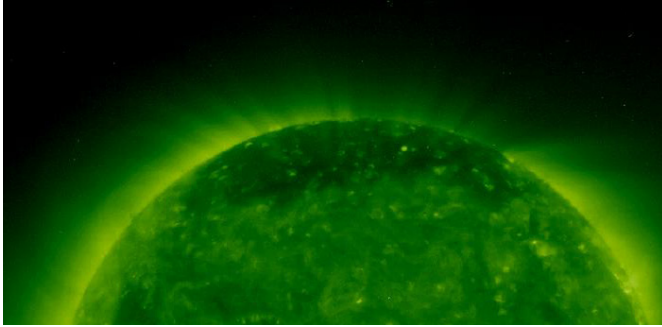
Figure 1.6 Coronal plumes in the 195 Å wavelength as recorded by EIT (courtesy of SOHO/EIT consortium).

Figure 1.7 North pole coronal holes as seen in X-ray image recorded by Yohkoh.
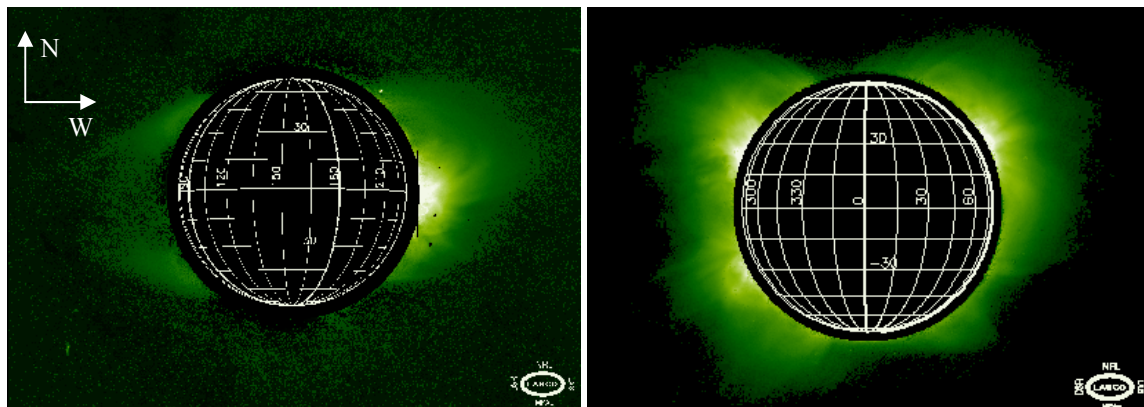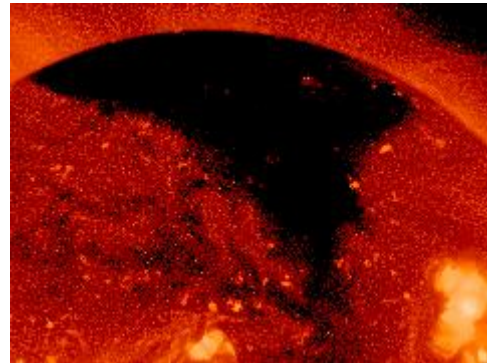
Figure 1.8 The green corona near activity minimum (left) and maximum (right) showing the closed magnetic structures (Wang et al. 1997). The polar coronal holes are observed in the minimum image, by the lack of green radiation. The images are recorded with LASCO-C1 coronagraph on 20th of May 1996, respectively 7th of June 1998.

The solar corona has three components:

K corona – Kontinuum corona

F corona – Fraunhofer corona

E corona – Emission corona

The K component of the corona is the optical radiation as observed during total eclipses (see Figure 1.5). It derives its name from the German "Kontinuum". Its continuous spectrum also resembles the photospheric spectrum, but the Fraunhofer lines are absent. The K corona is the light of the photosphere scattered by the electrons in the corona (Thompson scattering). Due to the high temperature of the electrons, the absorption lines are broadened to a point where they are mixed with the continuum. The K corona structures are tightly linked to the magnetic field of the Sun and their appearance varies with the solar activity.

The F corona (known also as Zodiacal light) dominates outwards from around 2 or 3 solar radii. Its spectrum shows the normal dark Fraunhofer absorption lines of the photospheric spectrum, therefore the name. It can be explained as photospheric light scattered on dust particles. The dust is concentrated towards the ecliptic plane (Stix, "The Sun – An Introduction").

The E component shows the corona in emission lines. Its spectrum is very wide, from radio waves to ultraviolet and X-rays. Shortly, these components are described below:

Emission lines in the visible

In 1942 19 lines were identified by Edlén (Edlén and Swings 1942) as forbidden transitions of highly ionized atoms (one example is shown in Figure 1.8). This will be described in detail in the next section.

Ultraviolet and X-rays

The corona emits a very rich spectrum of UV/EUV lines (Mariska 1992, Mason et al. 1994, Wilhelm and Kalkofen 2003).

Images taken with narrow-band spectral filters tuned to one of these lines exhibit the density distribution of the respective ions (see Figure 1.9). The Extreme ultraviolet Imaging Telescope (EIT) onboard the SOHO satellite monitors the Sun at four different wavelengths: 171 Å, 195 Å, 284 Å, and 304 Å. The lines were selected such that they give information on density distributions at different temperature levels (from the transition region to the lower corona, i.e. from 100 000 K to 2 MK).

Examples of EIT EUV images are shown in Figure 1.9.
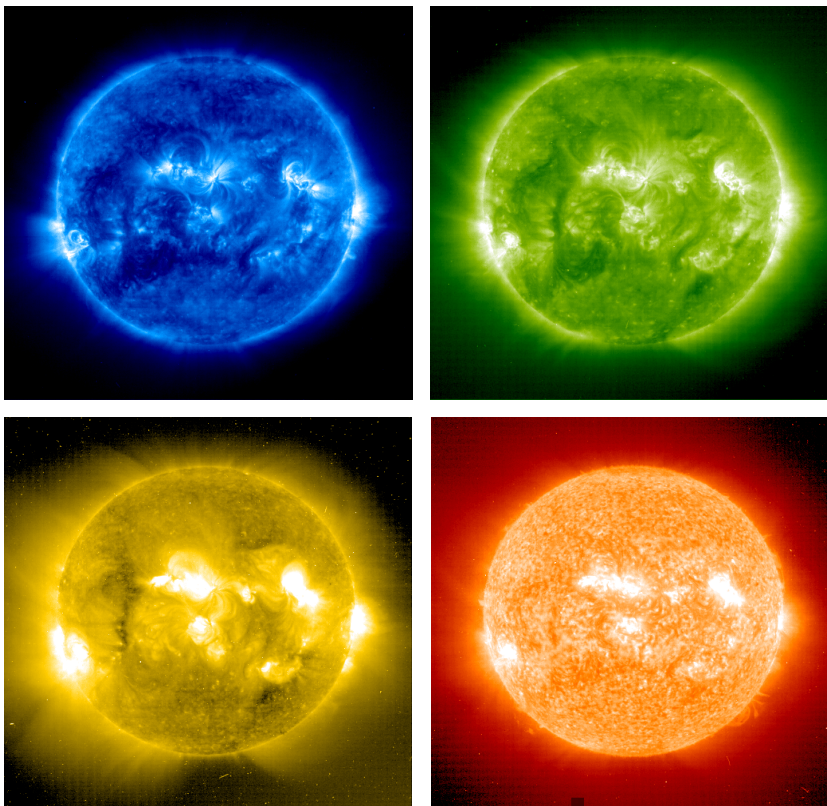
Figure 1.9 EIT images of the full Sun (3rd of November 2004) in spectral ranges of Fe IX, X 171 Å, (blue), Fe XII 195 Å (green), Fe XV 284 Å (yellow), He II 304 Å (red). Coronal holes can be seen on both poles of the Sun (top and bottom). The structure of the corona is controlled by the Sun's magnetic field which forms bright active regions on the solar disc and ray-like structures extended from the coronal holes. (Courtesy of the SOHO EIT consortium).

The 304 and 284 Å images show a portion of the high layers of the chromosphere. In these wavelengths we can sometimes see large prominences rising high above the surface of the Sun. The 195 and 171 Å pictures (EUV) show a part of the low corona. Most of this light comes from

"active regions", where we can sometimes see loops. At the north and south poles of the Sun, less EUV light is emitted - these regions often end up looking dark in the pictures, giving rise to the term "coronal holes."

At the EUV wavelengths, we observe active regions, denoting some of the higher energy phenomena associated with the Sun. These include such features as flares. Brighter regions correspond to the hottest regions.

Profiles of EUV emission lines have been measured with the UV Coronagraph Spectrometer (UVCS) on board of SOHO (Kohl. et al. 1997, 1998) (seeFigure 1.10). Lines measured by UVCS sample the optically-thin plasma along extended regions above the Sun's limb, effectively integrating along the line of sight. Large line widths have been found especially from emission of coronal features having a magnetic field perpendicular to the line of sight, e.g., streamers, helmets or coronal hole regions above the limb.
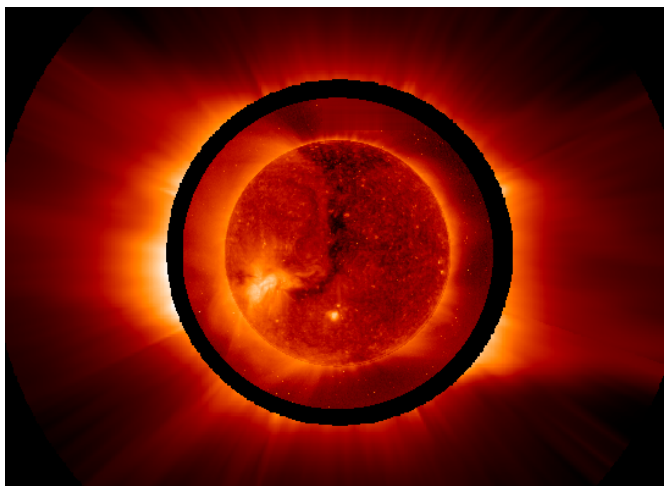
Figure 1.10 The ultraviolet Sun: This composite image, taken by EIT (inner part) and UVCS (outer part) reveals the ultraviolet light of the Sun's atmosphere from the base of the corona to millions of kilometers above the visible disk. The region outside the black circle shines in UV light emitted by oxygen ions. The inner image shows the UV light emitted by iron ions at a temperature near 2 MK. Coronal holes are found on both poles of the Sun (top and bottom) and across the disk of the Sun (so called elephant trunk, as it appeared in August 1996).

High resolution TRACE images in the EUV (171 Å) show bright thin coronal loops above active regions. The finest discernable threads have a width of around 10^6 m, which is close to the resolution limit (see Figure 1.11). That detailed TRACE image indicates that most of the heating of the loops occurs low in the corona, near the bases of the loops as they emerge from and return to the solar disk (Aschwanden et al. 2000, Schrijver et al. 1999).
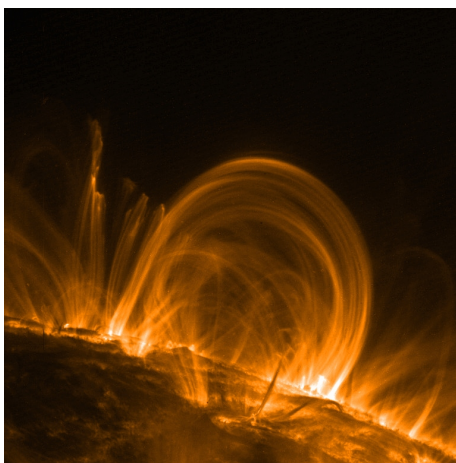
Figure 1.11 The Sun in EUV. In this TRACE image, taken on 6th of November 1999, the hot gas is detected in UV light of Fe IX/X at 17.1 nm, formed at a temperature of about 1 MK. The low corona and transition region are filled with bright, thin magnetized loops. The coronal loops are filled with gas that is hundred times hotter than the photosphere. (Courtesy of Markus J. Aschwanden, the TRACE consortium, LMSAL and NASA).

Spectral atlases have been obtained from the SOHO instruments CDS and SUMER and cover the ranges 30-60 nm and 67-161 nm, respectively (Brekke et al. 2000, Curdt et al. 2001). Due to the high temperatures in the atmosphere, transition region, and corona a wide variety of emission

lines is generated in the UV/EUV range. Each line is characteristic of a specific ion in a specific ionization state. As an example, Figure 1.12 shows the north coronal hole as seen in the light of EUV lines as recorded by SUMER (with the temperature of their peak formation).
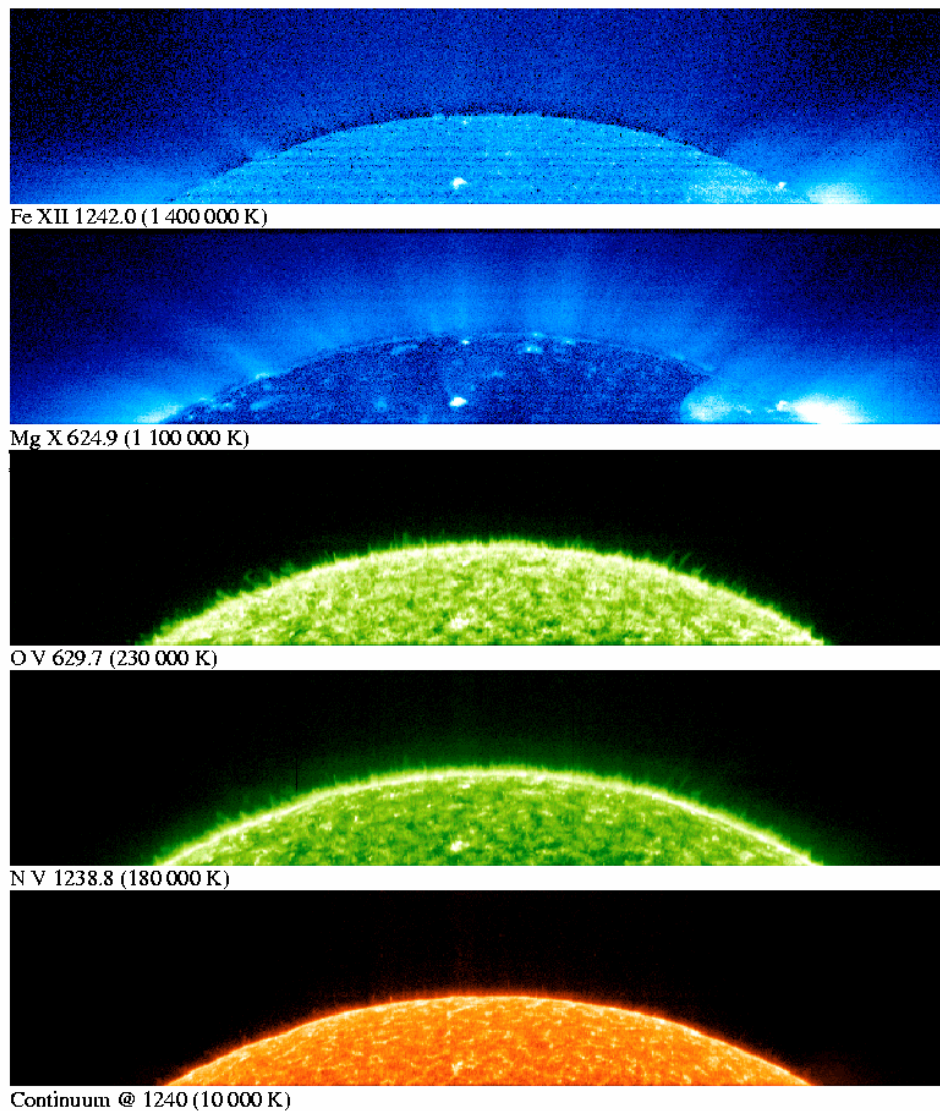
Figure 1.12 The north polar cap of the Sun on 31st of August 1996 seen in four emission lines plus the continuum (last image) with very different formation temperatures from more than 1 MK down to less than 100 000 K. The Mg X (624.9 Å) line shows the dark coronal hole region with bright points. Some of them are the sources of polar plumes, which extend into the corona, presumably along open magnetic field lines. The O V (629.7 Å) line and N V line are characterized by the magnetic network and spicule activity. Very little emission is visible in the Fe XII (1242 Å) line in the upper panel (courtesy of SOHO SUMER consortium).

Numerous coronal X-ray images were taken with the Wolter telescope flown on Skylab in 1973-1974, with the normal incidence X-ray telescope NIST on rocket flights (Golub et al. 1990) and with the soft X-ray telescope of the Yohkoh mission (Figure 1.13).
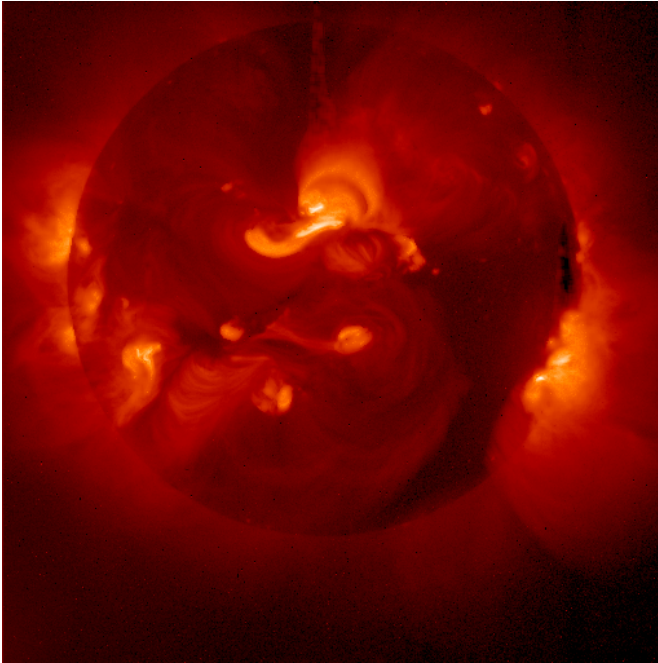
Figure 1.13 The picture of the Sun in X-rays. The image was taken with the Soft X-ray telescope (SXT) on the Yohkoh spacecraft on December, 2001. The X-ray image shows loop-like emission with twisted geometry, as well as bright, compact active regions, coronal loops and relatively faint and long magnetic loops. Dark coronal holes are also seen. (Courtesy of NASA, ISAS, the Lockheed-Martin Solar and Astrophysics Laboratory, National Astronomical Observatory of Japan and University of Tokyo).

The term "X-rays" refers to light with wavelengths shorter than about 10 nanometers. Not all the corona emits the same amount of X-rays. The most visible structures are the loops and arches around the active regions. Movies made from X-ray pictures show that the corona is a very dynamic place, constantly changing and erupting. In these X-ray images one can also see the "coronal holes," regions of low brightness at the north and south poles. Flares are usually discovered first by monitoring the X-ray flux of the corona.

Chapter 2 The Green and Red Corona

2.1 Notes from the History of Forbidden Lines

*It was in the 1860s, when emission lines (particularly a green line) were observed in the coronal spectrum during solar eclipses that did not correspond to any known atomic transition. It was proposed that these were due to an unknown element, provisionally named **coronium**. It was not until the 1930s that it was discovered that these lines were due to highly-ionised iron and nickel, the high ionisation being due to the extreme temperature of the solar corona.*

The term 'spectrum' used to mean 'phantom' or 'apparition', until Isaac Newton introduced a new meaning in 1671, when he reported his experiment of decomposing the white sunlight into colors using a prism. Today, the term 'spectrum' is used for "a display of electromagnetic radiation as a function of wavelength". Several related terms, such as 'spectroscopy' (the study of spectra) and 'spectrograph', have since been introduced into the English language. The term 'continuum' is used to describe spectra that change gradually, like the rainbow. There are also discrete features, called 'emission lines' or 'absorption lines' depending on whether they are brighter or fainter than the neighbouring continuum.

During the total solar eclipse of August 7, 1869 (which was visible from Alaska to North Carolina), Harkness and Young discovered an emission line of feeble radiance in the green part of the white light spectrum of the corona. The eclipses which followed that of 1869 gave evidence of other lines which also could not be satisfactorily identified and were thought to have some relation to the green line in question. Certain groups of these lines had wavelength ratios which served to strengthen the assumption that they arose from a common substance.

Reliable spectral observations were not obtained until 1893. At the time of the eclipse of 1898, measurements of the green line showed that for the past thirty years identity had been assumed with the chromospheric line 1474 at 5316.8 Å while in reality the green coronal line was approximately 14 Å units toward the violet end of the spectrum at about 5303 Å. This more accurate determination of the wavelength of the line due to a hypothetical element called *"coronium"* was made possible by using instruments of better definition and higher dispersion.

During the next few years many observations were made especially by English and by American astronomers in an effort to obtain better determinations of the wavelength of the coronal lines and in particular the line at 5303 Å. Lyot in 1930 and 1931 developed the first coronagraph that allowed him to observe the green line without an eclipse at a high altitude at Pic du Midi. He obtained a value of 5303.2±1 Å and in 1935 a more precise value of 5302.8 for the green line.

The big breakthrough occurred when Grotrian (1939) showed that two of the observed coronal lines correspond to forbidden transitions of the Fe X and Fe XI ions. Grotrian based his calculations on measurements made by the Swedish spectroscopist B. Edlén (1936, 1937). Edlén proceeded to identify further 17 coronal lines, all of them emitted by highly ionized atoms (among them: Fe XIV and Fe X). Hence, Grotrian and Edlén showed that the strange coronal lines are emitted by elements such as iron, calcium and nickel in very high stages of ionization.

The presence of these ions unequivocally indicated temperatures in the corona of at least one million degrees, necessary for the formation of these ions.

2.2 Solar Plasma Diagnostics

The transition from excited metastable states to the ground state of an atom produces what is called forbidden lines. These transitions take place much more slowly than the allowed transitions. Under most conditions, collisions de-excitate the metastable state before it loses energy by a radiative process. Hence, forbidden lines usually are produced when gas densities are low, so that the chances of collision are small during the time interval between excitation and radiative de-excitation.

2.2.1 Line Emissivity

An atom in an excited state (u) can decay spontaneously to a lower energy state (l) and the difference of energy between the two states $\Delta E = \dfrac{hc}{\lambda_{ul}}$ is carried away by a photon of wavelength of λ_{ul}.

At the densities typical of the solar corona ($< 10^9$ cm^{-3}) the plasma is optically thin. In these conditions the line emission from a given volume element, at a given wavelength in the solar corona (erg cm^{-3}s^{-1}Å^{-1}) is given by (2.1) (Teriaca, 2001):

$$E(\lambda)_{lu} = \frac{hc}{\lambda_{lu}} \cdot N_u \cdot A_{ul} \cdot \Psi(\lambda) \tag{2.1}$$

where N_u is the population density of the upper level and A_{ul} is the spontaneous transition probability.

$\psi(\lambda)$ is the emission profile normalized to unity when integrated over all wavelengths.

The total emissivity (erg cm^{-3}s^{-1}) is given then by:

$$E_{lu} = \frac{hc}{\lambda_{lu}} \cdot N_u \cdot A_{ul} \tag{2.2}$$

The formula above is valid for optically thin plasmas (i.e. when the probability that the emitted photon interacts with other atoms before escaping from the plasma is negligible).

Another way to write the total emissivity is:

$$E_{lu} = \frac{hc}{\lambda_{lu}} \cdot \frac{N_u}{N_{ion}} \cdot \frac{N_{ion}}{N_{el}} \cdot \frac{N_{el}}{N_H} \cdot \frac{N_H}{N_e} \cdot N_e \cdot A_{ul} \tag{2.3}$$

- $\dfrac{N_u}{N_{ion}}$ is the fraction of ions in the upper emitting level u. It is weakly dependent on temperature but can be strongly dependent on the electron density.

- $\dfrac{N_{ion}}{N_{el}}$ is the relative abundance of the ionic species with respect to the number density of the element to which the ion belongs. It has a strong dependence of temperature.

- $\dfrac{N_{el}}{N_H}$ is the element abundance with respect to the hydrogen.

- $\dfrac{N_H}{N_e}$ is the hydrogen number density relative to the electron number density. For totally ionized plasmas this number is 0.85 (Feldman et al. 1992).

The observed line radiance is given then by:

$$I_\lambda = \int E_\lambda dl \tag{2.4}$$

As we mentioned in the introduction, the upper solar atmosphere is a very hot (one million K) and low density plasma (less then 10^9 cm^{-3}). Most atoms are fully ionized under these conditions. The atomic processes which excite the upper levels of forbidden lines are radiative excitation (the ions are excited by photons from the photosphere, de Boer 1972) and collisional excitation by electrons.

Once in the excited level, the atoms emit by spontaneous transitions.

2.2.2 Emission Line Profiles

Spectrum lines are not infinitesimally narrow; they have a finite width. A graph of radiance per unit wavelength (or frequency) versus wavelength (or frequency) is the line profile. There are several causes of line broadening, some internal to the atom, others external, and each produces its characteristic profile. Some types of profile, for example, have a broad core and comparatively narrow wings; others have a narrow core and extensive, broad wings. Analysis of the exact shape of a line profile may give us information about the physical conditions, such as temperature and pressure, in the solar atmosphere.

As we mentioned in Equation (2.1), the emission profile is given by:

$$E(\lambda)_{lu} = \frac{hc}{\lambda_{lu}} \cdot N_u \cdot A_{ul} \cdot \Psi(\lambda) \tag{2.5}$$

The emission line profile, $\Psi(\lambda)$, is formed by the convolution of all the emission profiles generated by the different broadening mechanisms:

$$\Psi(\lambda) = \Psi(\lambda)_{nat} * \Psi(\lambda)_{coll} * \Psi(\lambda)_{th} * \Psi(\lambda)_{nt} \tag{2.6}$$

where $\Psi(\lambda)_{nat}$ is the natural broadening

$\Psi(\lambda)_{coll}$ is the collisional (pressure or Stark) profile

$\Psi(\lambda)_{th}$ is the thermal or Doppler profile

$\Psi(\lambda)_{nt}$ is the non-thermal profile.

Natural broadening ($\Psi(\lambda)_{nat}$) arises from the widths of the energy states involved in the transition. The finite duration of the radiation process of electron transition leads to a finite width of line, in accordance with Heisenberg's uncertainty principle:

$$\Delta E \cdot \Delta t \geq \frac{h}{2\pi} \tag{2.7}$$

Natural broadening leads to a Lorentzian emission profile:

$$\Psi(\lambda)_{nat} = \frac{1}{\pi} \cdot \frac{\dfrac{\Delta(\lambda)_{nat}}{2}}{(\lambda - \lambda_0)^2 + \left(\dfrac{\Delta(\lambda)_{nat}}{2}\right)^2} \tag{2.8}$$

The collisional broadening leads also to a Lorentzian profile.

For atomic spectra in the visible and UV, the limit of spectral resolution is often set by **Doppler broadening** ($\Psi(\lambda)_{th}$). With the thermal motion of the atoms, those atoms traveling toward the detector with a velocity v will have transition frequencies which differ from those of atoms at rest by the Doppler shift. The distribution of velocities can be found from the Boltzmann distribution:

$$n(v)dv = N \cdot \sqrt{\frac{m_0}{2\pi kT}} \cdot e^{-\frac{m_0 v^2}{2kT}} dv \tag{2.9}$$

where N is the total number of atoms, m_0 is the atomic mass and v is the speed along the line of sight, k is the Boltzmann constant and T is the kinetic temperature of the gas.

A Maxwellian velocity distribution gives rise to a Gaussian line profile:

$$\Psi(\lambda)_{th} = \frac{1}{\pi^{1/2} \cdot \Delta\lambda_{th}} \cdot e^{-\frac{(\lambda - \lambda_0)^2}{\Delta\lambda_{th}^2}} \tag{2.10}$$

From here we get a Doppler width of:

$$\Delta\lambda_{th} = \frac{\lambda_0}{c} \cdot \left(\frac{2kT}{m}\right)^{1/2} \tag{2.11}$$

In the equation above we have the thermal speed in the form:

$$v_{th} = \left(\frac{2kT}{m}\right)^{1/2} \tag{2.12}$$

where m is the ion mass, k = Boltzmann constant, $\Delta\lambda_{th}$ is the Doppler width (width at 1/e).

The full width at half maximum (FWHM) is:

$$FWHM = \sqrt{4\ln 2} \cdot \Delta\lambda_{th} \tag{2.13}$$

A more general formula for the Doppler width is:

$$\Delta\lambda_D = \frac{\lambda_0}{c} \cdot \left(\frac{2kT}{m} + \xi^2\right)^{1/2} \tag{2.14}$$

where ξ is a non-thermal velocity parameter (turbulence or waves, assumed to have a Gaussian probability distribution). This results in a **non-thermal broadening** of the line: Ψ_{nt}.

The convolution of thermal broadening with the naturally or collisionally broadened line profile is called Voigt profile. This is the convolution of both Lorentzian and Doppler profiles. It does

not have a simple analytical form. It falls off slower than a Doppler profile, so typically the core is approximately Gaussian while the wings look similar to the Lorentzian profile.

The particle collisions are the cause of **pressure broadening**. It is also called collisional broadening. For a high pressure gas, radiating times can be much greater than the interval between atomic collisions, and this perturbation by colliding atoms causes the premature transition and emission of a photon. The decreased lifetime of the state creates an increased uncertainty in photon energy, thus broadening the emission line. The resulting emission profile is, in many cases, again a Lorentzian profile.

2.3   The Green and Red Line Observations of the Solar Corona

Coronal emission lines at visible wavelengths have been observed using Fabry-Perot techniques or spectrographs during total solar eclipses and with coronagraphs at high altitude or in space. They provide us important information about the physical processes taking place in the solar corona.

The intense forbidden lines of the solar corona are magnetic dipole transitions between levels of ground configuration of highly ionized atoms. They are generally polarized, (Charvin, 1965), especially the green line of Fe XIV (Charvin 1971). The ground configuration of Fe XIV is $3s^2 3p$ and the transition is $^2P_{3/2} - ^2P_{1/2}$. Here we use the spectroscopic notation: $n^{2j+1}l_s$, where n is the principal atomic number, j is the total angular momentum number, l is orbital angular momentum number and s is the spin quantum number. For the orbital momentum we have the notations:

$$
\begin{array}{ccccc}
 & S & P & D & F \\
l = & 0, & 1, & 2, & 3
\end{array}
$$

$j = l \pm s$, where s is $+\dfrac{1}{2}$ or $-\dfrac{1}{2}$.

For Fe X the ground configuration is $3s^2 3p^5$ and the transition is: $^2P_{1/2} - ^2P_{3/2}$.

In the corona, the levels of the ground configuration are populated by collisions with electrons and protons, by cascades (electron impact excitation followed by spontaneous emission via excited configurations), and by absorption of the photospheric continuum radiation. The levels are essentially depopulated by spontaneous emission of radiation. Excitation by radiation is not isotropic and this results in polarization of the emission line (Sahal-Bréchot 1974).

For $R/R_\odot \leq 1.2$ the mode of excitation of Fe X ions is predominantly collisional. Collisional as well as radiative excitation is important for $1.2 < R/R_\odot < 1.4$ whereas beyond $R/R_\odot = 1.4$ radiative excitation becomes dominant (Singh 1985). For Fe XIV the dominant excitation mechanism is collisional in the inner coronal regions (up to $\sim 1.4\ R_\odot$) (Raju 1991).

The radiance of the 2 emission lines can be expressed as:

$E_g = D_g(T) \cdot n^{1.68}$ for the green line and

$E_r = D_r(T) \cdot n^{1.66}$ for the red line

$D(T)$ depends on the chemical abundances and the specific transitions as well as on the electron temperature T (Guhathakurta, 1993). n is the electron density.

In coronal structures the width of the red line increases with height above the limb at a rate of 0.5 – 2.6 mÅ / arsec, whereas the green line width in the same region decreases with height at a rate of 1.2 – 3.4 mÅ / arcsec (Singh et al. 1999, 2002). The explanation the author gives for this behaviour is: "As we move up along the coronal structure, the magnetic field spreads and weakens, and mixing of hotter and cooler plasma may occur due to the existence of large thermal and non-thermal velocities. The mixed plasma at large heights may have an average temperature lower than that of the green line plasma and higher than that of the red line plasma at the bottom of the structure".

The average values of the widths of the green line for different coronal structures range between 0.7 – 0.97 Å with a most probable value of 0.8 Å. For the red line width the range is between 0.73 – 1.06 Å, with a most probable value of 0.8 Å.

The line widths in closed magnetic structures are smaller than those in open field structures in the polar regions (Raju et al. 2000). The width of the green line in both the open and closed structures is almost the same, whereas the width of the red line is larger in the open structures as compared to the closed loop-like structures. Outside coronal holes the Fe XIV line intensity is significantly stronger than the Fe X line intensity at all distances (Esser et al. 1995).

At sunspot maximum, the Fe XIV total intensity is about eight times bigger than at the minimum of activity (Waldmeier 1971). The presence of coronal holes and depletions were found from green line measurements (Fisher and Musman 1975, Fisher 1978).

Chapter 3 The Instrument

The LASCO (Large Angle Spectrometric Coronagraph) on board the SOHO (Solar Heliospheric Observatory) spacecraft has provided unprecedented observations of the corona since launch in 1995 (e.g., Howard et al. 1997, Schwenn et al., 1997, St. Cyr et al. 2000). In the C1 design, a Fabry-Perot interferometer is used as a narrow passband, tunable filter. It has the ability to generate a series of images which are separated in wavelength by intervals of 0.003 nm. Such scans allow emission lines to be characterized as function of wavelength at each point in an image.

3.1 LASCO-C1

The Large Angle Spectrometric Coronagraph (LASCO) on the Solar and Heliospheric Observatory (SOHO) consists of three individual coronagraphs with nested fields of view. The three telescopes comprising LASCO are the C1, with coverage from 1.1 to 3.0 $R_\odot$, the C2, extending from 2.0 to 6.0 $R_\odot$, and the C3, which spans the outer corona from about 3.7 to 32 $R_\odot$.

The C1 instrument is a newly developed mirror version of the classic Lyot internally occulted coronagraph, while the C2 and C3 are externally occulted instruments. C1 is equipped with a Fabry-Perot interferometer that allows spatially resolved high-resolution coronal spectroscopy in selected spectral ranges.

The C1 coronagraph observes the solar corona from 1.1 to 3 $R_\odot$ (Brueckner et al. 1995). In order to image the corona with high spatial resolution very close to the limb, an internally occulted system is necessary. C1 implements this requirement with a mirror telescope design. The optical layout of C1 is shown in Figure 3.1. The entrance aperture A0 (4.7 cm diameter) allows the full Sun and the corona to illuminate the off-axis parabolic objective mirror M1 (75 cm focal length). A real image of both the Sun and the corona is formed at mirror M2 which acts as a field mirror. The photospheric light is allowed to pass through a hole (equivalent radius 1.1 $R_\odot$) in M2. This light is eliminated from the telescope with the diagonal rejection mirror and a subsequent optical relay. The coronal light is reflected from M2 on to the off-axis parabolic mirror M3. The two parabolic mirrors, M1 and M3, which are placed symmetrically, form segments of a single parabolic mirror and serve to eliminate coma. The field mirror M2 is spherical (242.2 cm radius of curvature). The combination of M1, M2 and M3 produces a real 1:1 image of A0 at the stop A1. The A1 aperture is sufficiently smaller than A0 that light originated at the edge of A0 is intercepted. In this way, A1 functions as a Lyot stop.
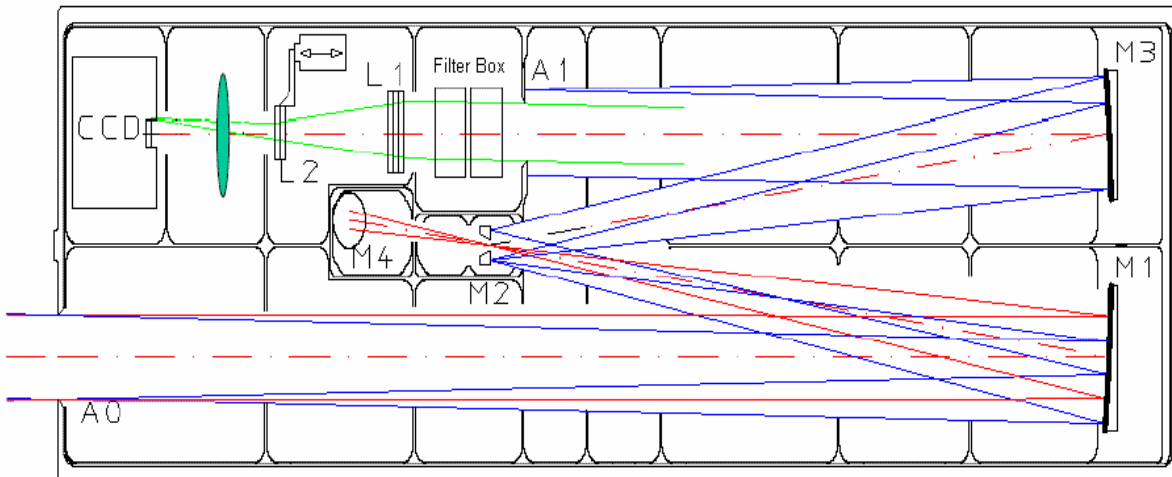
Figure 3.1 The C1 Coronagraph. Red: photospheric light (solar disk), blue: diffracted sunlight at the edges of A0, green: scattered sunlight + corona light

The collimated beam leaving A1 is sent through a narrow-passband tunable Fabry-Perot interferometer. A telephoto lens system (76.8 cm focal length) consisting of 5 lenses forms the actual coronal image. The coronal light passes through a system of broad-band filters and polarizers mounted on two filter wheels. The final image is formed on a CCD camera located behind a mechanical shutterblade. The layout is such that a circular field of view with the radius of 3 $R_\odot$ forms an inscribed circle on the 1024x1024 pixel CCD where one pixel subtends 5.6" in the corona.

The analogue signal is digitized to 14 bits by an analog-to-digital converter, with a quantization step of about 15-20 electrons. The noise of the entire process is less than 10 electrons, so that the entire dynamic range of the system is the full 14 bits, or about 16,000.

3.2   Fabry-Perot Interferometer

The FP is an interference (comb type passband) filter, which passes many interference orders. It works in conjunction with a broader blocking filter, with a passband sufficiently narrow to eliminate all but one selected order passed by the FP, but broad enough to allow tuning of the FP over nearly a full free spectral range (the wavelength range between successive orders). During series of exposures, the FP passband is stepped across a part of the free spectral range to cover a desired spectral line, with the scanning actuated by piezoelectric drivers.

The Fabry-Perot has an intrinsic passband (FWHM) of approximately 0.07 nm, and a free spectral range of 3.5 nm. Therefore the finesse (the ratio of the free spectral range to the spectral passband) is about 50. Cavity length and wedge defect (departure from parallelism) of the interferometer plates are controlled from a microprocessor that uses capacitance micrometers for position sensing. Three piezoelectric transducers determine the cavity length. This combination allows automatic adjustment of wavelength and finesse. The coronal spectrum is referenced to the solar disk Fraunhofer spectrum using three optical control channels, which are located on the perimeter of the interferometer plates.

The coatings of the interferometer plates limit the useful wavelength range to approximately 130 nm. The coating was selected to cover the range from Fe XIV at 530.3 nm to H-alpha at 656.2

nm. Table 3.1 summarizes the available channels using the Fabry-Perot and the appropriate blocking filters.

Channel	Wavelength	Spectral Bandpass	Tunable Range
Fe XIV (emission)	530.3 nm	0.065 nm	±0.76 nm
Ca XV (emission)	569.4 nm	0.059 nm	±0.92 nm
Na I D (Fraunhofer)	589.0 nm	0.072 nm	±0.81 nm
Fe X (emission)	637.4 nm	0.085 nm	±1.06 nm
Hα (emission/absorption)	656.2 nm	0.104 nm	±1.12 nm
White light	530-640 nm	Glass Filter (FWHM = 110.0 nm)	±0.7 nm

Table 3.1 Wavelength bands of the C1 Fabry-Perot interferometer

Table 3.2 lists potential diagnostic methods for use by C1. Coronal temperatures (assuming $T(e) = T(ion)$) can be deduced from line radiance ratios using the three forbidden lines from highly ionised metals, but Ca XV will be useful only in active regions where the temperature is higher. The three lines can also be used in density diagnostic line radiance ratios. Nonthermal velocities can be derived from line profiles, and coronal dynamics from Doppler shifts. Magnetic field directions were thought to be obtained from the Hanle effect polarization in Fe XIV.

Temperature	Intensity ratio	Fe XIV, Ca XV, Fe X
Density	Intensity ratio	Fe XIV, Ca XV, Fe X
Nonthermal velocity	Line width	Fe XIV, Ca XV, Fe X, Hα
Dynamics	Doppler shifts	Fe XIV, Ca XV, Fe X, Hα
Magnetic field direction	Hanle effect, degree and direction of polarization	Fe XIV
Separation of K and F corona	Grotrian method, residual intensities	Na I D
Column densities	Intensity	White light
Outflow	Doppler dimming	Hα

Table 3.2 Fabry-Perot Diagnostics

As we mentioned above, sets of individual monochromatic images can be obtained by scanning over a range of wavelengths around each observed coronal emission line. This is illustrated in Figure 3.2.
The top panel shows the Airy profile of the FP used in C1 for the 530.3 nm line. The lines in black and blue show the transmission profile of the FP without any blocking filters. The parameters of the FP used are given in the table 3.1. The red dashed line shows the blocking filter profile. The resultant filter transmission is given by the product of these two profiles and it is shown in blue color. The middle panel shows an enlarged view of the FP transmission peak at

the line center (within the two dashed lines in the top figure). The dark line indicates the FWHM of the filter (0.07 nm). The line in green is an assumed Lorentzian profile that is similar with the Fe XIV line to be diagnosed. To determine the line profile, the FP pass band is tuned in steps (of 0.03 nm) from the blue side of the emission profile to the red side (lower panel). The reproduced profile, for each pixel in an image, is a convolution of the filter profile and the line profile. In order to reproduce the line profile accurately it is necessary to have a narrow band filter (high spectral resolution) and fine tuning steps.
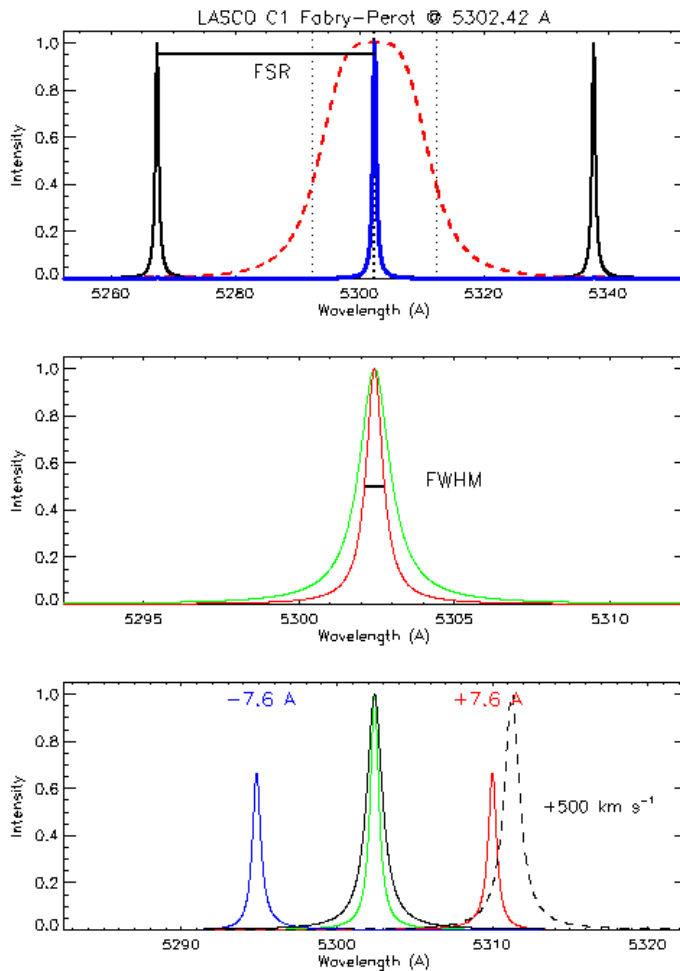
Figure 3.2 **Upper panel:** The FP transmission profile (black) plus the blocking filter profile (red). The blue color is the resultant filter transmission.

Middle panel: Enlarged view of the FP transmission peak at the line center. The dark line: FWHM of the filter (0.065 nm). The green line is a Lorentzian profile with 1.2 Å FWHM.

Lower panel: The filter tuned at 3 different wavelength positions. Blue and red: -0.76 nm, and + 0.76 nm, respectively from line center, green: line center. The dashed, black curve shows the line shifted corresponding to 500 km/s. (Courtesy of S. Mathew).

The tuning range of the FP is +/- 0.76 nm. In terms of Doppler shifts, this range will correspond to velocities of +/- 400 km/s. The dashed curve in Figure 3.2 shows the line for 500 km/s, i.e. beyond the measurement range.

3.3   LASCO Electronics and Image Acquisition

The LASCO and Extreme Ultraviolet Imaging Telescope (EIT) experiments are both controlled by a single electronics unit, the LASCO Electronic Box (LEB). The LEB receives commands from the spacecraft and provides science and housekeeping data to the spacecraft for telemetry. In addition, the LEB contains the power converters used to supply operating voltages to the LEB, the cameras, Fabry-Perot interferometer, pointing eyes and M1 mirror controller. It also controls the experiment operations, manages the interface to the spacecraft computer and performs image processing of the CCD data.

After taking, processing and compressing an image, the data are passed to a 2 Mbyte telemetry buffer. With the telemetry rate allocated to LASCO and EIT together (5.2 Kbs^{-1}), a full buffer will be empty in about one hour.

The major functions of the flight software are command processing, instrument control, image processing and compression, status monitoring and telemetry control. Each of the LEB processors has a small operating system (executive software called LP) that understands a limited number of commands and performs a limited number of control tasks.

Chapter 4 The Observations

Revealing the dynamic nature of the solar corona has made major progress in recent years using modern instrumentation both on the ground and in space. In particular, with advent of the LASCO coronagraphs on SOHO, a new quality of coronal observations could be obtained. The field of view now extends from 1.1 $R_\odot$ (C1) to 30 $R_\odot$ (C3), with sufficient sensitivity to make visible even the almost continuous solar wind outflow in the streamer belt.

4.1 Image Handling and Compression

The three telescopes (C1, C2 and C3) on LASCO use CCD-cameras with 1024x1024 pixels, with a depth of 14 bit. Thus, a full image comprises 2 MB. These images are too big to be sent to the ground base in a fast cadence. In order to make optimum use of the limited telemetry rate image compression is necessary.

In order to compress LASCO images, several techniques are used:
  a) *Occulter* – the image blocks (32x32) pixels that are beyond the field limit or that are occulted by the occulting disk are not transmitted.
  b) *Mask* – an arbitrary pattern can be transmitted by specifying a mask table of image blocks that are not to be transmitted.
  c) *Subregion* – any rectangular subregion of the 1024x1024 CCD may be read out.
  d) *PixSum* – the LASCO Electronic Box (LEB) can perform pixel sums (binning) of any rectangular array of pixels. This feature is also available on the CCD chip itself but is then limited to the dynamic range (14 bits) of the analog-to-digital converter.
  e) *Wavelets* – the images are compressed using wavelet techniques.

The observing programs are:
  a) *Normal* - a single image is taken from a specified telescope (C1, C2, C3, or EIT) for a specified polarizer wheel and filter wheel position. No configuration of the C1 Fabry-Perot (FP) is performed. Thus, this program is used if the FP had already been commanded into the proper state, or if the image did not depend upon the FP configuration.
  b) *FP Scan Line* - an image sequence is taken for a specified polarizer wheel and filter wheel position using the FP at a commanded sequence of wavelength positions needed to build a line profile.
  c) *Polarization Sequence* - A sequence of images is taken from a specified telescope using a single filter wheel position, where for each image the polarizer wheel position is specified. Any filter wheel position of the five available may be used.
  d) *Dark* – For calibration purposes, dark exposures are taken from a specified telescope. The shutter is closed. The mechanical shutter is of the "windmill type". In its closed position, the shutter keeps the CCD dark.
  e) *Flat Fields* – A flat field image is taken keeping the instrument door closed. The C1 door lid contains a quartz diffuser. When the door is closed, attenuated, diffuse light from the solar disk illuminates the aperture and is transmitted through the telescope to the focal lane.

This way, a pure photospheric spectrum containing Fraunhofer lines is obtained for each pixel. Further, the sensitivity of each pixel can be calibrated.

During the whole mission different formats were used. For C1 data a detailed description is given in the next section. For C2 and C3 the most used formats are: the full image: 1024x1024 pixels, corona around the equator (on the minimum of activity): 1024x512 pixels. The filters used are shown in Table 4.1.

Filter	Nominal Bandpass (nm)
Blue	420-520
Orange	540-640
Deep Red	730-835
Clear	400-850
Infrared	860-1050
Hα	2.0 nm centered @ 656.3
3 Polarizers at 120°	400-850

Table 4.1 C2 and C3 filters and polarizers.

4.2   Spectral Observations with LASCO-C1

The Fabry-Perot interferometer in combination with a blocking filter in the C1 instrument transmits only light of a particular wavelength. The wavelength of the light transmitted depends upon the separation of the FP plates and the angle of the light ray with respect to an axis normal to the FP plates.

In order to record an image at a given wavelength, the distance of the FP plates is adjusted accordingly by varying the voltage on three piezoelectric transducers. As the incident light hits the Fabry-Perot etalon at different angles, the transmitted wavelength depends on the position in the field of view (see Figure 4.1). The axis where the light is perpendicular on the camera is called the optical axis of the FP, and the point at which it intercepts the detector is the optical axis intercept (FPAI).
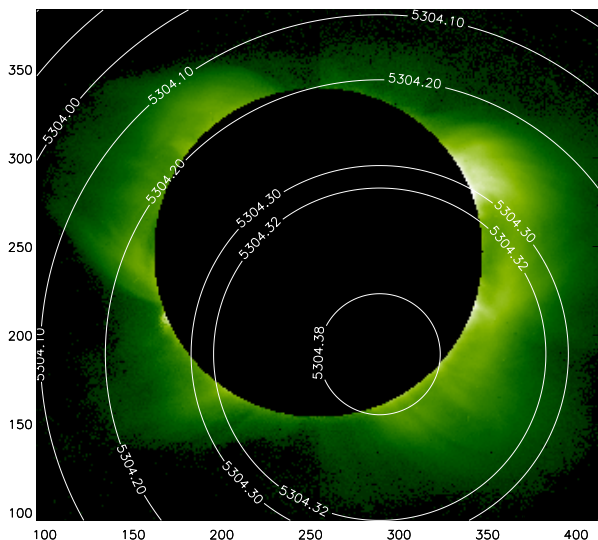
Figure 4.1 The required wavelength correction across the field of view for a wavelength of 5304.36 Å. The wavelengths in the plot are vacuum values. The image is taken on 27th of March 1998.

The correction will be described in detail in Chapter 5 (Data Analysis).

4.3   The Data

The routine data which were taken by C1 were the line-center images and images taken off-line, far from the center of the green emission line and any Fraunhofer absorption line. Full spectral scans were taken usually once per day.

Almost all of the data from C1 are line-center data (around 5303 Å for Fe XIV (green) and 6376 Å (red) for Fe X lines) together with the corresponding off-line images: 5309 Å for the green and 6380 Å for the red line, respectively. This is what we call routine data.

The spectral data were taken almost daily (usually one data set per day), since August 1996 to June 1998, when C1 stopped working. Both the green (5303 Å) and the red (6370.2 Å) lines are analyzed. A data set consists of several on-line images (with the spectral range from 5300 to 5305 Å for the green line, and 6374 to 6378 Å for the red line) and one off-line image (around 5309 Å for the green line and 6380.9 Å for the red line). These wavelengths are listed in the header of every image (fits file).

During the two years and half, LASCO-C1 recorded spectral images in different formats with different exposure times. A detailed description is shown in Table 4.2.

Date	*Xsize (pixels)*	*Ysize (pixels)*	*bin*	*Exp. time (s)*	$\lambda_{on\ min}$ (Å)	$\lambda_{on\ max}$ (Å)	λ_{off} (Å)	$\lambda - step$ (Å)
Aug - Oct 1996	*832*	*672*	*1*	*25*	*5300.90*	*5303.95*	*5309.24*	*0.3*
Oct 1996	*416*	*352*	*2*	*25*	*5300.90*	*5303.95*	*5309.24*	*0.3*
Nov 1996, June 1998	*320*	*320*	*2*	*25*	*5301.20*	*5303.64*	*5309.24*	*0.3*
Nov - Dec 1996, Jan – Mar 1997	*384*	*320*	*2*	*25*	*5301.20*	*5303.64*	*5309.24*	*0.3*
Nov 1996	*512*	*512*	*2*	*25*	*5301.20*	*5303.64*	*5309.24*	*0.3*
Nov - Dec 1996, Jan - Mar 1997	*512*	*320*	*2*	*100*	*5301.51*	*5303.94*	*5309.24*	*0.3*
Nov 1997	*512*	*512*	*2*	*25*	*5300.41*	*5304.79*	*5309.24*	*0.2*
Jan 1998	*512*	*544*	*1*	*25*	*5300.41*	*5304.60*	*no*	*0.4*
Feb 1998	*256*	*256*	*2*	*25*	*5299.70*	*5304.60*	*5309.24*	*0.3*
Mar 1998	*192*	*288*	*2*	*25*	*5299.70*	*5304.60*	*5309.24*	*0.3*
Aug - Sept 1996, Jan 1997	*832*	*672*	*1*	*16*	*6374.11*	*6377.94*	*6380.95*	*0.5*
Sept - Oct 1996	*416*	*352*	*2*	*16*	*6374.24*	*6378.03*	*6380.95*	*0.5*
Oct 1996	*320*	*288*	*1*	*16*	*6374.80*	*6378.08*	*6380.95*	*0.5*
Nov 1996	*320*	*320*	*2*	*16*	*6374.80*	*6378.08*	*6380.95*	*0.5*
Nov - Dec 1996, Jan, Mar 1997	*384*	*320*	*2*	*16*	*6374.80*	*6378.08*	*6380.95*	*0.5*

Table 4.2 C1 spectral scans of Fe XIV (green) and Fe X (red) lines taken during the period August 1996 – June 1998.

The table describes: the date when the spectral data were recorded (first column), the size of the images (second and third columns), the binning (the 4th column), the exposure time as given in the header (5th column), the first and last on-wavelengths in a scan (6th and 7th columns), the off-line wavelength (8th column) and the step width in taking the on-line images in the 9th column.

It is noticed that in 1996 and 1997 both the red and the green line scans are taken every day. For March 1998 Fe XIV scans are taken every hour, for both east and west limb sides. In this period no Fe X line was recorded. The only data sets of this line in 1998 were taken on March (2 data scans) and April (1 data scan).

The green data analyzed in this thesis are:

a) The data of March 1998: Each data set consists of 15 spectral on-line images with the "command" wavelength ranging from 5299.7 to 5304.6 Å and one off-line image taken at the wavelengths of 5309.24 Å. The "command" wavelength is given in the header of every fits file and represents the wavelength at which the instrument was "commanded" to take an image. In this period both east and west scans were taken with a cadence of 1 minute and the exposure time of 25 seconds. In the period of 27-30 March a number of 47 data sets were recorded. Examples of images taken at a given wavelength are shown in Figure 4.2.
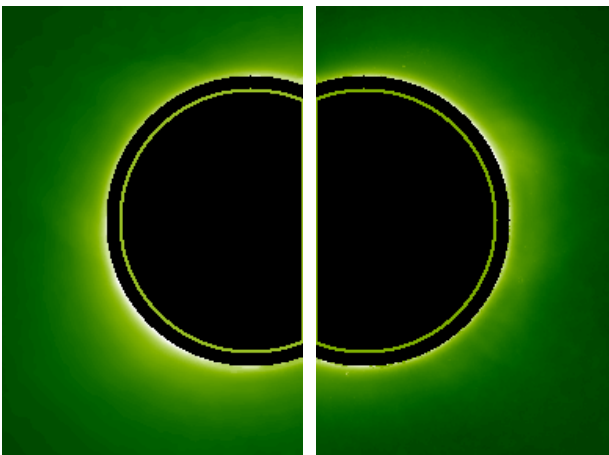
Figure 4.2 Green line images taken with LASCO-C1 at a "command" wavelength of 5302.12 Å on 28th of March, 1998, 01:52, on east (left image), respectively west (right image) side. Bad pixels due to cosmic rays were removed and the CCD bias was subtracted. The radiances are displayed in logarithmic scale.

The 2 images are the row ones. That means that the off line image was not subtracted. Because of this the green corona is not seen. The strong stray light hides the emission corona.

b) The data of August-October 1996: In this case we have only 9 spectral on-line images in a set, ranging from 5300.9 Å to 5303.95 Å and one off-line image taken at a wavelength of 5309.24 Å. In this period a data scan per day was taken, with a cadence of 3 minutes and an exposure time of 25 seconds. In this period 97 data sets were recorded. An example of image taken at a given wavelength is shown in Figure 4.3.
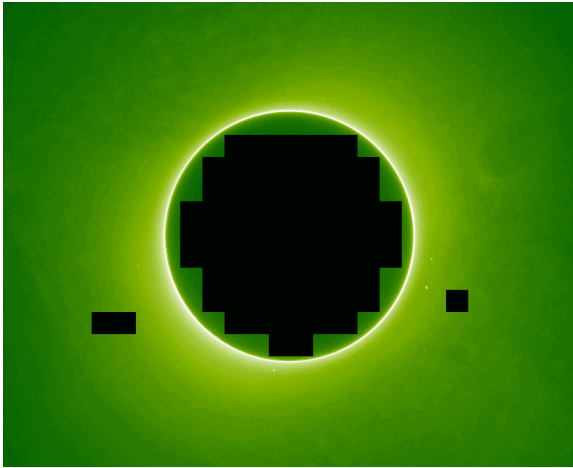
Figure 4.3 Green line image taken with LASCO-C1 at a "command" wavelength of 5302.12 Å, on 1st of August 1996. Bad pixels due to cosmic rays were removed and the CCD bias was subtracted. The radiances are displayed in logarithmic scale. The black regions are the missing blocks in the telemetry.

The red data analyzed here are:

a) The data of 27th of March and 08th of April 1998: They consist of 13 spectral on-line images with the "command" wavelengths ranging from 6374.04 to 6377.64 Å and one off-line image at the wavelength 6385.10 Å. In this period only two scans were taken on March and one scan in April, with a cadence of 1 minute, respective 2 minutes and the exposure time of 16 seconds. An example of an image taken at the "command" wavelength of 6374.94 Å is shown in Figure 4.4.
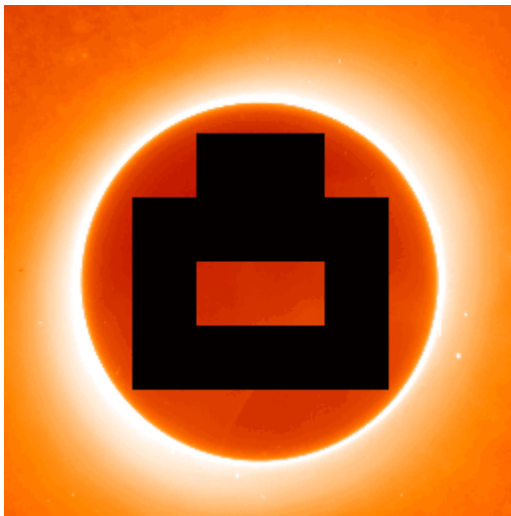
Figure 4.4 Red line image taken with LASCO-C1 at a "command" wavelength of 6374.94 Å on 27th of March, 1998, 15:08. Bad pixels due to cosmic rays were removed and the CCD bias was subtracted. The radiance is displayed in logarithmic scale.

The image looks brighter near the occulter compared with green images because the pixels were 2x2 binned (i.e. 4 adjacent pixels were summed up).

b) The data of August-October 1996: A spectral scan consists of 9 on-line images with the "command" wavelengths ranging from 6374.12 to 6379.04 Å and one off-line image taken at a wavelength of 6380.96 Å. In this period a number of 76 spectral scans were recorded, one scan per day, with a cadence of 8 minutes and exposure time of 16 seconds. An example of an image taken at the "command" wavelength of 6376.17 Å is shown in Figure 4.5.
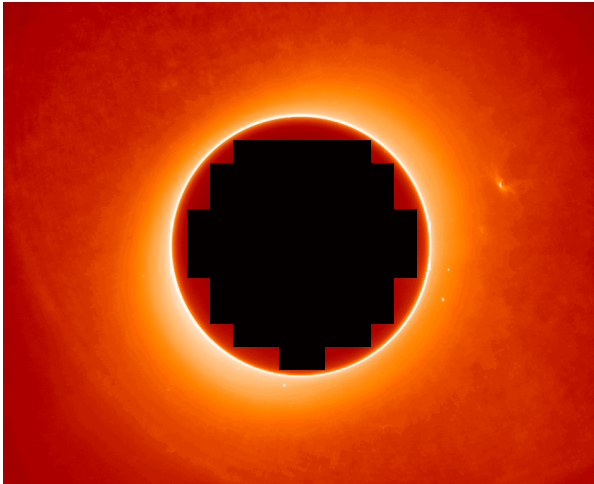
Figure 4.5 Red line image taken with LASCO-C1 at a "command" wavelength of 6376.17 Å on 06th of August, 1996. Bad pixels due to cosmic rays were removed and the CCD bias was subtracted. The radiance is displayed in logarithmic scale.

The image above is a subframe of the big 1024x1024 frame. These kinds of images were taken many times in order to save telemetry.

Chapter 5 Data Analysis

Before the emission line profiles can be evaluated, some standard procedures of data reductions need to be applied. Also, the influences of instrumental scattered light (which is dominated by three nearby Fraunhofer absorption lines for Fe XIV data) are removed. After properly fitting the measured spectra using Gaussian line profiles, the emission line characteristics are determined for the whole field of view and radiance, Doppler shift and line width maps are computed.

5.1 Standard Data Reductions

The LASCO-C1 coronal images used in this analysis are "level 0.5 images", i.e., raw images that have been rotated to put the solar north at the top of the image. The image data are available as FITS files at the MPS (Max-Planck Institute for Solar System Research) archive. The image headers give detailed information on the format of the images, the exposure time, and the corrections which were already applied. The corrections for instrument response, stray light, etc. are not yet done. The radiances are given in units of DN (digital numbers or counts).

In order to reduce the C1 data some preparatory steps are needed:

a) An amplifier offset bias is subtracted from the images. This bias had been added before the signal was converted from analog to digital, in order to avoid negative values. The bias value for the C1 detector has been found to be slowly increasing with time (see Figure 5.1). Calculation of the actual LASCO-C1 offset bias has been done using dark images for various days during the mission. The value of the offset bias for a particular dark image was taken to be the value assumed by the majority of pixels in the image.
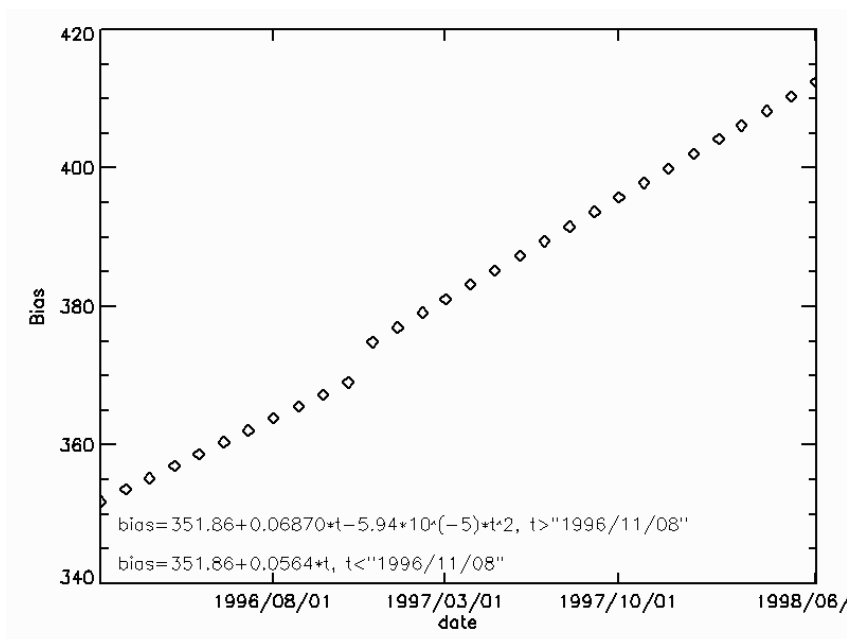
Figure 5.1 The variation of C1 bias in time. The bias was computed using the formulas shown in the figure.

32

b) The occulter mask was also applied. In order to apply the occulter mask (with a radius of 1.1 $R_\odot$) the position of the subframe (see discussions in Chapter 4) on the big frame (1024x1024) has to be known, in order to determine the center of the Sun.

c) The images have a number of randomly distributed pixels that are too bright because of the interaction of cosmic rays with the CCD during the exposure and the readout. These bad pixels were partially removed by using a median filter technique.

d) The images were normalized to the exposure time. This information is given in the header of each FITS file.

e) In order to increase the contrast the wavelet technique is applied to the routine data (see section 5.3).

5.2   Error Analysis

The statistical errors in the brightness of each pixel in a CCD image should be determined by the CCD photoelectron statistics. The number of photoelectrons (N) in each pixel is sufficiently large for the Poisson distribution to approach a Gaussian distribution, meaning the 1 σ uncertainty in these photoelectron counts is simply $\sigma = \sqrt{N}$. Every count (DN) in our data corresponds to 13 photoelectrons (Cook et al. 2000). Thus, the statistical error expressed by the DN numbers is $\dfrac{\sqrt{DN}}{\sqrt{13}}$. Normalisation to counts rates (DN/second) is achieved by dividing the DN numbers by the exposure time.

5.3   Wavelet Technique

In order to better see the coronal features in LASCO images we increase the contrast using a wavelet technique. We apply this technique to the routine data only.

The wavelet technique consists in the decomposition of a 2D image in wavelet scales. When an image is decomposed in wavelet scales, its contents are partitioned into consecutive frequency bands (Stenborg & Cobelli, 2003). The first wavelet planes contain the higher frequency components, while lower frequency signatures are present towards the last scales and on the smoothed array.

Fluctuations due to time varying background and those introduced by noise are not of interest for data restoration as they do not contain relevant information. Their contribution must be reduced to a minimum in order to attain optimum visibility of coronal fine structures. This can be achieved by considering each scale as being another base-level image whose quality is to be enhanced. The splitting algorithm of a wavelet packet analysis is based on this fact and provides a finer analysis of the frequency content of transients at a given scale. Finally, by recombining these planes (having different weights) a very good contrast enhanced image can be obtained. Applications of the technique are shown in Figure 5.2.
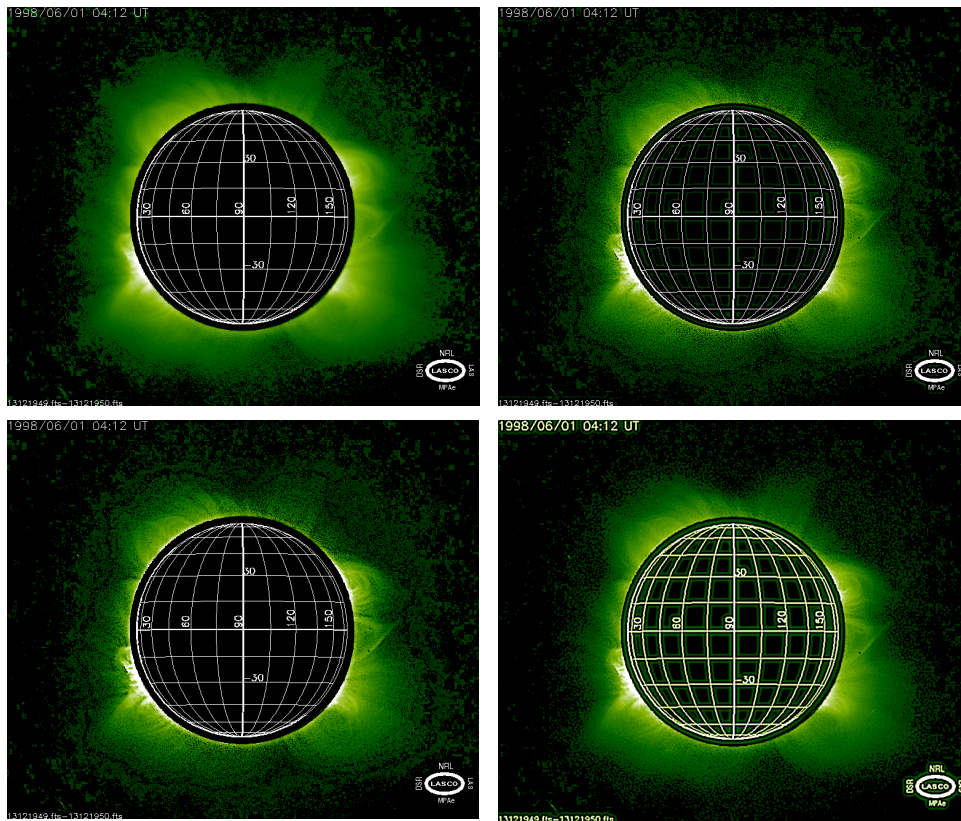
Figure 5.2 Fe XIV green line loops in the inner corona as seen by LASCO-C1 on 01st of June 1998 at 04:12 UT (upper left image) plus three different reconstruction schemes based on an 8 first-level scales plus the smooth array, each scale further subdivided in 4 scales plus continuum. The original image is reduced by subtracting the off-line image from the corresponding on-line image.

The images above show a complex loop system which is very well seen in the wavelet processed images. Three different reconstruction schemes are shown, each revealing different aspects of the solar corona. The upper right and lower left images show the faint fine structures. The inner structure of the loops is well discernable. For these images only the high frequency planes were kept. The lower right image shows the large-scale corona. For this the low-frequency planes were kept.

5.4   Reduction of Routine Data

After applying the corrections explained above, Fe XIV and Fe X images are created from all on-line images by subtracting the off-line images taken nearest in time. Before subtraction, the off-line images are multiplied by a normalization factor of 0.96, in order to correct for different spectral sensitivity of the instrument. These images are treated with wavelet technique (see the previous section) in order to increase the contrast.

Some examples of these data together with the wavelet processed images are shown in Figure 5.3 and Figure 5.4 (Fe XIV) and Figure 5.5 and Figure 5.6 (Fe X).
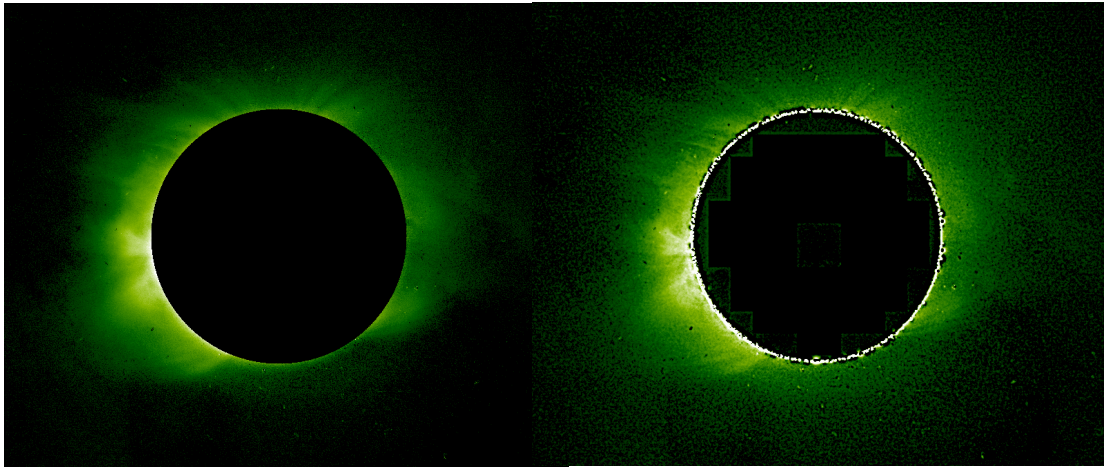
Figure 5.3 Fe XIV green corona as seen by LASCO-C1 on 15th of September 1996 at 15:43 UT (left) plus one reconstruction scheme (right image) based on an 8 first-level scales plus the smooth array, each scale further subdivided in 4 scales plus continuum.

One may notice in the wavelet processed image that the green corona is well seen even above the north pole. At the minimum of activity the coronal holes can be seen in green images (see the south pole) as dark regions. The active regions are confined towards the equator. As seen in wavelet processed image they consist of small loops overlapped by big ones which form the base of a streamer.
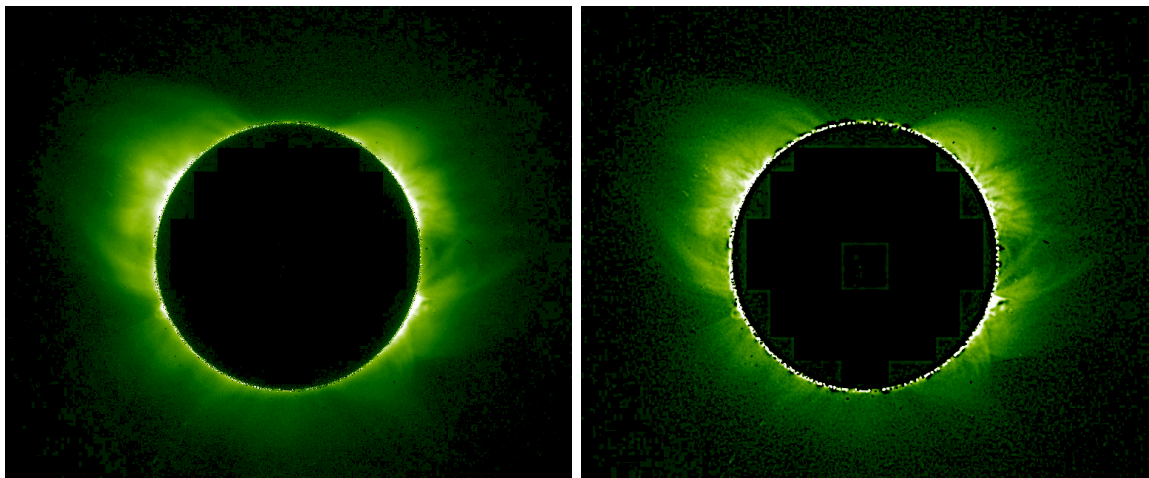
Figure 5.4 Fe XIV green line loops in the inner corona as seen by LASCO-C1 on 24th of June 1998 at 12:14 UT plus one reconstruction scheme (right image) based on an 8 first-level scales plus continuum, each scale further subdivided in 4 scales plus the smooth array.

The wavelet processed image (right one) shows the loops and their internal structure in much more detail, compared to the non-processed image. The active regions consists of small bright loops (see north west side) and big ones (see north east side) all of them continuing out with the streamers. They are present all over the Sun. It is noticed that the coronal holes are almost absent as the Sun is close to the maximum of activity.

In the following the same procedure is applied for red (Fe X) images.
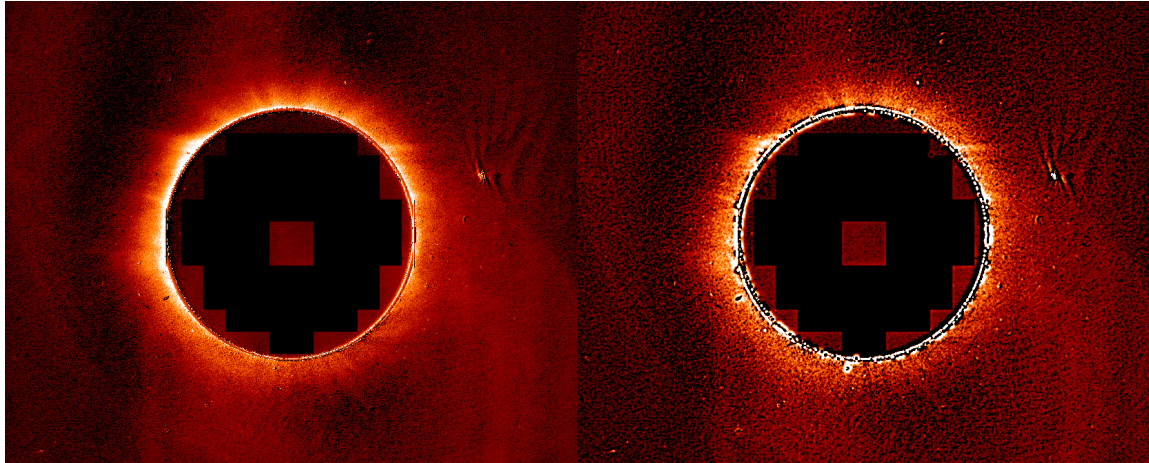
Figure 5.5 Fe X red corona as seen by LASCO-C1 on 15th of September 1996 at 05:56 UT plus a reconstruction scheme (right image) based on an 8 first-level scales plus continuum, each scale further subdivided in 4 scales plus the smooth array.

The red corona is visible all around the limb. One may notice the plumes on both poles. Compared with green corona, the red corona at minimum of activity is seen even at the poles. The coronal holes can not be seen in this line. As the line forms at a a temperature of 1 MK (for Fe XIV the temperaure of formation is 2 MK) the features observed are different from what is seen in green line. No loops are now seen in red images. Also the red corona does not extend as far as the green corona.
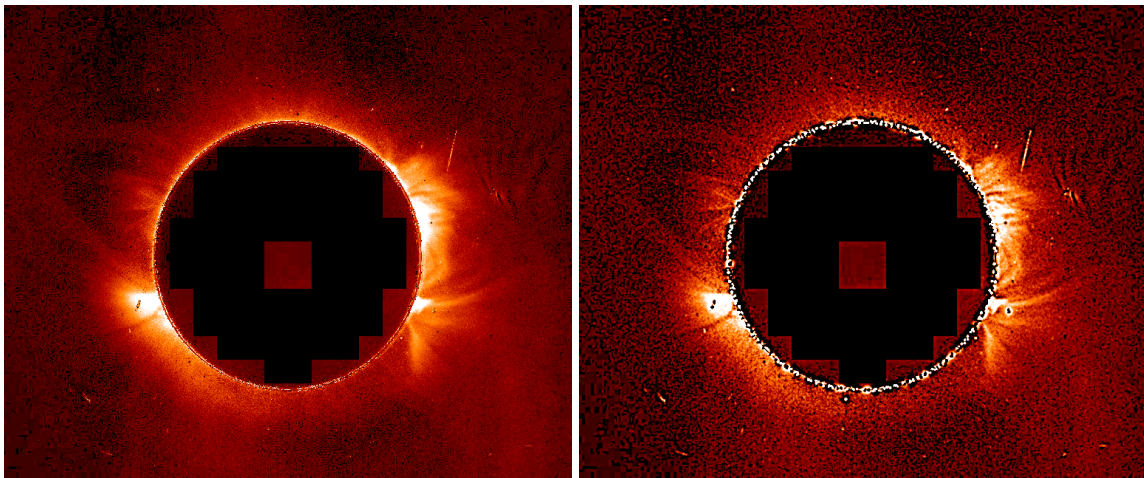
Figure 5.6 Fe X red line loops in the inner corona as seen by LASCO-C1 on 24th of June 1998 at 11:37 UT plus one reconstruction scheme (right image) based on an 8 first-level scales plus continuum, each scale further subdivided in 4 scales plus the smooth array.

For red corona in 1998 the signal is much higher and the loops are well discernable in wavelet processed images (see the right panels of the figures above).

Although the red image was taken on the same day as the green one, different features are observed. Still, the big loop on the north east side is seen in the red image also, as well as the loop on the west side. The hot loops at the north-west side are not seen in the red image.

The wavelet technique helps us to increase the contrast of the features and to determine the large scale motions in the plane of the sky. However, motions perpendicular to that plane, i.e., along the line of sight can only be deduced from spectral scans (see next sections).

5.5   Spectral Data Reduction

A spectral scan (or scan set) consists of several images recorded at different wavelengths. Such a scan allows a spectral line to be characterized at each point in an image.

5.5.1 Measuring the Line Profile

In order to build the profile of a line we take the radiance at a given pixel, of all on-line images in a scan set, as function of corresponding wavelengths (see Figure 5.7).
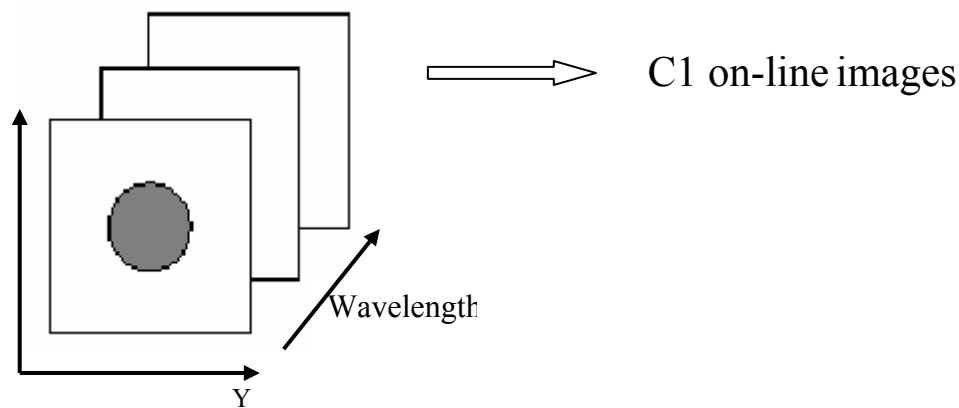
Figure 5.7 C1 spectral data cube.

The data are in counts per second and have contributions from the green or red emission corona, from the continuum corona and from the scattered light in the instrument. The emission is due to coronal Fe XIV and Fe X ions, respectively. The continuum is the photospheric light scattered by the free electrons in the corona. The scattered light in the instrument is photospheric light containing the Fraunhofer absorption lines, which in case of Fe XIV affect the emission profile (see the next sections).

5.5.2 The Wavelength Calibration on the Field-of-View

As we mentioned in the previous chapter, an image is taken at a given "command" wavelength which is written in the header of each fits file. Since there is evidence of an offset between the vacuum wavelength and the noted command wavelength, the wavelengths of each image were adjusted according to the following steps:

a) By measuring the position of the Fraunhofer line at 5303.78 Å (vacuum) the command wavelength was corrected. For doing this the scan of door-closed images were used. These images consist of Fraunhofer absorption lines characteristic of the solar disk. As the positions of these lines are well known (see NSO catalogue) they were used to bring the command wavelength to the correct value for each pixel in the image plain.

b) As the light hits the FP at different incident angles, the transmitted wavelength changes over the field of view of an image. An IDL program is now available in Solar Soft (an IDL package for astrophysical research) which converts a command wavelength to vacuum or air wavelength at any given pixel on the detector (see Figure 5.8).

Figure 5.8 The required wavelength correction across the field of view for a "command" wavelength of 5302.12 Å. The wavelengths in the plot are the corrected ones, in vacuum values. The image is taken on 1st of August 1996, 13:00 UT. The off-line image was subtracted.
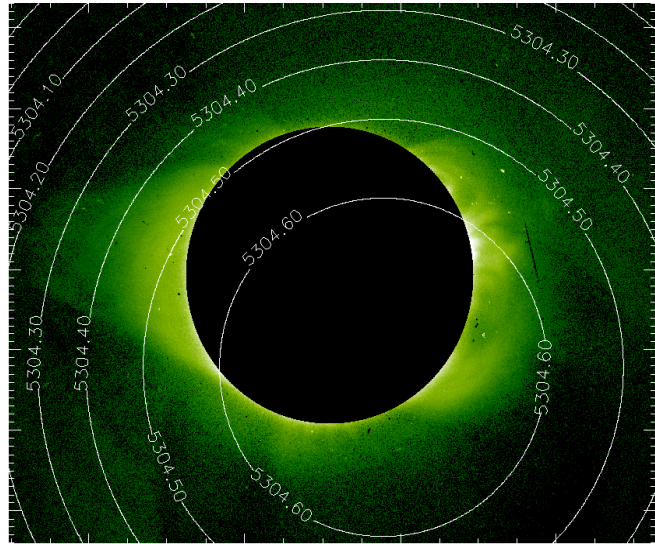
Figure 5.8 shows the measured variation of the passband center of the green line over the C1 field of view. The axis where the light is perpendicular on the detector is called the optical axis of the FP. In Figure 5.8 this axis passes through the center of the white circles. These data were used to correct all wavelength values for each individual pixel. A similar correction applies to the Fe X data too (only the wavelengths are different). The program we used to make this correction (fpc1_wcw.pro) is available in Solar Soft.

5.5.3 Fe XIV Spectral Data - Corrections

Line Profile

In Figure 5.9 we show a typical spectrogram taken at a pixel position: 1.13 $R_\odot$ and PA=272°.
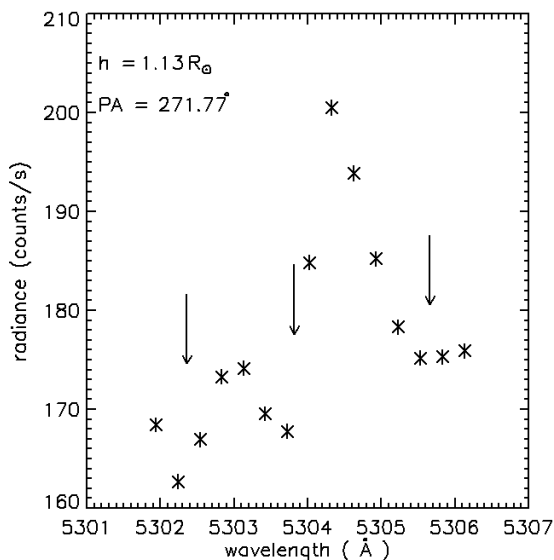
Figure 5.9 Spectrogram of the coronal region (PA 272° and d=1.13$R_\odot$), as observed by LASCO-C1 on 28th of March 1998. The emission line is affected by 3 nearby absorption lines (indicated by the arrows), from scattered photospheric light. The statistical errors as determined by the formula described in section 5.2 are represented by vertical bars (in this case they are smaller than the symbol). The polar angle (PA) is measured from north pole, counterclockwise.

As seen in Figure 5.9, the emission profile is affected by three absorption profiles (indicated by arrows). In order to get the pure emission profile we have to take out the influence of the absorption lines. For this we need to know the characteristics of these lines. The detailed description is given in the next sections.

Exposure Time Correction

For the Fe XIV data the uncertainties in the exposure time as given in the header of every image are too small to affect the profile of our line. This is because compared with the red line the signal is much higher.

Wavelength Calibration using the Absorption Line

Due to the uncertainties in the wavelength calibration of the instrument (see paragraph a) of section 5.5.2) the position of the main absorption line appears offset with respect to its real value as given in the catalogue. Therefore, we use the main absorption line (Fe I) as a standard reference for recalibrating our data and shift the spectra accordingly.

For getting the absorption lines we take those regions in the corona where the emission line is absent, like for example in the coronal holes above the poles. In these regions, at the minimum of activity, the green line does not form due to the low temperatures. The measured radiances are fitted with 3 Gaussians (negative amplitudes) and a constant background. The method of fitting consists in minimization of χ^2, using the Levenberg-Marquardt method (see numerical recipes).

A profile of the absorption spectrogram above the north pole, for a data scan recorded in March 1998, is shown in Figure 5.10. For comparison, the corresponding spectrogram from the photospheric atlas (NSO) is overploted as a dashed line.
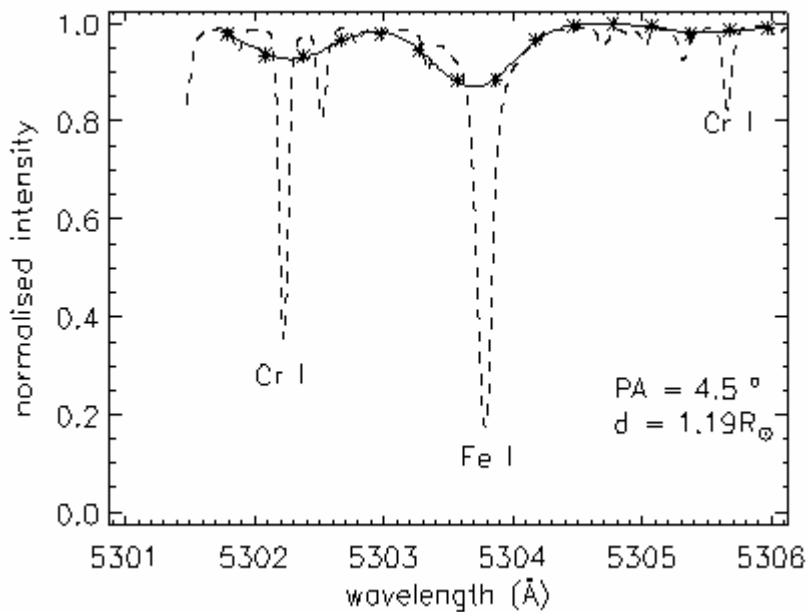
Figure 5.10 Spectrogram obtained for a region without green corona at north pole, in the data recorded on 28th of March 1998 (asterisks). The solid line shows a 3-Gaussian fits to the data. The photospheric spectrogram (in vacuum wavelengths) in the region of interest from *"An atlas of the Spectrum of the Solar Photosphere from 3570 Å to 7405 Å"*, Kitt Peak National Observatory is overploted in dashed line.

The values of the wavelengths are given relative to vacuum. It is noticed that the widths of the absorption lines as measured by C1 are larger than those of the catalogue. This is due to the finite spectral resolution of the instrument.

For the data in 1996 we have only 9 spectral images, and in this case only the main absorption line, at 5303.78 Å can be seen (see Figure 5.11). The flank of the absorption line at 5305.65 Å is also present but it does not influence the main absorption line. Nevertheless, the shift relative to the catalog value can be used for recalibration.
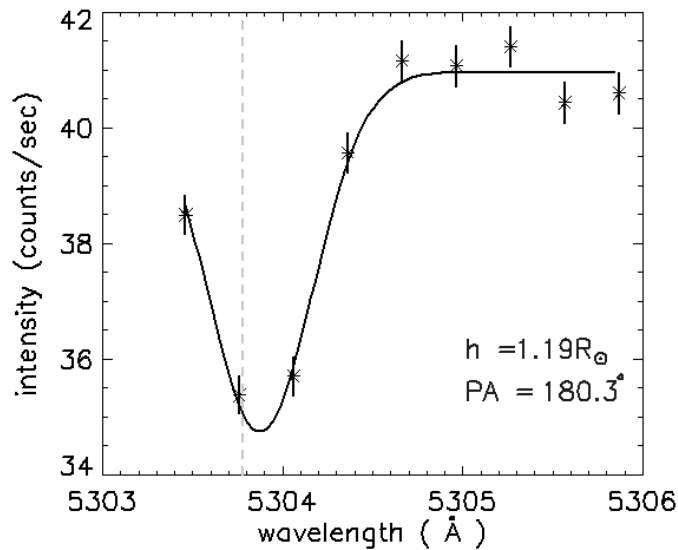
Figure 5.11 Spectrogram obtained for a region without green corona at south pole in the data recorded on 2nd of September 1996 (asterisks). The solid line shows the Gaussian fit to the data. The dashed line shows the position of the absorption line as taken from the catalogue.

The peak of the main absorption line is very close to the emission line and this has a big influence on the emission profile (see Figure 5.12).
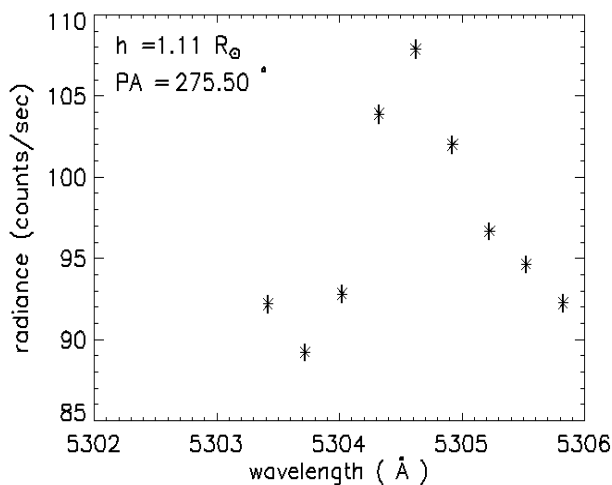
Figure 5.12 Spectrum of the coronal region (PA=275° and d=1.11$R_\odot$), as observed by LASCO-C1 on 2nd of September 1996. The emission line is affected by the nearby absorption line, from scattered photospheric light. The statistical errors (as determined by the formula described in section 5.2) are represented by vertical bars.

In order to get the pure emission profile the influence of the main absorption line has to be taken out.

Since the values obtained for the absorption line are slightly offset with respect to the value from the catalogue, the wavelengths of each on-line image were adjusted to the value of the catalogue.

For getting the absorption line parameters several things have to be taken in consideration:

a) The absorption lines are quantities well known from the spectral catalogue. They are the photospheric light scattered in the instrument containing the Fraunhofer lines.

b) Their wavelength positions, widths and line depressions are known.

c) In our case the widths are larger due to the convolution with the instrumental profile (FWHM=0.6 Å) from the finite spectral resolution of the spectrometer.

d) The continuum level of the photosphere in our spectral range is constant.

e) We have contributions from both photospheric background and the continuum corona. We cannot keep the ratios of the line amplitudes and the underlying background constant.

    f)   The ratios between the small absorption line amplitudes and the main absorption line amplitude are constant.

    g)   For the widths and amplitudes we cannot use the values from the spectral atlases. We get them from our data.

    h)   The wavelength positions of the two small absorption lines are not that of the atlas due to the influence of the neighboring absorption lines (which cannot be resolved due to the insufficient spectral resolution of the spectrometer).

Having this in mind, we compute for every set the median value (of all relevant pixels) of the absorption line position. We plot these median values for the data sets in 1996 in Figure 5.13 and for data sets in 1998 in Figure 5.15. The difference between these points and their median value (solid line) are the corrections used for every set to calibrate the wavelength.
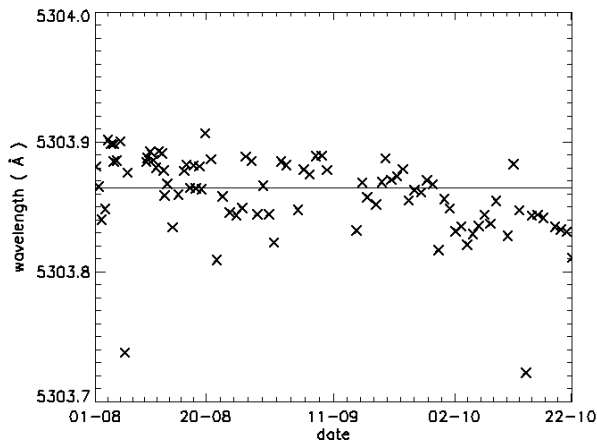
Figure 5.13 The median values of the position of the main absorption line in a region at the south pole (crosses), plotted versus the time in 1996. The solid line represents the median of these values.

The scatter of the position of the main absorption line around the median value is very small. After calibrating the wavelength, all of them have the value of the catalogue (5303.78 Å).

In the same way we compute the median values of the FWHM of the absorption line and we plot them versus time (Figure 5.14).
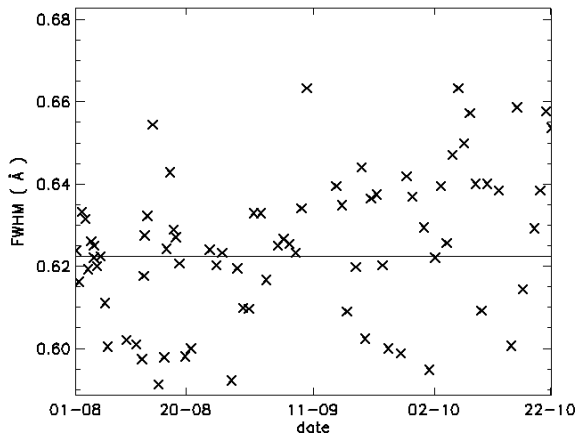
Figure 5.14 The median values of the FWHM of the main absorption line in a region at the south pole (crosses), plotted versus the time.

.

The values of FWHM for every data set are scattered around the median value represented in the graph by the horizontal line. This value is used further for fitting the data.

The ratio of the amplitude of the weaker line to that of the stronger line has to be constant (see the above paragraph).

It was not possible to determine the parameters of the weak absorption line because of the few spectral data (9) we have in this period. To get these parameters we should fit the data with 2

Gaussians and one constant background, i.e. 7 parameters. In this case there will be only 2 free parameters. Nevertheless we can get these values from the data in 1998 when we have enough points to make the fit with the sum of 3 Gaussians and a constant background (see the next sections).

Similar evaluations for the data in 1998 are shown in Figures 5.15 and 5.16.
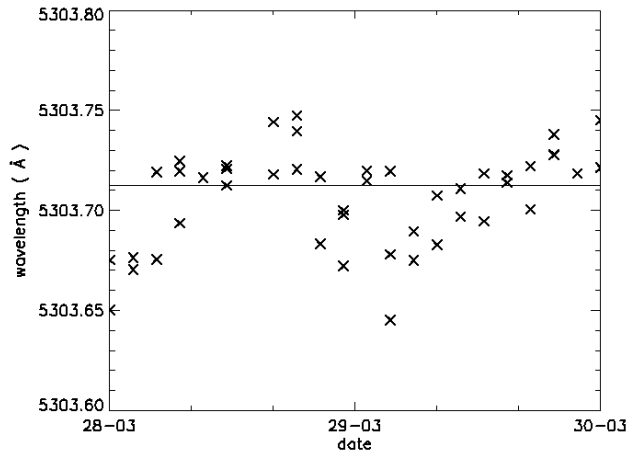
Figure 5.15 The median values of the position of the main absorption line in regions at the south and north poles (cross), plotted versus the time in 1998.

The positions of the absorption lines are all shifted to overlay the value from the catalogue (5303.78 Å). The shifts are used to recalibrate the wavelengths for every data set.

The median values of the FWHM for a region at the south pole are plotted versus time (see Figure 5.16).
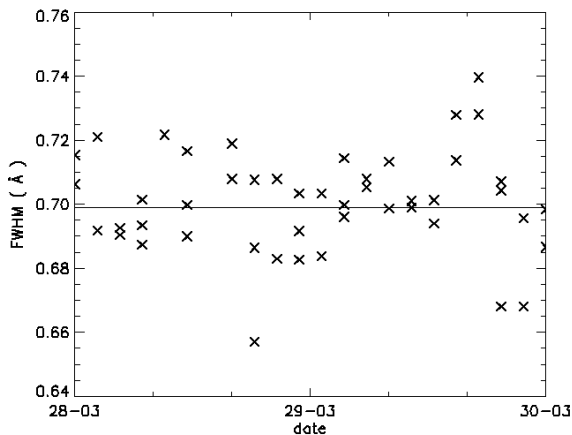
Figure 5.16 The median values of the FWHM of the main absorption line in regions at the south and north poles, plotted versus the time.

The horizontal line is the median of the FWHM for all data sets. It will be used in fitting the data (see the next sections).

The same kind of plots were performed for the two small absorption lines (See Figure 5.17 and Figure 5.18).
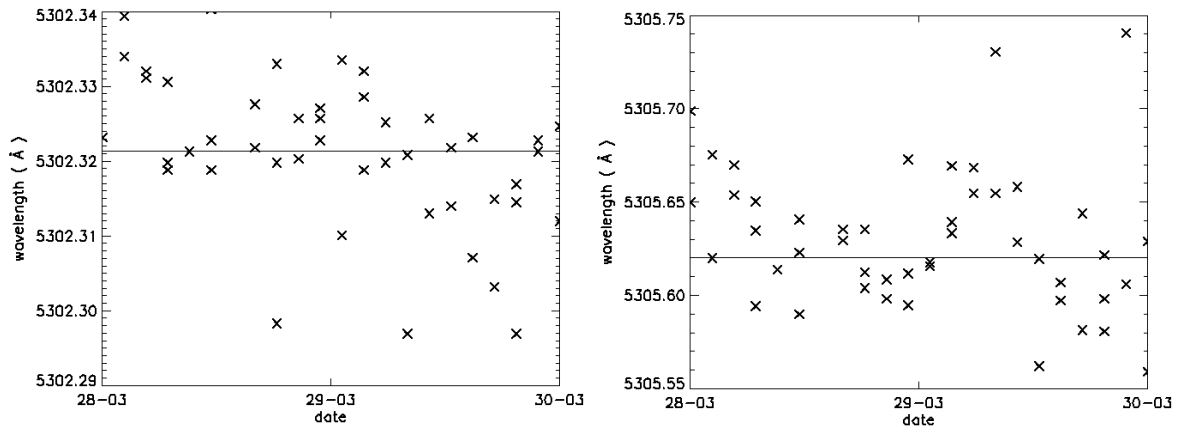
Figure 5.17 The median values of the position of the 2 small absorption lines, after wavelength recalibration, (left panel: line at 5302.22 Å; right panel: line at 5305.65 Å) in regions at the south and north poles, plotted versus time.

The positions of the weakest absorption line (at 5305.65 Å) in right panel are more scattered then the other two absorption lines. Nevertheless its median value is used to fit the data.

We observed for the FWHM the same behavior for the two weak absorption lines (at 5302.22 Å and at 5305.65 Å) (see Figure 5.18).
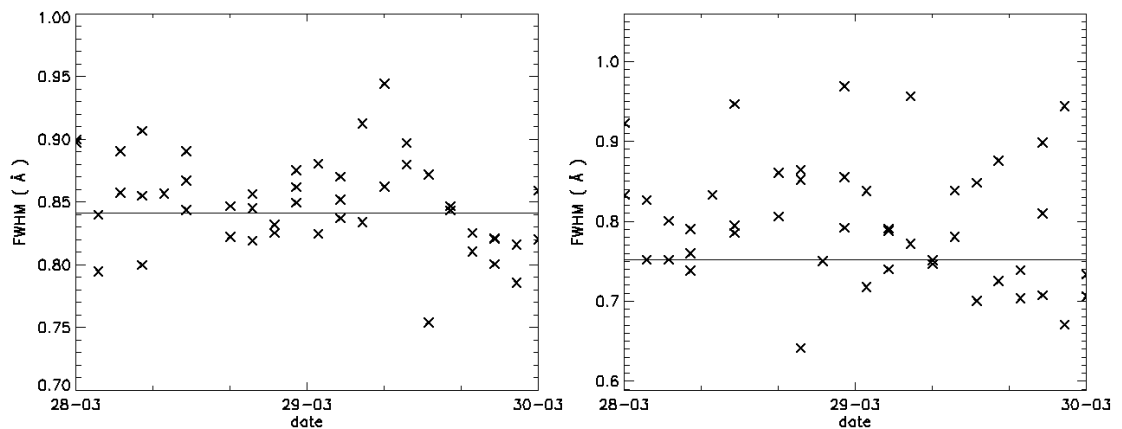
Figure 5.18 The median values of the FWHM of the 2 weak absorption lines (left panel: line at 5302.22 Å; right panel: line at 5305.65 Å) in regions at the south and north poles, plotted versus the time.

Differently from the data in 1996, this time we can make an estimate of the ratios of the 3 absorption lines. We show these ratios in Figure 5.19.
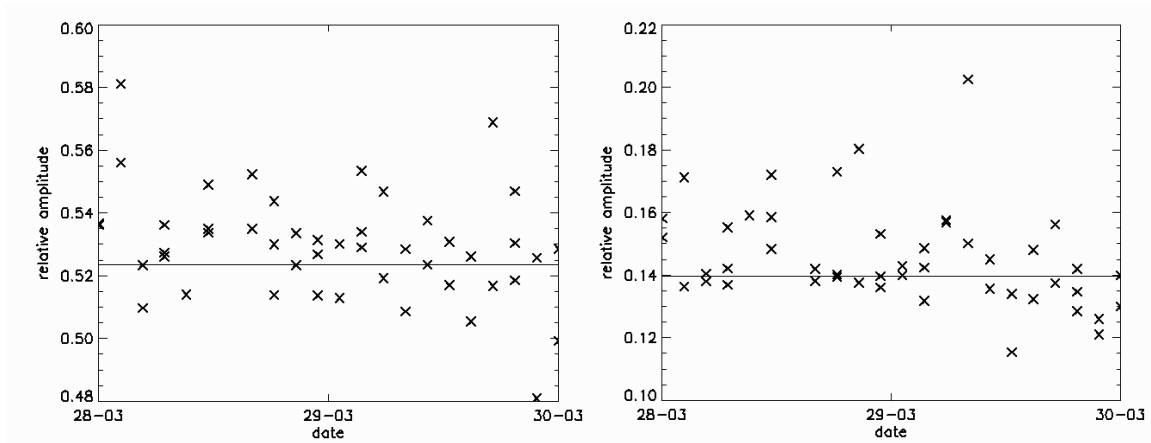
Figure 5.19 The median values of the relative amplitudes of the 2 small absorption lines with respect to the main absorption line (left panel: the line at 5302.22 Å; right panel: the line at 5305.65 Å) in regions at the south and north poles, plotted versus the time (or number of data sets). The continuum line is the median value of these points.

It is noticed that the scatter of the points around the median value is very small.

The median values of the absorption line parameters are used further for fitting the emission line data.

5.5.4 Fe X Data - Corrections

Line Profile

For the Fe X line we have to modify the correction procedure since there are no absorption lines nearby. The profile is a Gaussian right away (see Figure 5.20), and the only inconvenience is that we cannot recalibrate the position of the line. But we can calculate everything relative to a given position. This is shown in the next sections.
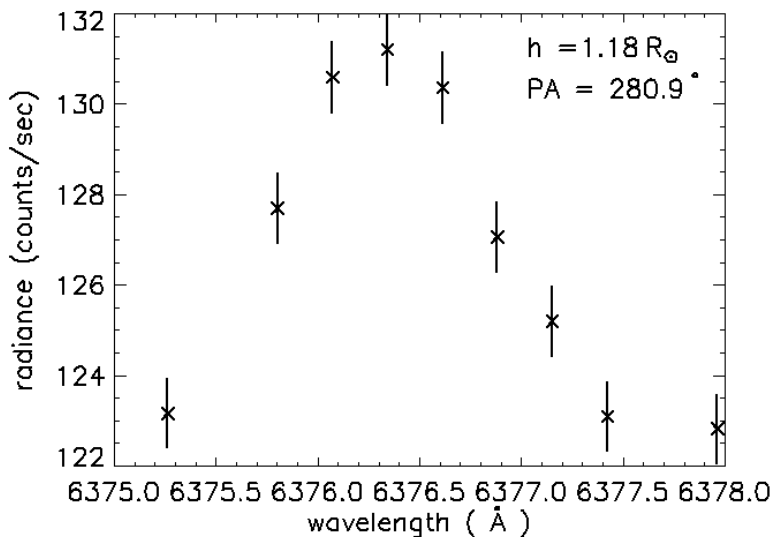
Figure 5.20 Spectrum of the Fe X line for a coronal region on the west side of the limb, as observed by LASCO-C1 on 2nd of August 1996. The errors are represented by vertical bars.

Exposure Time Correction

The red-line signal is very weak compared to the underlying bright stray-light background. The exposure time as given in the header of each image turned out to be not sufficiently precise. Therefore a specific recalibration technique had to be applied.

In order to find optimum correction factors we took for reference parts in the images, where there is definitely no red corona present. We take a circular cut, of 0.1 $R_\odot$ width at a distance of 1.8 $R_\odot$. The spectral profile should be a straight line for every data set if all exposure times were equal. Figure 5.21 shows that there indeed are deviations of the order of a few per mille. We found that these deviations are very similar for most pixels.
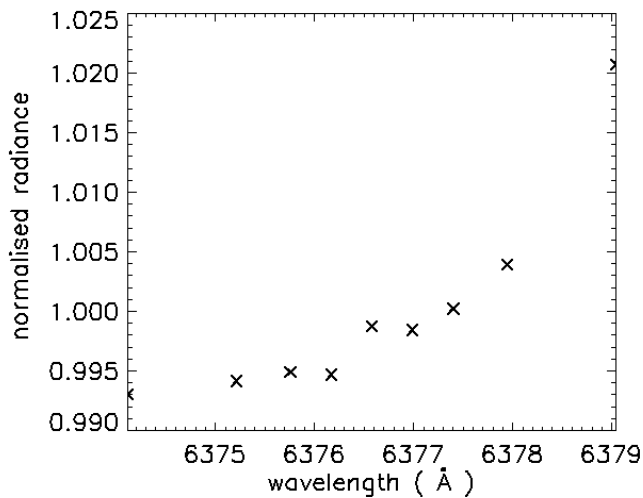
Figure 5.21 The exposure time correction factors for a data set taken on 20th of August 1996.

We conclude that the deviations are due to slight uncertainties in the exposure times, and thus can be used to correct them. Therefore, we compute a normalized spectrum over all pixels in the selected reference region (see Figure 5.21). Every radiance in each data set is then divided by these factors. Examples of profiles, before and after the correction are shown in Figure 5.22.
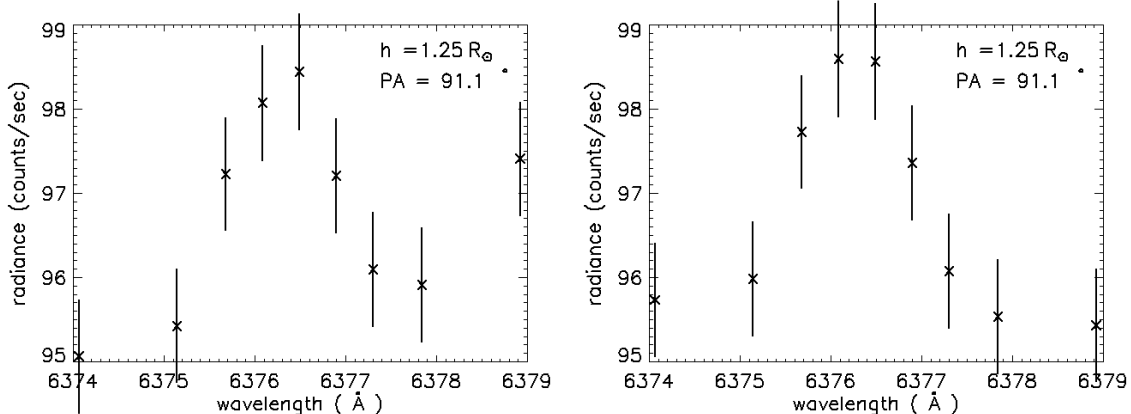
Figure 5.22 Spectrum of the Fe X line for a coronal region on the east limb, as observed by LASCO-C1 on 20th of August 1996 (left panel). The right panel is the spectrum corrected for the exposure time. The errors are represented by vertical bars.

Although this correction is very small in absolute numbers, the emission line profiles have become significantly clearer.

5.6 Determination of the Emission Line Parameters

Before computing the peak radiance (amplitude), central wavelength (position) and widths (FWHM) of the emission line (see Figure 5.23), some additional image reduction has to be applied:

1) To discard the isolated bad pixels we apply a running median of size 5x5 pixels over each spectral image.

2) The green and red corona is on the top of a large straylight background. In order to reduce the noise for the data in 1996 we create superpixels of 4 pixels in radial direction and one degree in azimuthal direction. Line profile fits are done for each superpixel.

3) For the data in 1998 we have enough signal to fit the data in every pixel of an image.
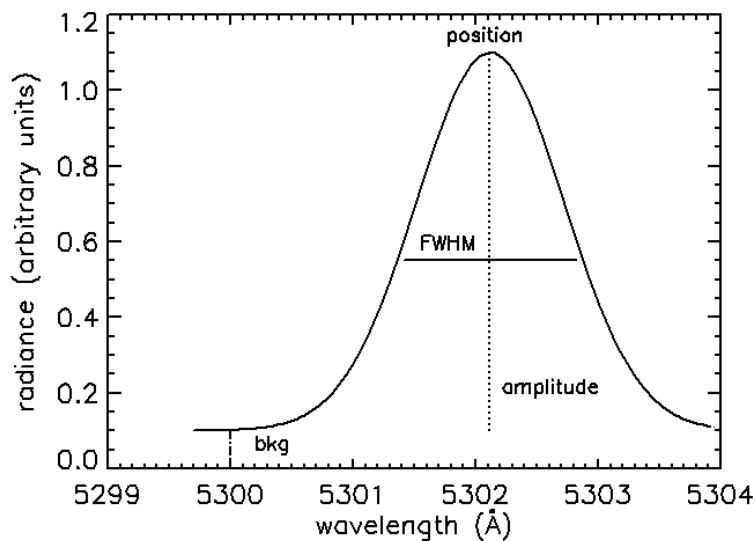
Figure 5.23 Sketch of the Fe XIV emission line. The radiance is given in arbitrary units. The central wavelength (position), is 5303.112 Å and the FWHM (horizontal line) is 1.41 Å. A constant background (dotted line) of 0.1 was chosen.

After the above mentioned corrections we can fit each pixel or superpixel of a data set by the functions we explain below. New images are created where each pixel is replaced by its radiance or amplitude (see Figure 5.23) (radiance map), by the line width or FWHM (FWHM map) and by line of sight speed (speed map). The last quantity is measured from the shift of the line position (see Figure 5.23) with respect to a rest wavelength (called also Doppler shift).

5.6.1 Fe XIV Data

To recapitulate, the steps we follow to process Fe XIV spectral data are:

a) Correction of the "command" wavelength: As the wavelength in the header of every image was found to be inaccurate, the closed door images are used to recalibrate the wavelengths.

b) Correction of the wavelengths in the field of view: due to different incident angles an image will have different wavelengths at different positions (see Figure 5.8).

c) Recalibration using the main absorption line: Due to the uncertainties in the wavelength calibration of the instrument (see paragraph a)) the position of the main absorption line is offset with respect to the catalogue. We shift all the spectra accordingly.

Line Fit

The corrected intensities for each pixel are fitted with the sum of 4 Gaussians (3 absorption lines with the parameters deduced as explained above, plus one emission line) and a constant background. For the absorption lines we keep as free parameters only the ratio of the main absorption line amplitude to the background, all the other parameters having the values as deduced from the polar regions (i.e. the positions of the 3 lines, the widths of the 3 absorption lines, the ratios of the 2 small absorption line amplitudes to the main absorption line amplitude). In order to explain why we leave free the main absorption line amplitude we should remember that the observed spectral profile consists of line emission from ions in the corona (in this case Fe XIV), photospheric light scattered at free electrons in the corona ("continuum corona") and instrumental scattered light. For the regions above the poles the instrumental scattered light is the brightest source and the ratios of the 3 lines with respect to this are constant. This may not be true for the rest of the corona. The "continuum" corona may have a big contribution also and because of this we keep as a free parameter the main absorption line amplitude. We keep constant only the ratios between the 2 small absorption line amplitudes and the main absorption line amplitude. The function to fit the data is described below:

$$I(\lambda) = I_{abs} \cdot (term_1 + term_2 + term_3) + I_{emis} \cdot e^{-\frac{1}{2}\left(\frac{\lambda - \lambda_0}{\sigma}\right)^2} + B$$

$$term_1 = I_1 \cdot e^{-\frac{1}{2}\left(\frac{\lambda - \lambda_1}{\sigma_1}\right)^2}$$

$$term_2 = I_2 \cdot e^{-\frac{1}{2}\left(\frac{\lambda - \lambda_2}{\sigma_2}\right)^2}.$$

$$term_3 = I_3 \cdot e^{-\frac{1}{2}\left(\frac{\lambda - \lambda_3}{\sigma_3}\right)^2}$$

The variables are: $I_{abs}, I_{emis}, \lambda_0, \sigma, B$.

The constants are: $I_1 = 0.52 \cdot I_{abs}$; $\qquad I_2 = 1 \cdot I_{abs}$ $\qquad I_3 = 0.14 \cdot I_{abs}$,

$\qquad \lambda_1 = 5302.32 \, Å,$ $\qquad \lambda_2 = 5303.78 \, Å,$ $\qquad \lambda_3 = 5305.62 \, Å,$

$\qquad \sigma_1 = 0.36 \, Å,$ $\qquad \sigma_2 = 0.30 \, Å,$ $\qquad \sigma_3 = 0.32 \, Å$

An example of such a fit is shown in Figure 5.24.
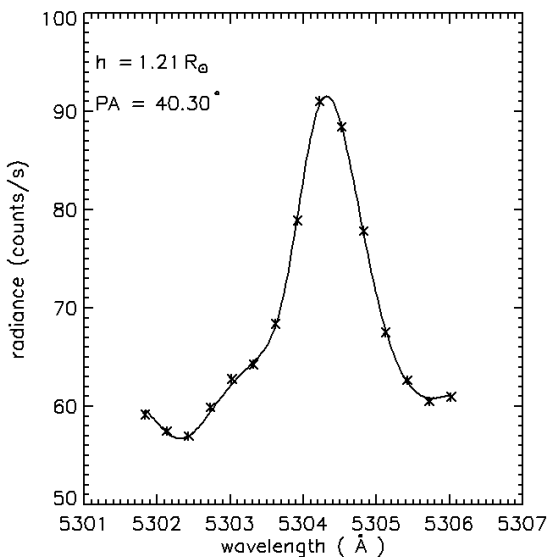
Figure 5.24 The green line profile for a certain pixel above the east limb of the Sun. The solid line shows the fit to the data. The crosses are the original corrected data points. The vertical bars represent the errors (in this case they are very small).

In Figure 5.25 we show the same plot as in Figure 5.24, with the 4 components plotted separately.
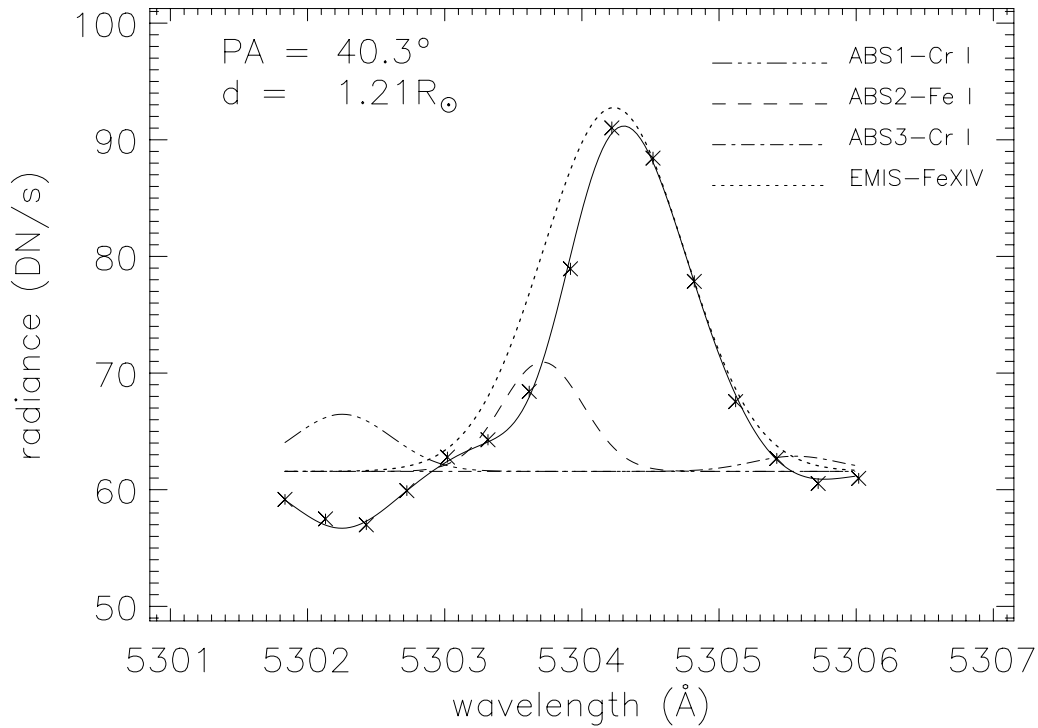
Figure 5.25 The line profile for the same region as in Figure 5.24. The absorption contributions are inverted and are shown in dash-dot-dot, long-dash and dash-dot lines. The emission line is the dotted one. The sum of all contributions is shown by the solid line. The asterisks are the original corrected data points.

For the absorption lines we inverted the sign of the amplitudes. The sum of all contributions is plotted as solid curve. We can see that it fits the measured points very well.

The data in 1996 were taken in limited spectral range covering only 2 absorption lines. The function to fit the data is:

$$I(\lambda) = I_{abs} \cdot (term_2 + term_3) + I_{emis} \cdot e^{-\frac{1}{2} \left(\frac{\lambda - \lambda_0}{\sigma} \right)^2} + B$$

$$term_2 = I_2 \cdot e^{-\frac{1}{2} \left(\frac{\lambda - \lambda_2}{\sigma_2} \right)^2}$$

$$term_3 = I_3 \cdot e^{-\frac{1}{2} \left(\frac{\lambda - \lambda_3}{\sigma_3} \right)^2}$$

The variables are: I_{abs}, I_{emis}, λ_0, σ, B.

The constants are: $I_2 = 1 \cdot I_{abs}$, $I_3 = 0.14 \cdot I_{abs}$,

$\lambda_2 = 5303.78\ Å$, $\lambda_3 = 5305.62\ Å$,

$\sigma_2 = 0.30\ Å$, $\sigma_3 = 0.32\ Å$

An example of such a fit is shown in Figure 5.26.
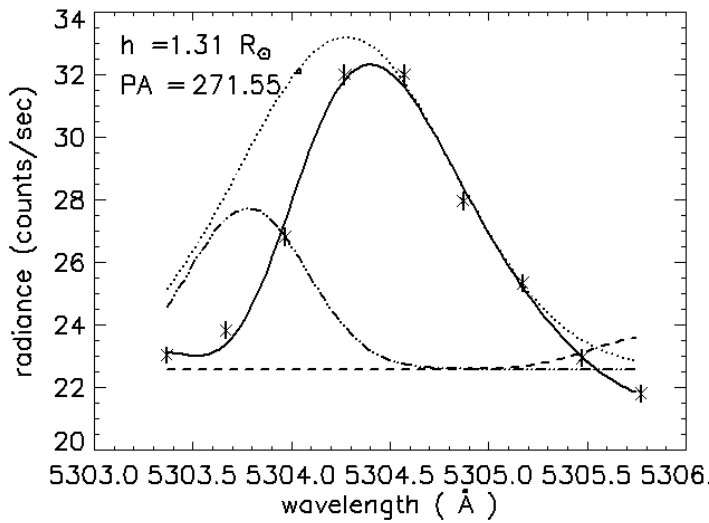
Figure 5.26 The line profile for a region at 1.31R$_\odot$ and PA = 272°. The absorption contributions are inverted and are shown in dash-dot-dot and long-dash lines. The emission line is the dotted one. The sum of all contributions is shown by the solid line. The crosses are the original corrected data points. The vertical bars represent the statistical errors as computed in section 5.2. The data were recorded on 2nd of September 1996.

The figure shows all the contributions to the line profile. The main absorption line (dash-dot-dot) has a big influence on the emission profile (dot). The most sensible is the width of the line which tends to become narrower by the contributions from the scattered light.

Selection Criteria

In cases of very low radiances the procedure of fitting can lead to unrealistic unphysical results, due to noise or data errors. We wish to retain only reasonable points and eliminate the points where:

- the relative errors of the parameters as deduced from the fit (see section 5.2) are bigger than 0.2,
- the position of the line is not in the range 5303 - 5305 Å
- the FWHM of the emission line is not in the range 0.6 (instrumental profile) – 5 Å.

The errors are given by the programs we use to make the fit. They are the uncertainties in determining the parameters. We use the diagonal elements of the covariance matrix in order to estimate the errors (see the short description below).

The method used is called Levenberg-Marquardt (Press et al. 1992). The error estimates are given by the formula:

$$\delta a_i = \pm \sqrt{\chi^2 \cdot C_{ii} \cdot \frac{M}{N}}$$

where δa_i is the error estimate of the parameter a_i.

N is the degree of freedom (total number of sampled points minus number of fitted parameters),

M is the total number of sampled points,

χ^2 is the merit function.

C_{ii} are the diagonal terms of the covariance matrix. C is the inverse of the Hessian matrix used in the Levenberg-Marquardt method.

In principle, the errors using the diagonal elements of the covariance matrix are underestimated, because the correlations between the free parameters are not taken into account.

Solar Rotation Correction

Near the solar equator, the apparent line of sight speed due to solar rotation amounts to +/- 1.85 km/s. In the distance range we are investigating using C1 data we can expect rigid rotation of the solar atmosphere, i.e. with increasing solar distance the line-of-sight speed also increases linearly. This effect is superposed on the coronal flow pattern we are interested in. Therefore we derived a method to compensate for this rotation effect.

At first, we demonstrate that this rotation effect is in fact visible in our spectral data, by comparing east and west limb data. We build histograms of all measured line centers of the green corona up to 1.8 $R_\odot$ at the east, respective west limb. We obtain 2 Gaussians with slightly different peak positions as shown in Figure 5.27.
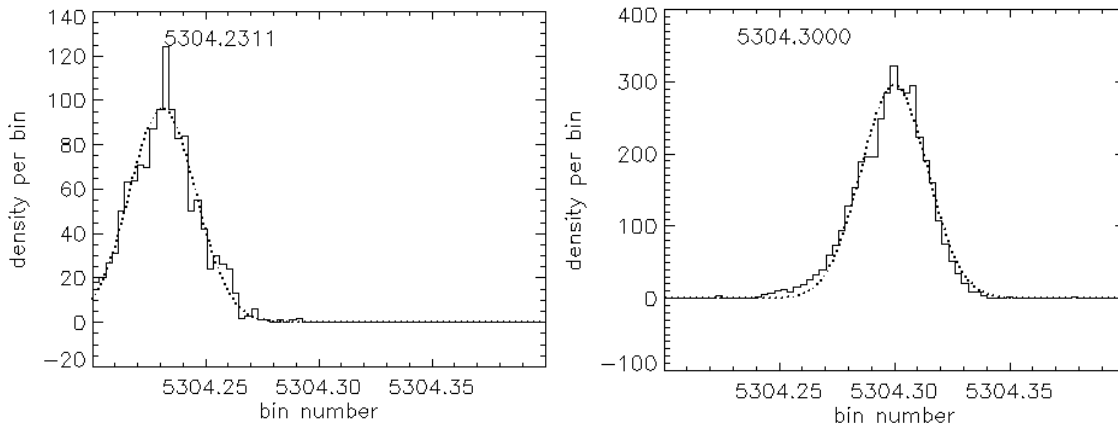
Figure 5.27 The histogram of the green line positions for east (left) and west (right) images, recorded on 30th of March 1998.

For correction, we assume the solar and coronal rotation as both being rigid, depending only on the distance from the rotation axis (e.g., Stenborg et al. 1999).

The formula used to compute the solar rotation is:

$$v_{rot} = \frac{2\pi}{t} \cdot r$$

where t is the period of rotation (t = 27.2 days·86400=2 351 080 s) and r is the distance of our data from the rotation axis.

We create an image with the rotation velocities (see Figure 5.28) which will be subtracted from the velocity map.
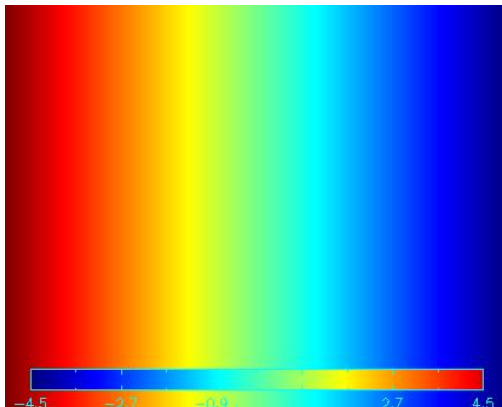
Figure 5.28 The solar rotation velocity map assuming rigid rotation. This image is subtracted from the Doppler images in order to correct for the rotation of the corona. The scale goes from -4.5 (red colors) to 4.5 km/s (blue colors).

After applying this correction, the histograms as shown in Figure 5.29 are obtained.
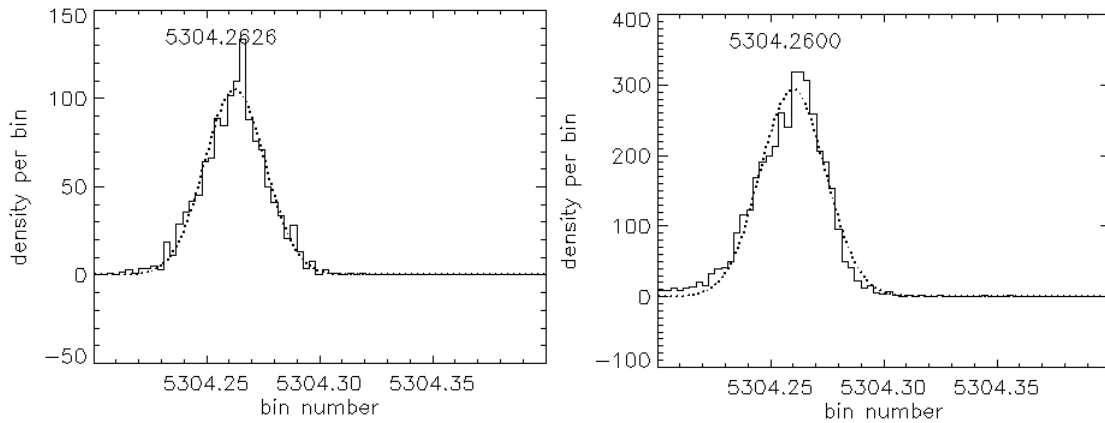
Figure 5.29 The histograms of the line positions for east (left) and west (right) images, after correcting for solar rotation.

It is noticed that the difference between the peak positions of the 2 histograms is of the order of 0.0028 Å, equivalent with 0.15 km/s (i.e. negligible).

Rest Wavelength Computation

Unlike for the absorption lines, there is no exact value for the "rest" wavelength of the green emission line. In order to define a reference value we assume that the corona as a whole is at rest. Therefore, we build the histograms of all measured line centers of the green corona in 1998 up to 1.8 $R_{\odot}$ at east, respective west limb (see Figure 5.29). We take the mean value (5304.26 Å) as reference wavelength, relative to which we determine individual line shifts. For the Fe XIV data in 1996 we get a rest wavelength value of 5304.4 Å. In the last case the errors are much bigger due to only 9 spectral points we have in the respective period of time. The theoretical values from atomic databases give a value of 5304.34 Å.

Uncertainties in Speed Determination

In order to give an estimate on how precisely we can determine the line-of-sight velocities we determine the sigma (standard deviation) for the histograms built as explained above. We get a value of 0.035 Å. We take this as being the uncertainties in measuring the position of the line. As 0.1 Å corresponds to a speed of 5.6 km/s, our uncertainty is approximately 2-3 km/s.

Emission Maps Computation

In the following we compute the emission maps:

Radiance Maps

From the radiance at the peak of the line we get the density distribution of the Fe^{+13} ions in the corona (see Figure 5.30).
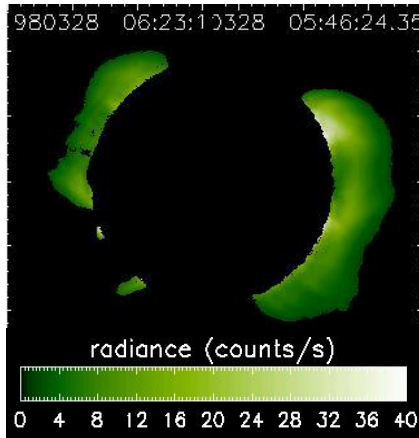
Figure 5.30 The radiance map for Fe XIV data on 28th of March 1998. The white color represents high radiance values.

The radiance maps give us information about the ion density distributions in the solar corona. The Fe XIV ions are confined usually around the magnetic field lines usually in the shape of loops (see north west side of the above image). A detailed description is given in Chapter 6.

Velocity Maps

From the shift of the central wavelength to the reference wavelength (Doppler shift), we can get the line-of-sight velocity:

$$\frac{\lambda_0 - \lambda}{\lambda_0} = \frac{v}{c}$$

λ_0 is the rest (reference) wavelength, v the line-of-sight velocity and c is the speed of light.

For $\lambda > \lambda_0$ the plasma moves away from the observer (the wavelengths are shifted to the red part of the visible spectrum).

For $\lambda < \lambda_0$ plasma moves towards the observer (the wavelengths are shifted to the blue part of the visible spectrum).

Figure 5.31 shows an example of a Doppler map for Fe XIV data. Blue and green represent plasma moving towards the observer, red and yellow plasma moving away from the observer and white is static plasma with respect to the observer.
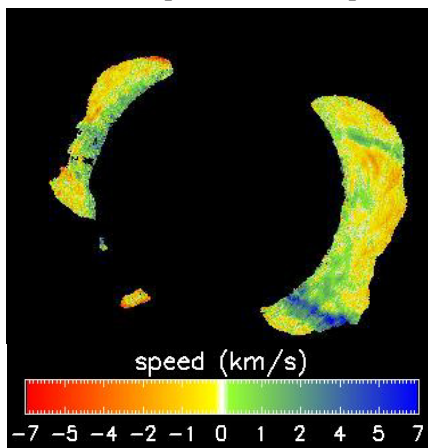
Figure 5.31 The velocity map for Fe XIV data, showing the plasma moving along the line of sight in the range -10 to 10 km/s. The uncertainties in determining the speed values are of 2-3 km/s. The data were recorded on 28th of March, 1998.

One may notice the strong blue shift in the streamer at the south west limb. This will be described in Chapter 6.

FWHM Maps

From the width of the line, after correcting from the instrumental profile (0.6 Å), we can get information on the "effective temperature" of the ions in the corona.

In the following example we show the FWHM for Fe XIV data. We will come back to the effective ion temperature in Chapter 6.
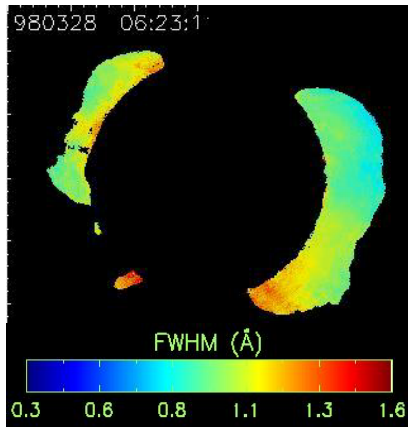
Figure 5.32 The FWHM map for Fe XIV data. The red color represents a large width (high effective ion temperature), and blue means a narrow line (low effective ion temperature). The data were recorded on 28th of March, 1998.

5.6.2 Fe X Data

To recapitulate, the steps we follow to process Fe X spectral data are:
   a) Correction of the wavelengths in the field of view: due to different incident angles an image will have different wavelengths at different positions (see Figure 5.8).
   b) Exposure time correction: because the exposure time reported in the header of each image is slightly inaccurate, the radiances in the profile are slightly displaced from their real value.

Now we can create the emission maps:

Line Fit

The measured intensities are fitted with a Gaussian plus a constant background. An example is shown in Figure 5.33:
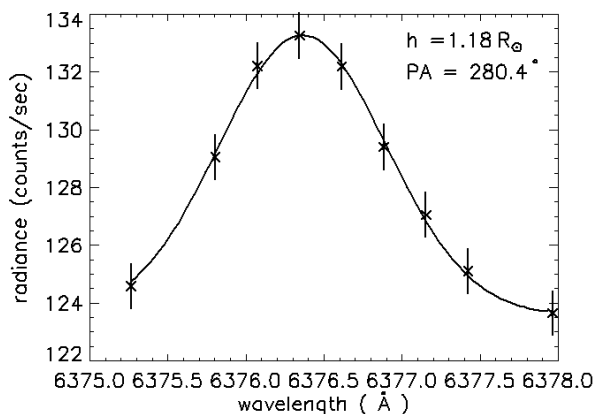

Figure 5.33 The Fe X line profile for a region on the west side of the Sun. The solid line shows the fit to the data. The crosses are the data points. The vertical bars represent the statistical errors as computed in section 5.2.

Selection Criteria

The procedure of fitting can lead to unrealistic, i.e. unphysical results, due to noise or data errors. We keep only the reasonable points and we eliminate the points for which:

- the relative errors of the parameters as deduced from the fit (see section 5.2) are bigger than 0.2,
- the position of the line is not in the range 6374 - 6379 Å
- the FWHM of the emission line is not in the range 0.8 (instrumental profile) – 5 Å.

The errors from the fit were explained in Section 5.61 in which the treatment of the Fe XIV data was described.

Solar Rotation Correction

We correct all spectra for the rotation of the corona, similar to the procedure described for the green line in Subsection 5.6.1. We consider it as being rigid, depending only of the distance from the rotation axis (see Fe XIV data).

If we build the histograms of all measured line centers of the red corona up to 1.5 $R_\odot$ at east, respective west limb we get the mean values as shown in Figure 5.34:
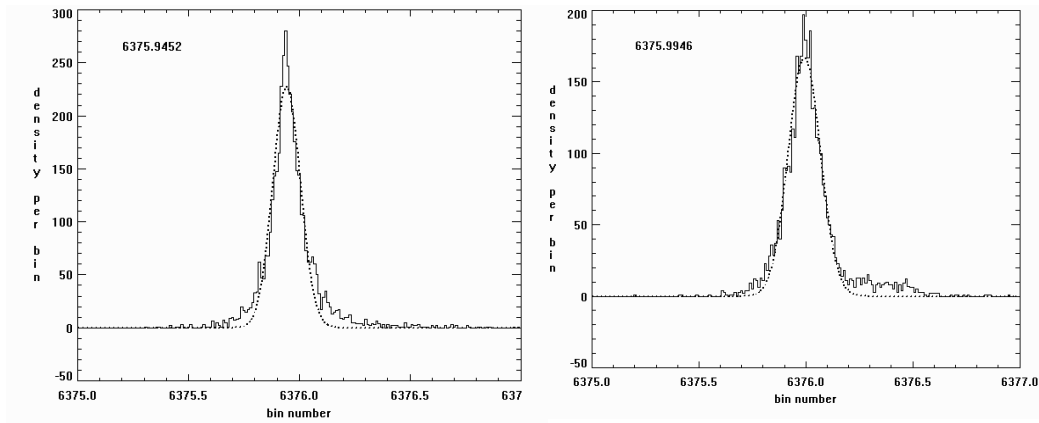
Figure 5.34 The histogram of the line positions of Fe X, for east (left) and west (right) images, before correcting for solar rotation. The dotted line is the Gaussian fit to the histograms. The data were recorded on 8th of May 1998.

After correcting for the solar rotation this difference disappears, as shown in Figure 5.35:
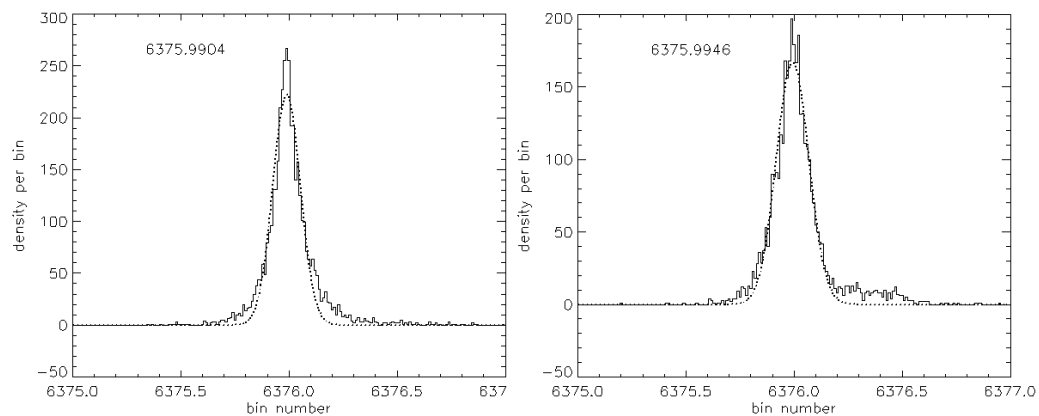
Figure 5.35 The histogram of the line positions of Fe X, for east (left) and west (right) images, after correcting for solar rotation.

In conclusion, the difference in the mean values of the line of sight speeds is due to the solar rotation.

Rest Wavelength Calculation

In order to determine the rest wavelength we build the histograms of all measured line centers of the red corona up to 1.5 $R_\odot$ at east, respective west limb, after removing the solar rotation. We take the mean value (6375.99 Å) as reference wavelength, relative to which we determine individual line shifts (see Figure 5.34).

Uncertainties in Speed Determination

As explained for the Fe XIV data the uncertainties to determine the line-of-sight velocities are around 2 km/s. We apply the same procedure to the Fe X data. We compute the standard deviation of the histograms built as explained above. We get a value of 0.06 Å (around 3 km/s). This is the uncertainty in measuring the line position.

Emission Maps Computation

From the line fits we determine:

The Radiance Maps

From the maxima of the line radiance the amplitude maps are computed (see Figure 5.36).
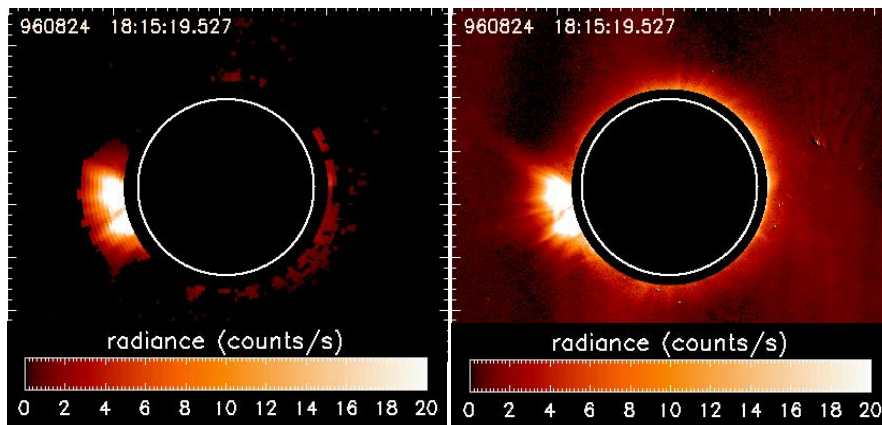
Figure 5.36 The radiance map for Fe X data (left image). The on minus off line image (right). The white color represents a high radiance (counts/s). The data were recorded on 24th of August, 1996.

For comparison the on- minus off-line image is shown (right side of Figure 5.36).
A detailed description of red corona features is given in Chapter 6.

The Velocity Maps

The line-of-sight velocities are computed from Doppler shifts (see Figure 5.37).
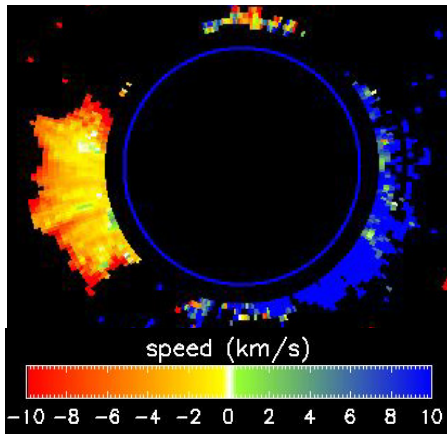
Figure 5.37 The velocity map for Fe X data, showing the plasma moving along the line of sight in the range -7 to 7 km/s. The uncertainties to determine the values are of 3 km/s. The data were recorded on 24th of August, 1996.

The red and yellow colors represent plasma moving away from the observer and blue and green plasma moving towards the observer. More about it is shown in Chapter 6.

The FWHM Maps

The FWHM gives us information about the "effective ion temperature" in the corona. An example is shown in Figure 5.38.
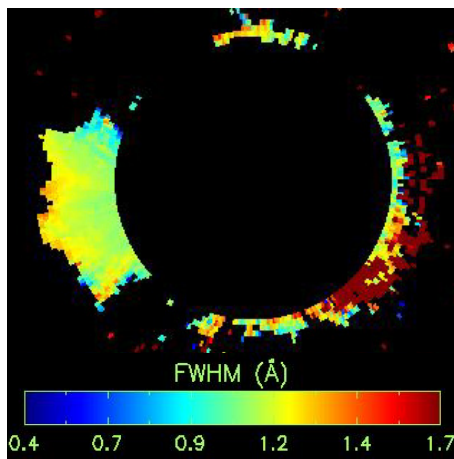
Figure 5.38 The FWHM map for Fe X data. The red color represents a large width (high effective ion temperature), and blue means a narrow line (low effective ion temperature). The data were recorded on 24th of august, 1996.

Bluish colors mean narrow line widths and reddish large line widths (see the detailed description in Chapter 6).

Chapter 6 Data Interpretation and Discussions

The parameters of the emission lines give us information about the ion density distributions (spectral radiance at the peak of the line), "ion temperature" (the width of the line) and bulk velocities (the Doppler shift from the position of the line peak) in the corona, for each pixel in the images.

6.1 Emission Map Interpretation

6.1.1 Radiance Maps

As we said in the previous chapter, for each pixel or superpixel in a data set, the radiance of the line was determined from the fitting procedure. These peak spectral radiances were then assembled in "radiance maps". The radiance maps give us information about the ion topology in the solar corona. In the following examples we show both green and red line images. Radiance maps and routine data are presented in order to compare them. Also a comparison between data in 1996 and data in 1998 is done.

In Figure 6.1 we show an example of a Fe XIV radiance map and for comparison routine data (see Chapter 4) from 1996.
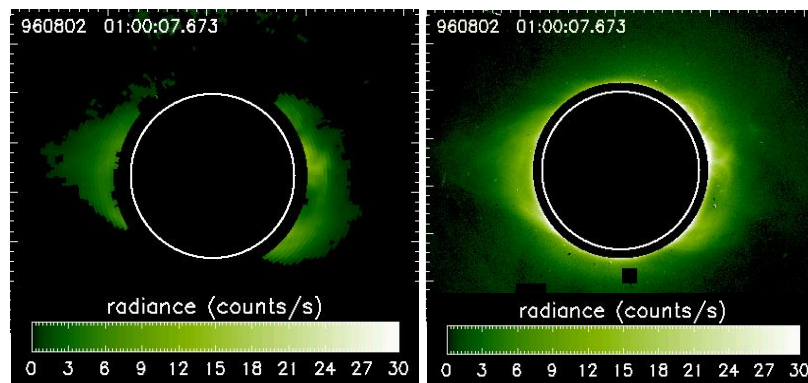
Figure 6.1 The radiance map (left) and the routine data (right) for Fe XIV data as recorded on 2nd of August, 1996. The white color represents a high radiance (more than 30 counts/s). The fit was done over super pixels of 1 degree in azimuthal direction and 4 pixels in radial direction. The white circle indicates the limb of the solar disk.

It is observed that the two images are quite similar. The only difference is the black regions in the radiance map (left). In these regions we could not perform the fit due to the noise. The criteria we use to discard these pixels were explained above.

In order to explain the differences and the similarities between the two images we should outline:

1) The "radiance maps" (i.e. the peak spectral radiances derived from spectral scans with all corrections applied) are the radiances taken at the line center. A disadvantage of this method is that in order to create a map we have to take a full spectral scan (i.e. some amount of time required to record all the needed images).

However, such scans (images at different wavelengths) were taken only once per day. A satisfactory fit, as said above, was not possible everywhere due to the noise.

2) The "routine data" are radiance differences of two images at fixed wavelengths: one at a wavelength near the assumed line center and one at a nearby continuum wavelength. The advantage of this method is that only two images are needed. They are taken several times per hour and only simple evaluation is needed. The disadvantage is that the spectral corrections cannot be performed. We have no spectral information, except the radiance image. Large bulk motions would result in a dimming of radiance in such images, which is difficult to distinguish from simple variations in the local density or temperature.

The green corona consists of loops (west side) which are associated with active regions located near the equator (see Figure 6.1). As the Sun is at the minimum of activity these loops are not the dominant features. We can see the dark regions above the poles as being of a larger extent. These regions are the coronal holes as we mentioned in Chapter 1. Their signature is the lack of the Fe XIV radiation. This is because the temperature is too low for these ions to form. In general the coronal holes are characterized by low electron density (Doschek et al. 1977, Banerjee et al. 1998) and by low temperatures (Wilhelm et al. 1998).

In the red corona (Figure 6.2), the lower formation temperature (1 MK) allows different features to be seen compared with the green corona from the same day. Now the coronal holes are no longer seen and the red corona extends all around the limb. The cooler regions (like polar plumes) can be seen in the red radiance maps.
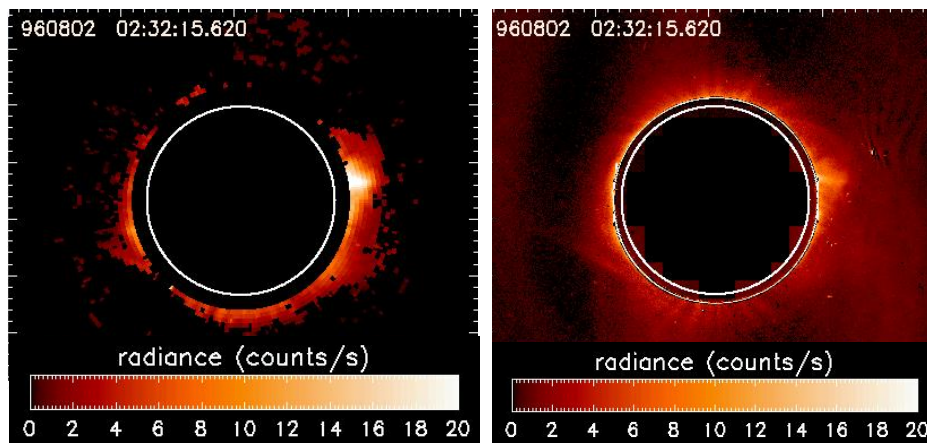
Figure 6.2 The Fe X radiance map (left image) and routine data (right image). The data were recorded on 2nd of August, 1996.

The difference between the two images is quite notable. Due to the low count rates the fitting procedure did not work. We can see the plumes only at the south pole in the radiance map.

For the green corona in 1998 (see Figure 6.3) the active regions are more numerous as the Sun approaches the maximum of activity. The coronal holes are still present but to a smaller extent compared with the green corona in 1996. We see the active regions as bright loops (see the west limb) and the base of the streamers (south east and west side of the limb). Now the radiances are larger compared with those in 1996 (see the color bars) as the Sun is on the ascending phase of activity.
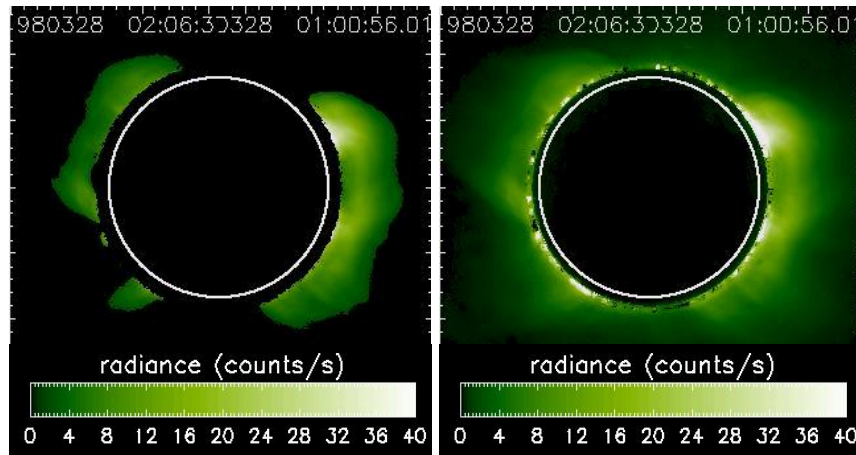
Figure 6.3 The Fe XIV radiance map (left image) and routine image (right image).They are composites of the east and west images taken separately. The data were recorded on 28th of March, 1998. The fit is done for each pixel in the image.

The radiances are higher than those of the green corona in 1996. Again, the red corona displays different features than the green corona in the same period of time. The hot loops (around 2 MK) (see Figure 6.3) are not anymore seen in the cooler line of Fe X (around 1 MK) (Figure 6.4).
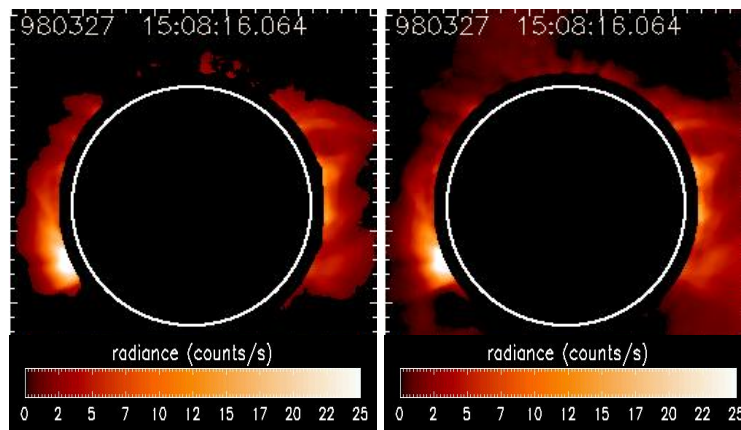
Figure 6.4 The routine (right image) and radiance map (left) for Fe X data recorded on 27th of March, 1998.

In this case there is not much difference between the two images. We cannot evaluate the spectra to large distances, because of increasing noise (see the dark regions on the radiance map). Compared with the green corona at the same period we observe very well the active region on the south-east part, where it shows high intensity. This active region is not seen in the Fe XIV radiance map indicating lower temperatures.

6.1.2 Speed Maps

For each pixel in a data set we determined the shift of the emission line relative to a reference position. This shift is interpreted as Doppler shift, indicating a velocity component of the plasma volume along the line of sight (LOS). From these speed values from each pixel, we construct "speed maps". We show examples of both Fe XIV (Figure 6.5) and Fe X (Figure 6.7) speed maps, from 1996 and 1998.
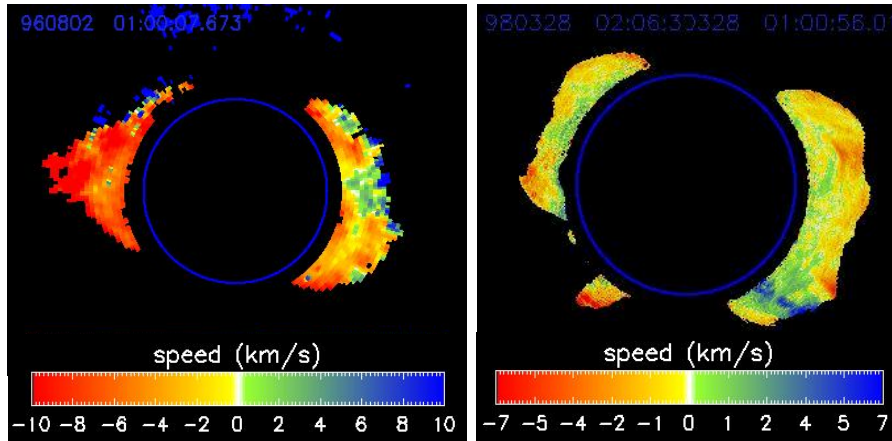
Figure 6.5 The speed maps for Fe XIV data on 2nd of August 1996 (left image) and 28th of March 1998 (right image). The blue circle indicates the limb of the solar disk. These images were corrected for the rotation of the corona. The fit for data in 1998 is done for each single pixel, while for the data in 1996 the fit is done for superpixels.

The figures show with blue and green colors motions towards the observer and with red and yellow colors motions away from the observer. White color indicates plasma with speeds along the line of sight around 0. The speed maps show in general speeds in the range -7 km/s to +7 km/s. The uncertainties in evaluating the speeds are of around 3 km/s (see the discussions in the previous chapter).

For the speed map in 1996 (left image in Figure 6.5) we observe a strong red shift on the east limb. This is due to a backward streamer. In 1998 we see a strong blue shift at the SW limb, like from a narrow jet (right image). This will be discussed in detail in Section 6.3.

Examples of Fe X speed maps in 1996 and 1998 are shown in Figure 6.6.
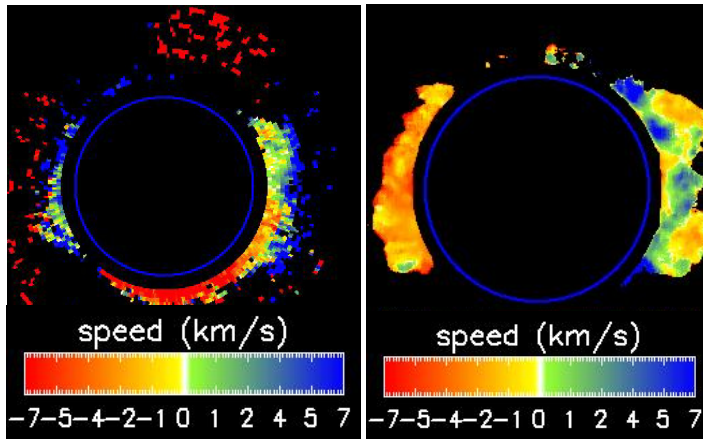
Figure 6.6 The speed maps for Fe X data in 1996 (left image) and 1998 (right image).

It is observed that the Fe X maps in 1996 are much more noisy than those in 1998. For the data in 1996 the strong red shift seen at the south pole is probably an artefact due to the generally low intensities of the red line.

6.1.3 FWHM Maps

For each pixel (data in 1998) or superpixel (1996) in a data set, the width of the line where the radiance is half of the maximum value (FWHM) was determined. These line widths were then assembled in "FWHM maps".

The FWHM maps give us information about the temperatures and turbulences taking place in the solar corona.

Brueckner (1975) and others found line widths in the solar atmosphere in excess of the thermal broadening expected from a temperature at the maximum of the ionic fraction. They introduced a non-thermal velocity contribution, ξ, such that the FWHM (for Gaussian profile and after correcting for the instrumental profile) of an emission line can be written as

$$FWHM = \left\{ 4\ln 2 \cdot \frac{\lambda^2}{c^2} \cdot \left(\frac{2kT_{ion}}{M_{ion}} + \xi^2 \right) \right\}^{1/2} = \left\{ 4\ln 2 \cdot \frac{\lambda^2}{c^2} \cdot \left(\frac{2kT_{ion,eff}}{M_{ion}} \right) \right\}^{1/2} \qquad (6.1)$$

$T_{ion,eff}$ is defined as "effective ion temperature", k is the Boltzmann constant and M_{ion} is the mass of the ion. In order to see how the FWHM varies we show examples of maps taken at different periods of time. We should say that a FWHM at around 0.7 Å for Fe XIV corresponds to an effective ion temperature of around 2 MK. A FWHM of 0.6 Å for Fe X is equivalent with 1 MK. As these are the temperatures at the maximum of ionic fraction for the 2 Fe lines, higher values reflect the non-thermal contributions to the profile of the line. Figure 6.7 and Figure 6.8 show Fe XIV and Fe X FWHM maps, respectively. The red color means large widths and blue colors means narrow line widths (see the color bars).
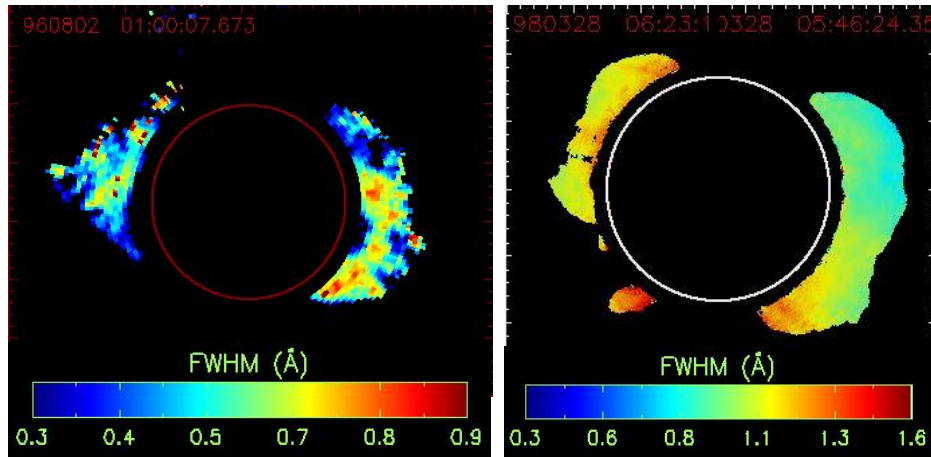
Figure 6.7 FWHM maps for Fe XIV data on 2nd of August 1996 (left image) and 28th of March 1998 (right image).

In general, the corona in 1998 is "hotter" than the corona in 1996. For the data in 1998 it is noticed that closed magnetic structures, (loops) (see Figure 6.3) contain cooler gas (bluish color at west limb in the right panel of Figure 6.7: around 0.5 Å) than open magnetic features (reddish color at south-west limb – around 0.8 Å). For these structures a decrease of the FWHM with height is observed.

Examples of Fe X FWHM maps are shown in Figure 6.8.
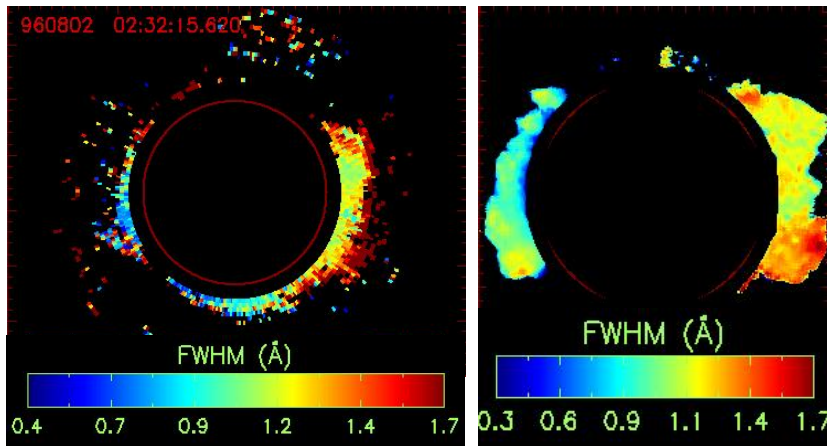
Figure 6.8 FWHM maps for Fe X data on 2nd of August 1996 (left image) and 27th of March 1998 (right image).

For Fe X data an increase of FWHM with height it is observed for the majority of the polar angles. A discussion of this behaviour is given in the next sections.

In order to allow quantitative interpretation of the emission line parameters we make cuts, both radial and polar for the radiance, speed and width. They will be discussed in the next section.

6.2   Interpretation of Emission Line Parameters

In order to allow a quantitative interpretation of the emission line parameters we discuss in the following:

a)   radial cuts in different regions of the corona

b)   polar cuts for different features in the solar corona

c)   variation of the parameters in time for a given region in the solar corona

The results are presented for both Fe XIV and Fe X, in the two periods of time: 1996 and 1998.

6.2.1 Radial Cuts

a) Data in 1996

In the following plots we show examples of radiance, speed and line width versus radial distance for Fe XIV and Fe X data of 1996. For the first example, we choose the "quiet Sun", when no bright regions are seen at the limb (see Figure 6.9).
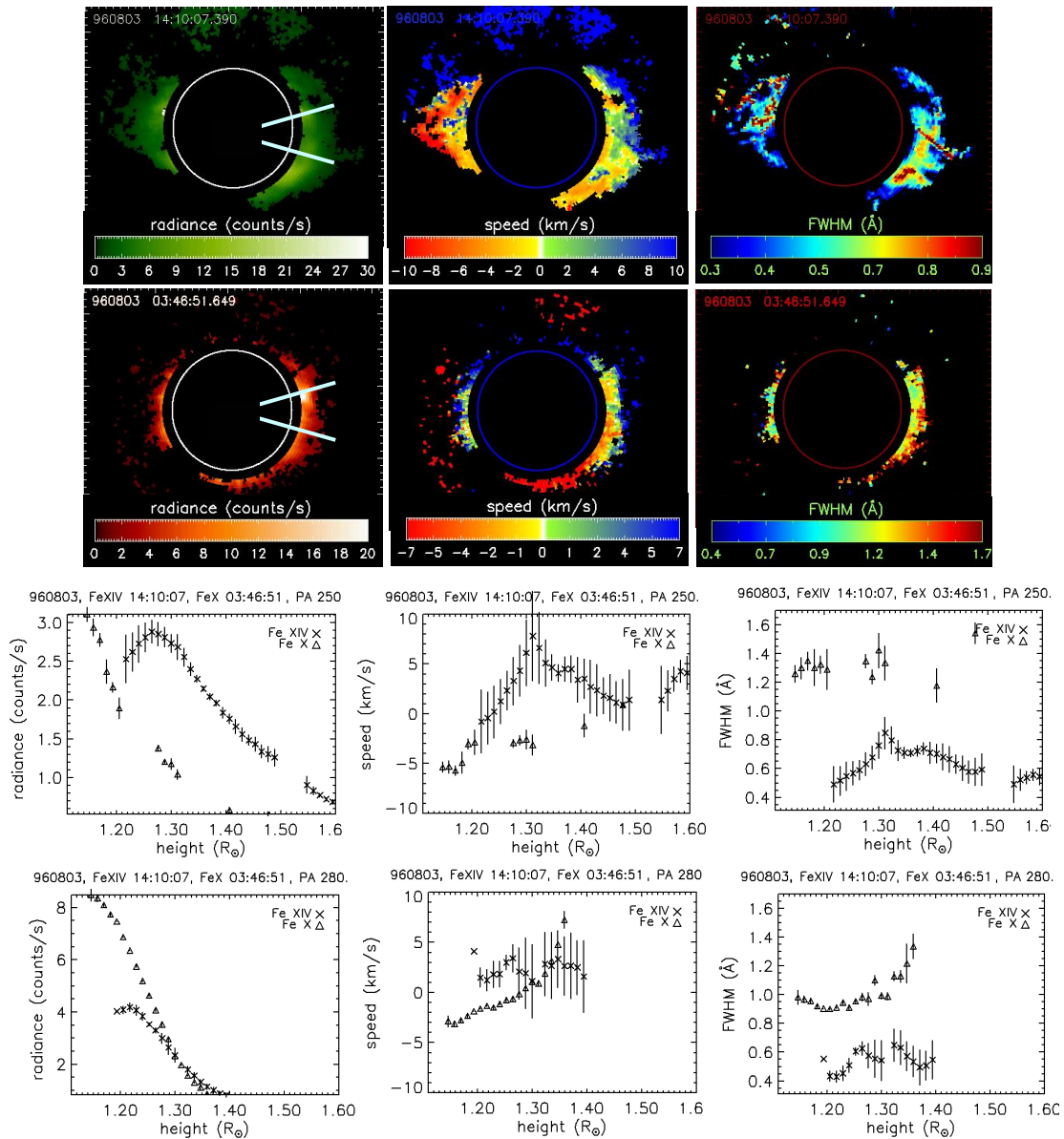
Figure 6.9 Fe XIV (upper 3 panels) and Fe X (the 3 panels right below) maps of radiance, speed, and FWHM for the data sets recorded on 3rd of August 1996. The radial plots of the emission line parameters were taken along the blue lines (see upper panels) and are shown in the 6 plots at the bottom.

We observe in Figure 6.9 (upper panels) rather low values of the radiance, as no bright active region is seen at the limb. The Fe XIV radiance at PA 250 (the lower blue line) first increases with radial distance, then it decreases. This is the signature of a loop with a dark cavity inside. At the top of the loop the speeds are around 5 km/s and outside the loop the speeds are around 0 km/s with an exception of -5 km/s near the limb. This can be due to different motions inside and outside the loop. It is noticed that inside the loop the FWHM is larger than outside (lower right panel). The Fe XIV FWHM is increasing with distance up to 1.3 $R_\odot$ and then it is decreasing. Fe X points at PA 250 are too few for determining significant trends, due to low radiances. At PA 280 there is a steep decrease of Fe X radiance with height. The line of sight speeds are around 0 km/s. For Fe X FWHM we observe an increase with height.

In the next sections we study some loops in order to understand these motions better.

At first, we choose a data set from 1996 with an active region on the limb (see Figure 6.10).
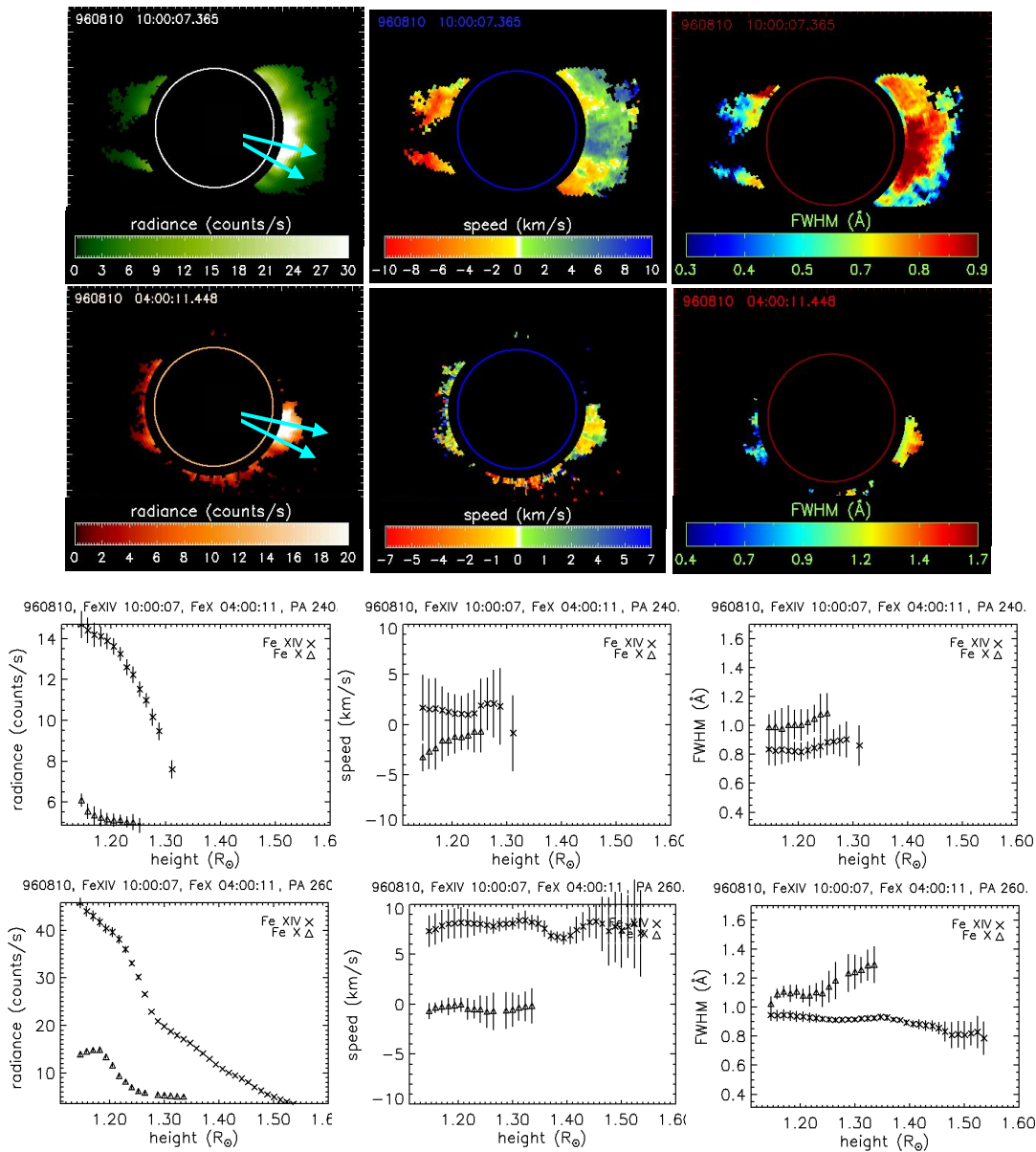
Figure 6.10 Fe XIV (upper 3 panels) and Fe X (the 3 panels right below) maps of radiance, speed, and FWHM for the data sets recorded on 10th of August 1996. The radial plots of the emission line parameters were taken along the blue lines (see upper panels) and are shown in the 6 plots at the bottom

For the two polar angles (one at the edge of the AR and one for the AR itself) the Fe XIV radiance is higher than that of Fe X. The count rates are higher this time (up to 40 counts/s). For PA 240 the speeds of Fe XIV and Fe X ions are around 0 km/s. The FWHM of the two species are increasing with the radial distance. For the AR we see speeds around 10 km/s for Fe XIV ions, and around 0 km/s for Fe X. The Fe X FWHM is again increasing with height while the Fe XIV FWHM is decreasing with the radial distance.

For the data in 1996 we have in general speeds in the range - 10 to + 10 km/s. The Fe X FWHM seems to increase all around with height while the Fe XIV FWHM is decreasing with height in the active regions.

b) Data in 1998

For the Fe XIV data in 1998 we show 2 examples of 28th and 29th of March, each having 2 radial cuts. The examples on 28th of March show 2 cuts for a region without AR (PA 216) and for an AR (PA 296) (see Figure 6.11).
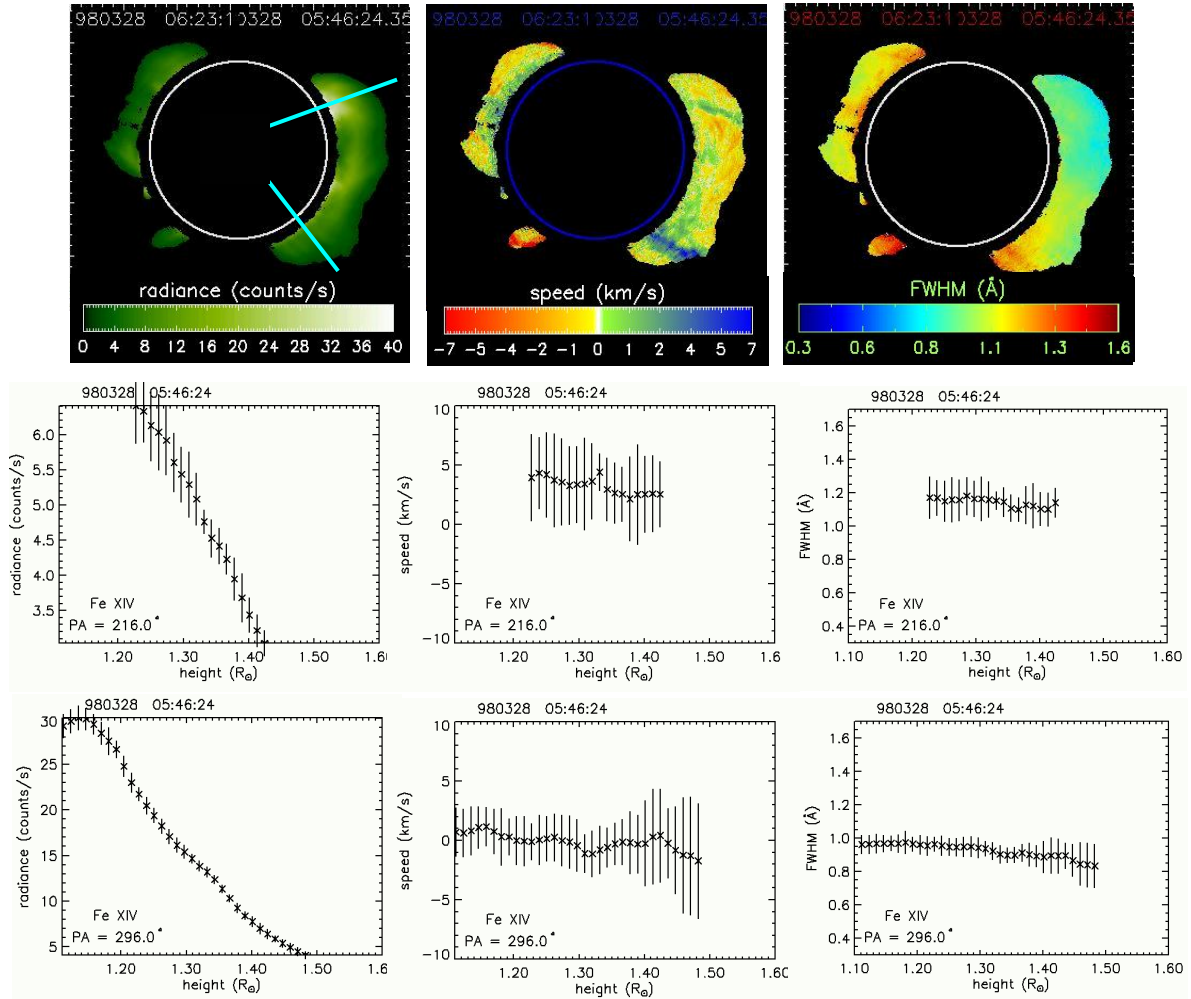
Figure 6.11 Fe XIV maps of radiance, speed and FWHM for the data set recorded on 28th of March 1998 and two radial cuts as indicated by the blue lines.

From Figure 6.11 we find that the radiance in the active region (lower left plot) is 5 times higher than the radiance in the streamer (upper left plot). The steep decrease of the radiance with height at PA 216 is due to the fact that the streamer is not radial and the cut just passes through a part of the streamer. Speeds up to 5 km/s are observed. In the case of the AR, the speeds are around 0 km/s (see the middle panel in lower row). In both cases the FWHM is decreasing with radial distance.

If we make radial cuts for a data set where a back side CME had occurred (this will be discussed in Section 6.5) we obtain the plots of Figure 6.12.
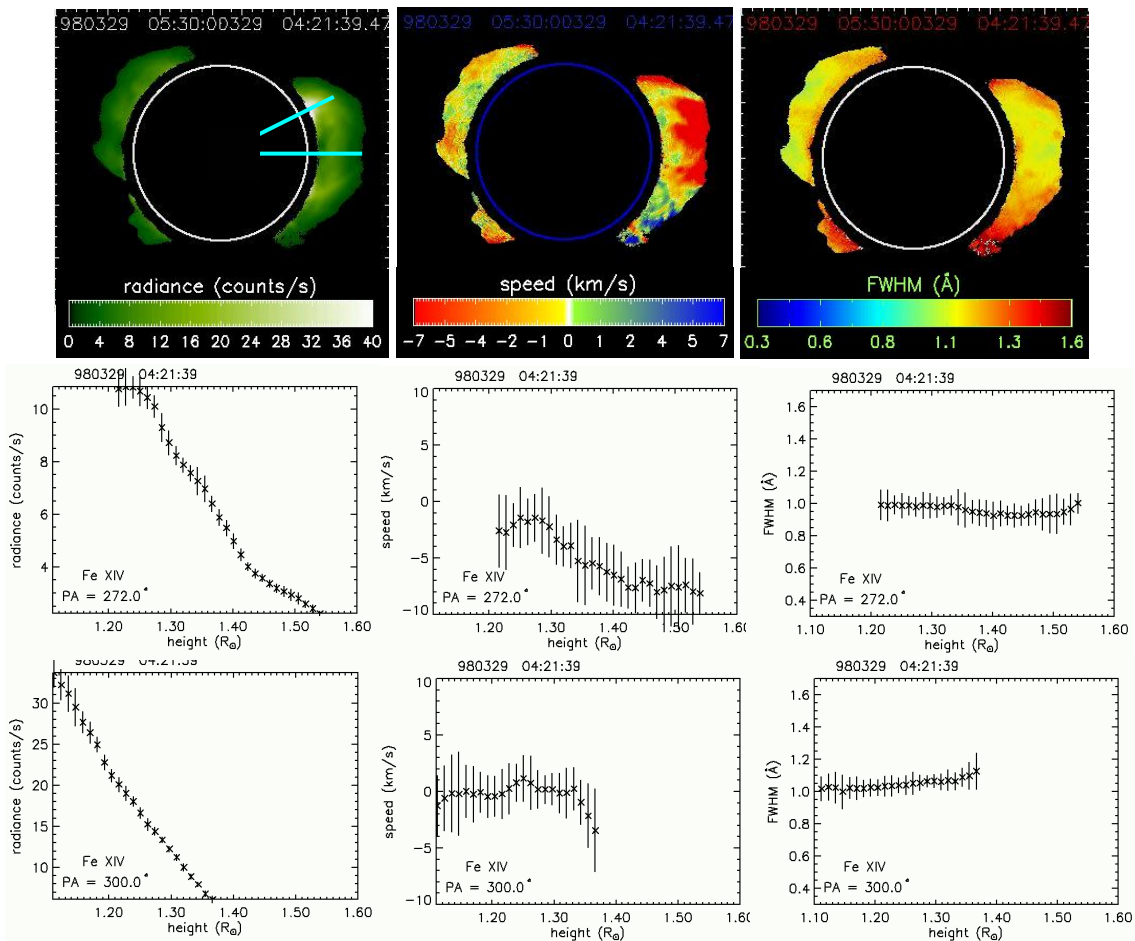
Figure 6.12 Fe XIV radiance, speed and FWHM maps for the data set recorded on 29th of March 1998 plus 2 radial cuts as indicated by the blue lines.

For PA 272 we find lower values for the radiances compared with the AR at PA 300. The plasma is moving away from the observer with speeds up to -10 km/s, at PA 272. In the case of the AR the speeds are around 0 km/s. The FWHM is slightly decreasing with height for PA 272 and it increases at PA 300.

For Fe X data we show one example from 27th of March 1998 (Figure 6.13).
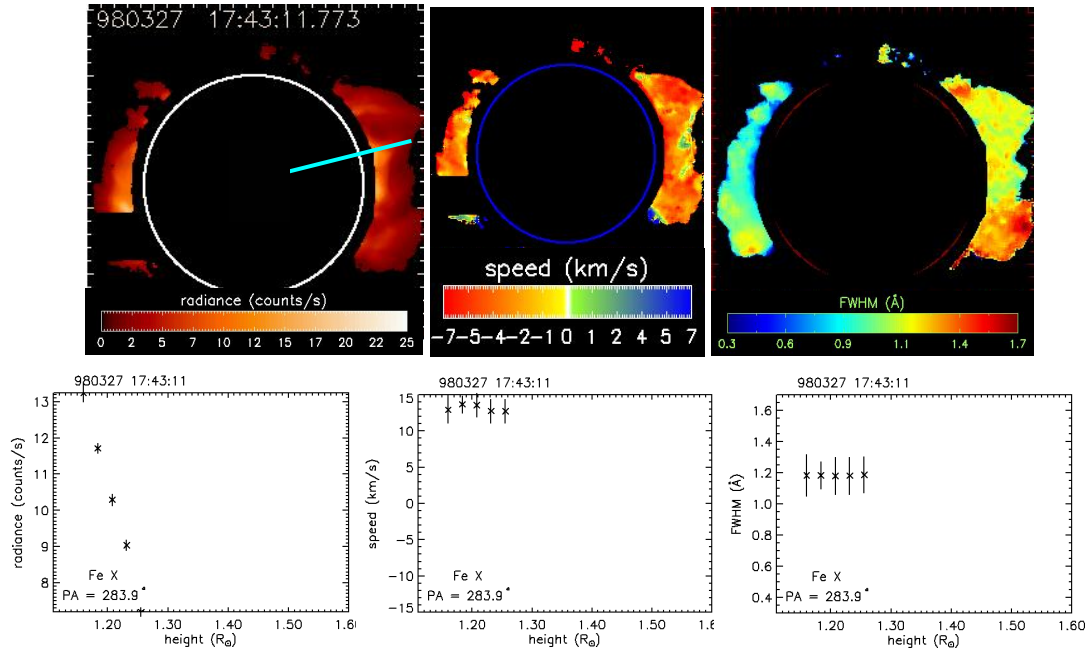
Figure 6.13 Fe X radiance, speed and FWHM maps for the data set recorded on 27th of March 1998 plus one radial cut as indicated by the blue line.

For Fe X data in 1998 we see that the speeds are around 15 km/s. The FWHM is constant in the range 1.1 to 1.28 $R_\odot$.

We find that the Fe X FWHM is almost everywhere increasing with radial distance. The Fe XIV FWHM in 1996 shows both an increase with distance, generally for the quiet Sun and a decrease, mostly for AR. Fe XIV FWHM for data in 1998 shows almost in most cases a decrease with radial distance. A statistical evaluation of the line FWHM results will be given in the following section.

The Statistical Behaviour of FWHM with Height for Fe X and Fe XIV Data

In order to analyze the radial profile of the line widths we make radial cuts at a given polar angle. We apply linear fits to the measured FWHMs and determine the slope (tan α) as shown in Figure 6.14. For each data set we make cuts at 6 different polar angles. We plot the slopes of all data sets versus time. The cuts at different PA are shown in different colors. We exclude the points were the correlation coefficient is between -0.5 and 0.5.
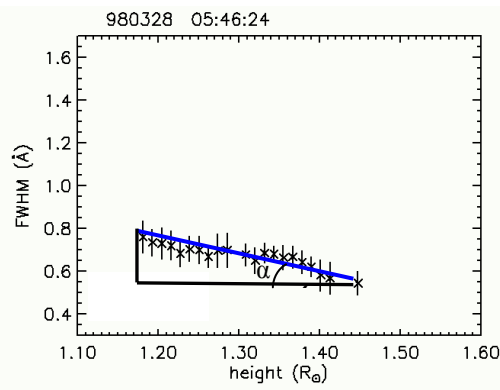
Figure 6.14 Example of a radial cut showing the variation of FWHM with height.

For Fe X data in 1996 we plot the slope in time for the polar angles: 70º, 90º, 110º, 250º, 270º, 290º, as shown in Figure 6.15.

Figure 6.15 The temporal variation of the Fe X slope. The colors represent different polar angles. The continuous line indicates a slope of 0, while the two dotted lines indicate slopes of +/- 0.5 Å/R$_\odot$
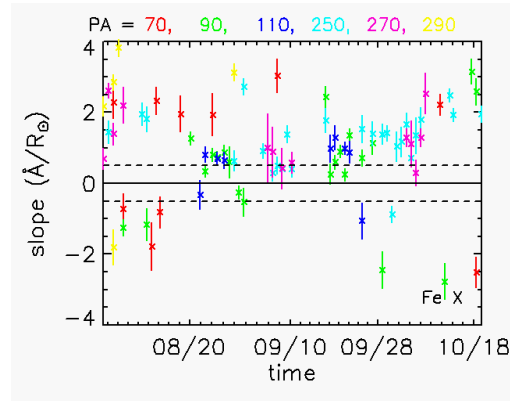
We see that for the majority of the points the slope is positive, i.e. the Fe X FWHM is increasing with radial distance throughout the whole time interval. Only in a few cases the line width is decreasing with radial distance. Inspections of the data lead us to the suspicion that the FWHM of Fe X also depends on the line radiance. In order to study this we plot the slope as function of line radiance for a constant radial distance of 1.2 R$_\odot$. The result is shown in Figure 6.16.
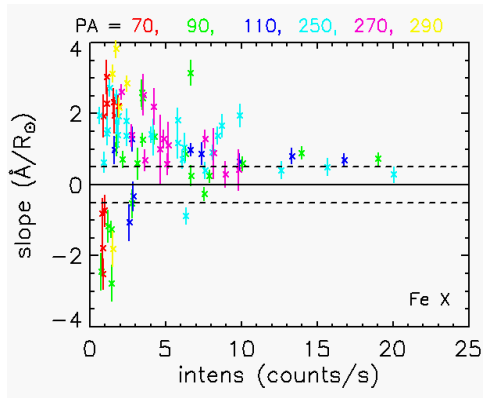
Figure 6.16 The variation of the Fe X slope with the radiance at 1.2 R$_\odot$.

We see that the few negative slopes correspond generally to low radiances.

For the Fe XIV data we plot at first the points in the range 1.1 to 1.3 R$_\odot$ and then 1.3 to 1.5 R$_\odot$ (see Figure 6.17).
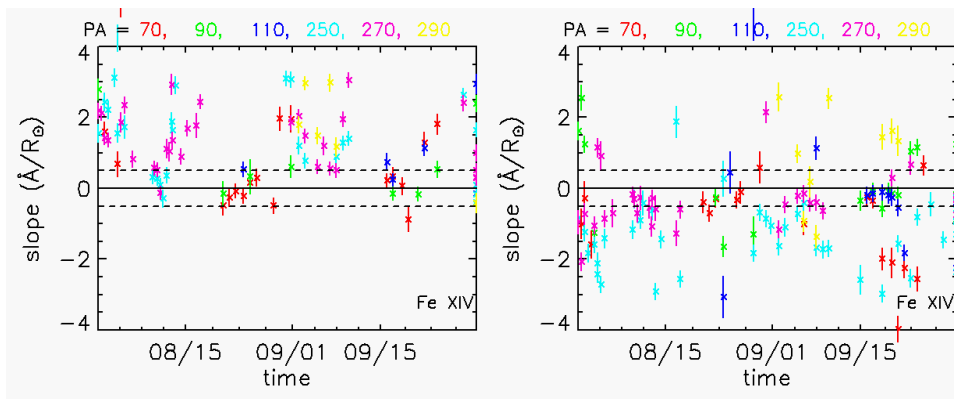
Figure 6.17 The variation of the Fe XIV slope with time. The left panel shows the slopes for the data between 1.1 and 1.3 R$_\odot$ and the right panel, data between 1.3 and 1.5 R$_\odot$.

We see that up to 1.3 $R_\odot$ the slope is generally positive, i.e. there is almost at all times an increase of the FWHM with height. For larger distances however, the FWHM appears to decrease with height.

The slope of Fe XIV versus radiance is shown in Figure 6.18.
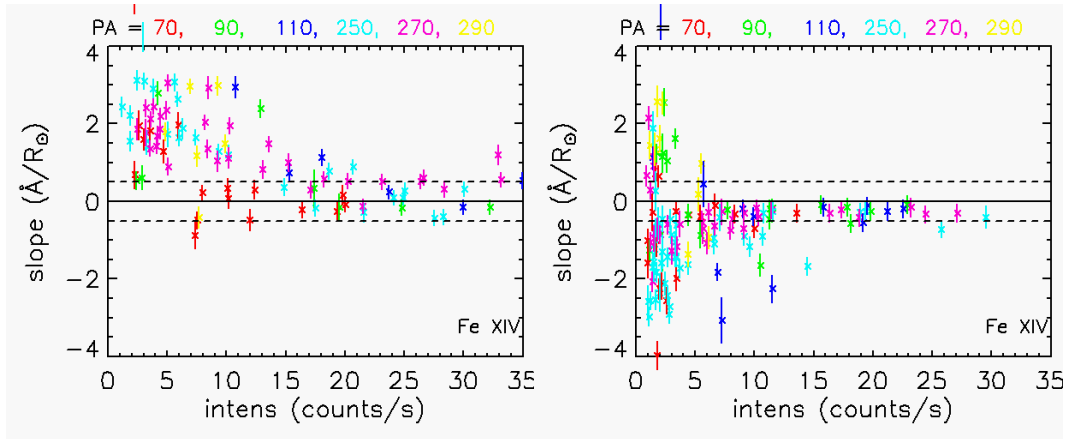
Figure 6.18 The variation of the Fe XIV slope with radiance. The left panel shows the slopes for the data between 1.1 and 1.3 $R_\odot$ and the right panel, data between 1.3 and 1.5 $R_\odot$.

We observe few cases at higher radiances where the slope is negative.

Interpretation: Line of Sight Effects

In order to explain the behaviour of the line width with distance we build a simple model that takes into consideration the effects of the line of sight integrated observations of the emission line profiles.

We consider a corona at constant temperature expanding radially with a constant speed (see Figure 6.19).
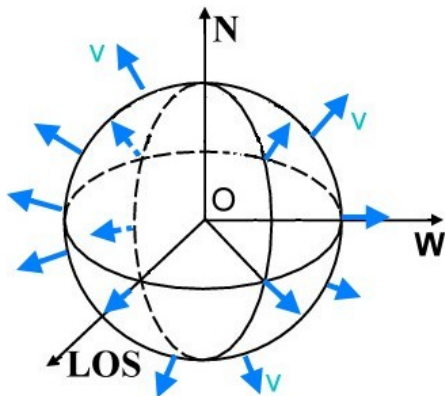
Figure 6.19 Sketch of the solar corona expanding radially. On the line-of-sight (LOS) the speeds at different angles will have different contributions.

For any line of sight, at a given radial distance, the expected emission contains contributions from different radial distances with different Doppler shifts. We assume the radiance to vary with distance as it was actually observed (Figure 6.20). For each line of sight in the distance range between 1.1 $R_\odot$ and 1.36 $R_\odot$ we build an integral over the expected emission for the whole spectral range of the emission line. We repeated this calculation assuming different

plausible values for the radial speed. This way, we obtain the plots shown in Figure 6.20, lower panels.
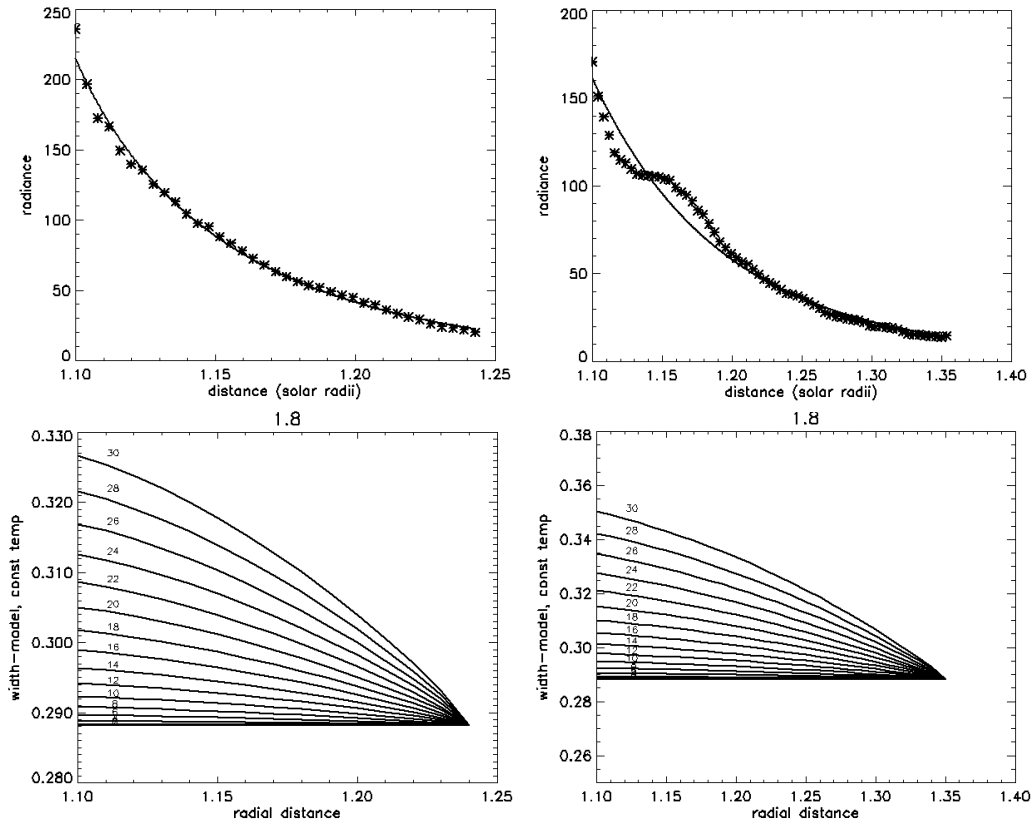
Figure 6.20 Model showing the variation of FWHM with radial distance (lower panels) for different radial speeds and the variation of the radiance with distance (upper panels). A constant temperature of 1.8 MK was considered. The parameters on the curves are the speeds in km/s.

Figure 6.20 shows clearly that for all assumed radial speeds, at a constant temperature the line width should decrease with radial distance. This may be due to the steep gradient of the peak radiance with solar distance. Nevertheless, the decrease is not as steep as we observe in our data. As a consequence, other effects have to be taken into account.

Interpretation: What does Affect the Line Width?

As we mentioned in Chapter 2, spectral lines are not infinitesimally narrow; they have a finite width. There are several causes of line broadening, some internal to the atom, others external, and each one produces its characteristic profile.

The emission line profile, $\Psi(\lambda)$, is formed by the convolution of all the emission profiles generated by the different broadening mechanisms:

$$\Psi(\lambda) = \Psi(\lambda)_{nat} * \Psi(\lambda)_{coll} * \Psi(\lambda)_{th} * \Psi(\lambda)_{nt}$$

At the above effects we add the line-of-sight effect, as explained in the previous section.

The natural broadening in the case of Fe XIV and Fe X forbidden lines (with a level lifetime of around 10^{-4} s (Brage et al. 1996)) is of the order of 10^{-9} Å, i.e. negligible.

The Stark or pressure broadening in the solar corona (electron density of order of 10^{10} cm^{-3}) is also negligible (see Gonzales et al. 1998).

The thermal broadening has a big influence on the line width. In general, observed line profiles in the solar corona are well represented by a Gaussian shape (Mariska 1992). Transition region and coronal emission lines show a width that cannot be explained by only Doppler thermal broadening (e.g. Boland et al. 1973, 1975, Doschek et al. 1976, 1977, Dere and Mason 1993, Warren et al. 1997, Chae 1998, Teriaca 1999).

The potential effects causing line narrowing or broadening with radial distance are discussed in the following.

In general a broadening of the emission line width with radial distance was observed (Hassler et al. 1990, Wilhelm et al. 2004). The explanation given by Hassler et al. (1990), in order to explain the broadening of the Mg X doublet at 609.8 and 625 Å, was the dissipation of the waves in the solar corona. This is due to the drop in pressure with height in the solar corona. Wilhelm et al. (2004) analyze the same line using SUMER data. They found that the Doppler width (i.e. half 1/e width) broadens from around 0.082 Å to around 0.095 Å between the limb and 0.31 $R_\odot$ above the limb in the equatorial corona. In a polar coronal hole, the Doppler width increases from 0.108 Å near 0.04 $R_\odot$ to 0.114 Å at around 0.11 $R_\odot$ above the limb. They do not find any evidence of a narrowing of the emission-line profiles as a function of the distance from the solar limb.

Harrison et al. (2002) reported the narrowing of the Mg X 625 Å line with height in the quiet near-equatorial solar corona using Coronal Diagnostic Spectrometer (CDS/SOHO) data. They conclude that this narrowing is most likely evidence of dissipation of Alfvén waves in closed field-line regions. Using the same data, O'Shea et al. (2003) observed the decrease of the line width with height in polar coronal holes. In the case of Fe XIV line at 5303 Å the only narrowing with the distance above the limb was reported by Singh et al. (1999). In the case of Fe X line at 6374 Å they found an increase of FWHM with height. In order to explain this they suggested that the mixing of plasma in middle and higher portions of the coronal structures by microturbulence may account for this behaviour.

In conclusion, the mechanisms which broaden the lines in solar corona are:
  a) the thermal motions in the solar corona.
  b) nonthermal effects (microscopic motions like waves/turbulence or macroscopic motions like line of sight effects)

These effects may act differently on cooler (Fe X) and hotter (Fe XIV) plasma resulting either in broadening or in narrowing of the line with radial distance.

6.2.2 Polar Cuts

a)   Data in 1996

Now we make polar cuts at a given distance from the limb. We try to see how the speed changes from AR to quiet Sun regions. The first examples are from the Fe X and Fe XIV data in 1996 (see Figure 6.21).

The parameter maps were already shown in Figure 6.9. The polar cut is done at a distance of 1.2 $R_\odot$ (note that the white circle in Image 6.9 is at a distance of 1 $R_\odot$).
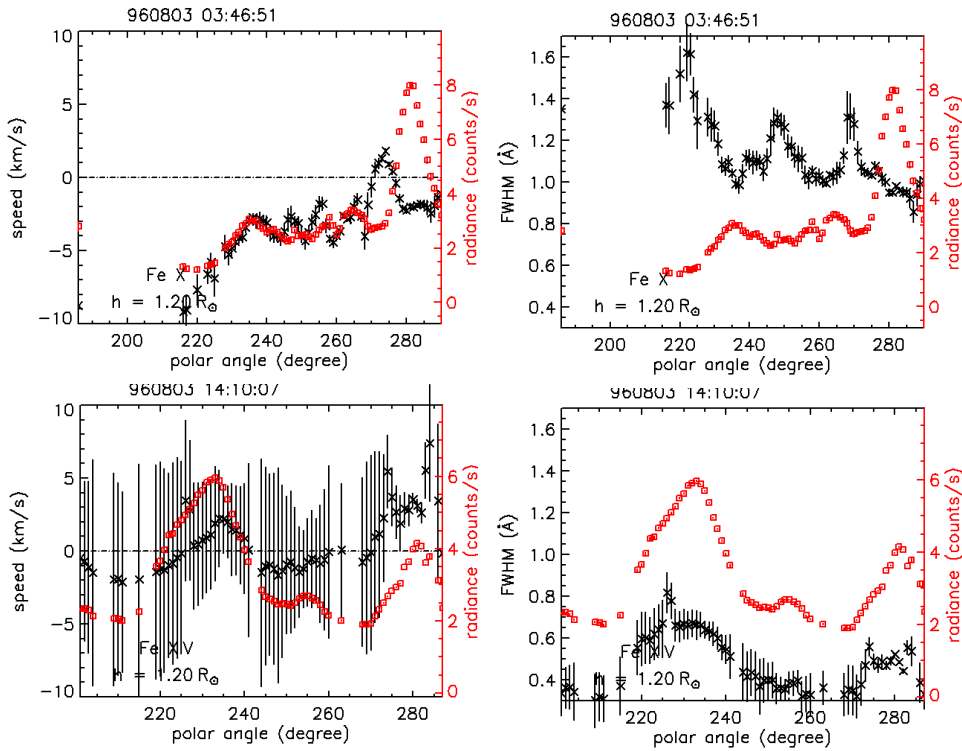
Figure 6.21 Radiance, speed and FWHM polar cuts for Fe X (upper panels) and Fe XIV (lower panels) data at a distance of 1.2 $R_\odot$ from the Sun center. The data are recorded on 3rd of August 1996.

We show both speed and radiance polar cuts. Note that the red (Fe X) and green (Fe XIV) corona exhibit different intensity features (cf. also Figure 6.9). The intensities are generally small (around 8 counts/s) as there were no bright active regions present at this time. The intensity varies dramatically with polar angle for both the Fe X and Fe XIV plots. The line of sight speeds for Fe XIV alternate between positive and negative values; for Fe X they are mostly negative (i.e. plasma seems to move away from the observer). We observe that the Fe XIV plasma is "cooler" than the Fe X one. The Fe XIV FWHM shows a good correlation with the radiance, while the two quantities for Fe X are anticorrelated in some regions (Figure 6.21, right panels).

In order to see the effective temperatures we transform the values from Å to K as described in Equation (6.1). The results are shown in Figure 6.22.
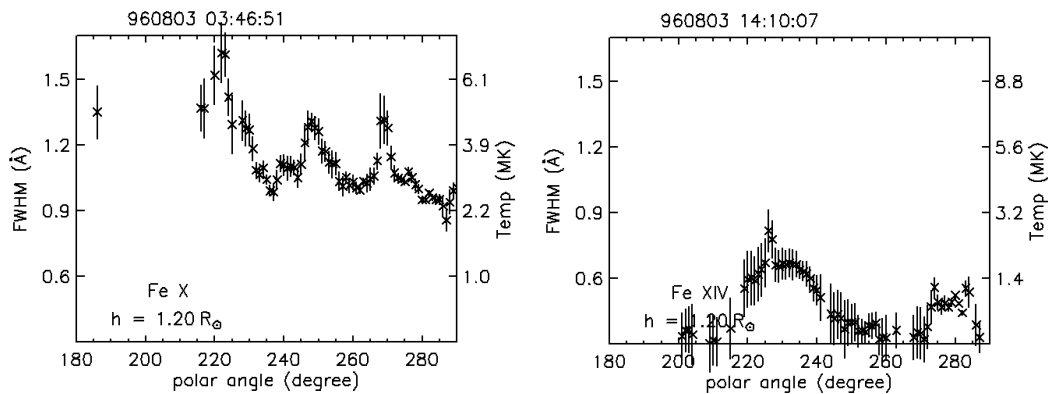
Figure 6.22 FWHM polar cuts for Fe X (left panel) and Fe XIV (right panel) data at a distance of 1.2 $R_\odot$ from the Sun center. The data were recorded on 3rd of August 1996. The right side y-axis shows the effective temperature of the ions.

Apparently, the effective temperatures are higher in the "red" (cooler) corona, compared to the "green" (hotter) corona. That means that the amount of turbulence is higher in the cooler plasma. In Figure 6.23 we show the emissivity of the 2 lines as function of temperature.
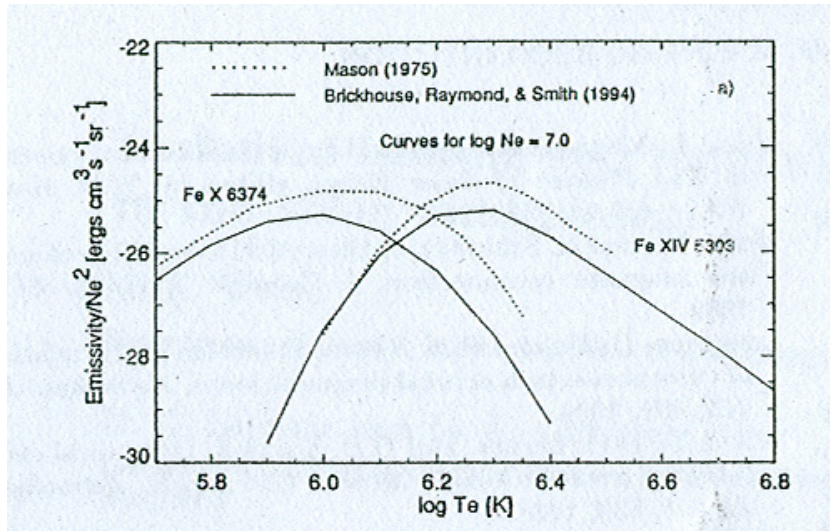
Figure 6.23 Emissivity of the Fe X 6374 A and Fe XIV 5303 A spectral lines as a function of the logarithm of the temperature for 2 different atomic models (Esser 1995).

From Figure 6.23 we learn that the peak temperature formation for Fe XIV emission is at around 2 MK while for Fe X it is around 1 MK. At lower temperatures (around 1.3 MK) there is still emission in the green line. Note that the temperature at which both lines have the same intensity is between 1.3 and 1.4 MK.

Next, the case with the very bright active region on the west limb (10th of August 1996) is investigated (see Figure 6.24).
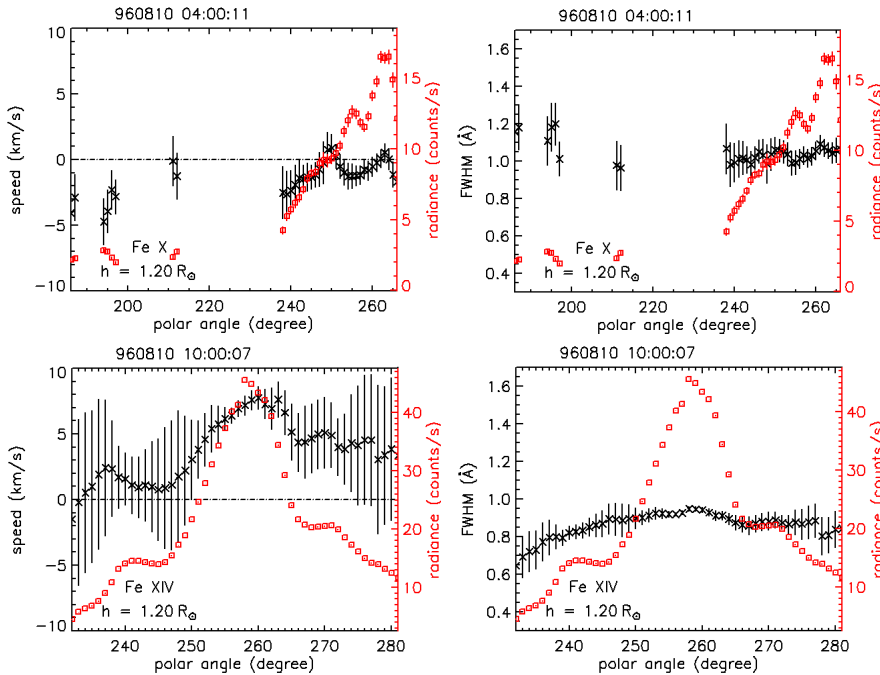
Figure 6.24 Polar cuts for radiance, speed and FWHM for Fe X (upper panels) and Fe XIV (lower panels) data as recorded on 10th of August 1996.

Of course, the high intensities occur where the active region is (at the west limb). The Fe XIV speeds go up to 8 km/s in the AR while the Fe X speeds are around 0 km/s. The FWHM is about constant all through the active region.

b)   Data in 1998

For Fe XIV data in 1998 (see Figure 6.13) we show 2 examples of polar cuts for the west limb.
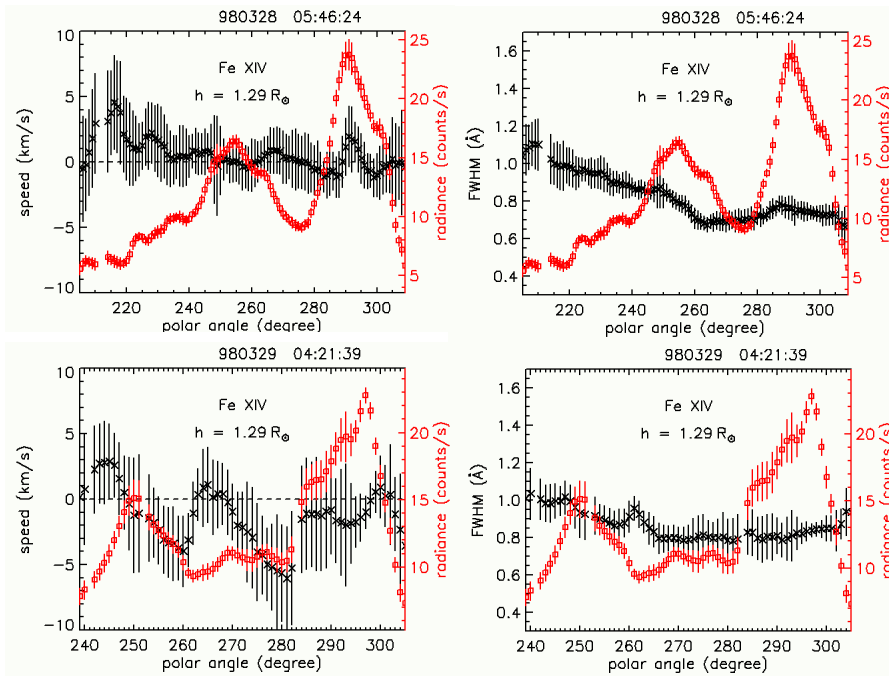
Figure 6.25 Polar cuts for radiance, speed and FWHM of Fe XIV data recorded on 28th (upper panels) and 29th (lower panels) of March 1998.

We see again in the radiance plots a strong variance with polar angle. The speeds for the data on 28th of March are around 0 km/s. For 29th of March we find significant negative speeds that are consistent with a backside CME that happened to occur right at this time. A more detailed discussion will be presented in Section 6.5. Larger widths are observed outside the ARs compared with the ARs themselves.

We do not present any example of Fe X data in 1998 because too many points are missing due to very low radiances.

The Evolution of the Emission Line Parameters in Time

Now we study the time variations of radiance, speed, and FWHM in different regions of the corona for both Fe XIV and Fe X for two time periods in 1996 and 1998.

The first example shows Fe XIV data in 1996. The speed and the FWHM are plotted in Figure 6.26 in the same graphic as the radiance in order to reveal potential correlations.
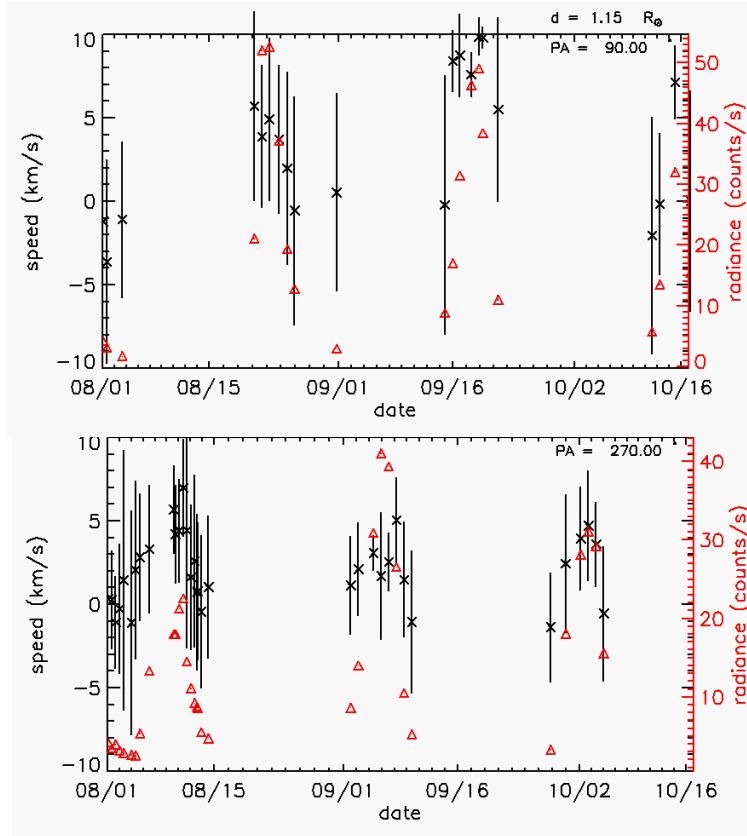
Figure 6.26 Radiance (red) and speed (black) versus time for east limb (upper panel) and west limb (lower panel) for Fe XIV data recorded on August-October 1996.

In the radiance plots we notice major variations with time. Naturally, radiances are high when an AR is passing the limb. We further note an apparent anticorrelation between the intensities at the two limbs. In this period of time there was only one bright active region. When the AR is at the east limb the radiance at the west limb is usually low, and the other way around. The speeds show the flow of the plasma towards the observer when the streamer (or AR) is near the limb. Upon inspecting EIT images in that period we notice that the AR has at its flanks 2 coronal holes (CH) (Figure 6.27).

.
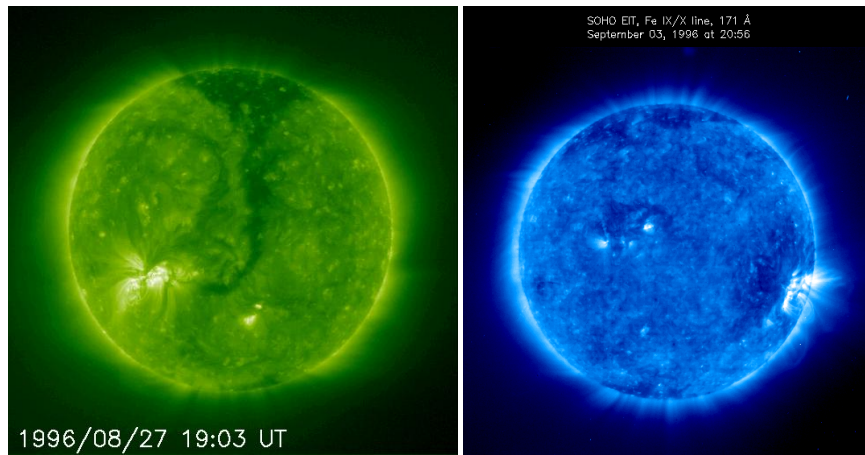
Figure 6.27 (EIT) full-field Fe IX, X 171 Å, (blue) and Fe XII 195 Å (green) on 27th of August (left) and 3rd of September (right) 1996. The right image is from NASA Goddard Space Flight Center.

The EIT image at 195 Å (left panel in Figure 6.27) shows a coronal hole at the right side of the AR. This is the famous "elephant's trunk" coronal hole (Del Zanna, 1999) that had been the subject of several studies in the Whole Sun Month (see Gibson et al. 1999). The other EIT image (right panel) was taken 7 days later, so that the Sun had rotated by about 105º. It shows now the same active region closer to the west limb plus another coronal hole bordering it on its west side. It looks as if the plasma flows at the interface between the AR and the two coronal holes. When the AR approaches the limb the flow speed as determined by our spectral analysis of Fe XIV data is showing an increasing blue shift. Our interpretation is that at first we see the plasma flowing at the interface between the right side CH and the AR. When the AR is almost at the limb we see the flow between it and the second CH. This speed is maximum when the AR is right at the limb. Afterwards the flow goes to 0 km/s as the second CH approaches the limb and it turns negative when the interface between the two regions reaches the back side of the limb.

In Figure 6.28 we show the variation of the FWHM with time for the same regions as in Figure 6.26.
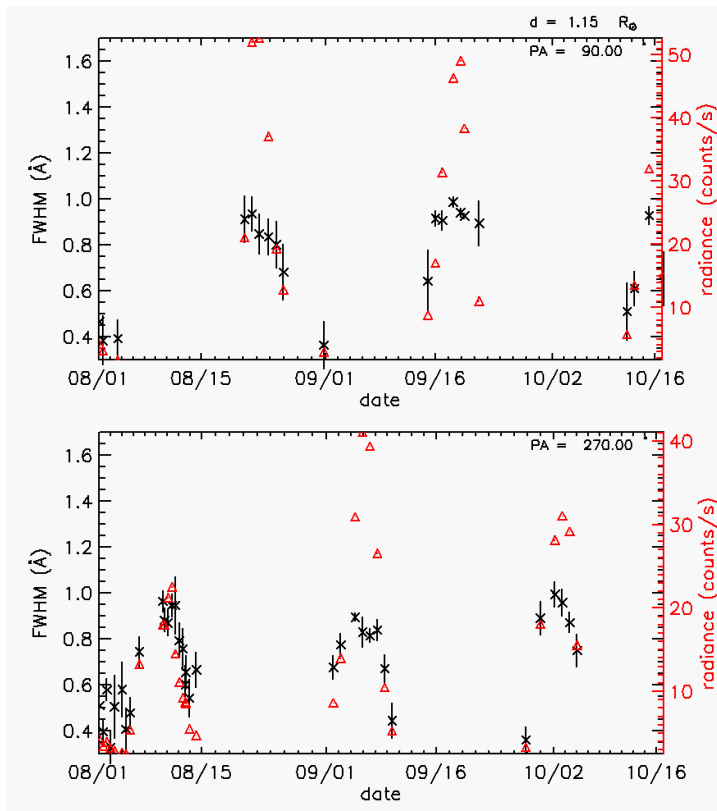
Figure 6.28 Radiance and FWHM versus time for east limb (upper panel) and west limb (lower panel) for Fe XIV data recorded on August-October 1996.

Figure 6.28 demonstrates clearly the brighter an AR near the solar equator is, the higher is its "effective temperature".

For the Fe X data in 1996 we show similar examples as for Fe XIV (Figure 6.29).
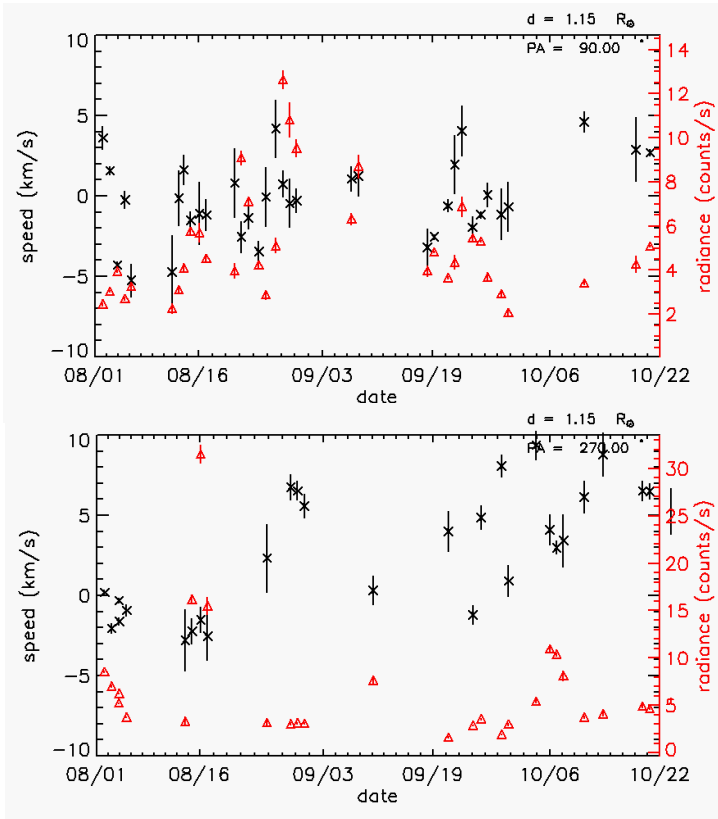
Figure 6.29 Radiance and speed versus time for east limb (upper panel) and west limb (lower panel) for Fe X data recorded on August-October 1996.

We find a similar modulation of the radiance with time as we did for Fe XIV. The speeds are around 0 km/s when the AR is at the limb.

The Fe X radiance and FWHM versus time are shown in Figure 6.30.
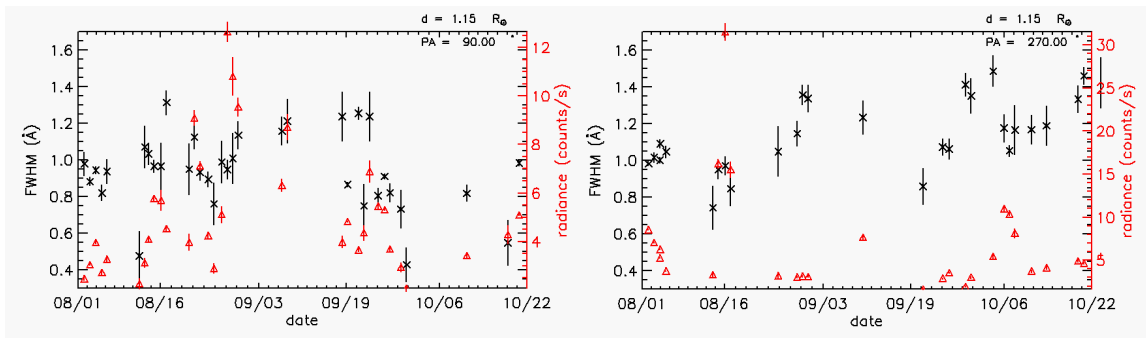
Figure 6.30 Radiance and FWHM versus time for east limb (left panel) and west limb (right panel).

It appears as the FWHM is fairly constant at around 1.2 Å throughout the whole time period, on both limbs.

No correlation can be observed between the FWHM and the radiance.

The Fe XIV data in 1998 were taken every 15 minutes, alternatively at the west or east limb, respectively) during the period $28^{th} - 30^{th}$ of March. We show the variation in time for the emission line parameters for two regions (both on the west limb) in the solar corona, in Figure 6.31.
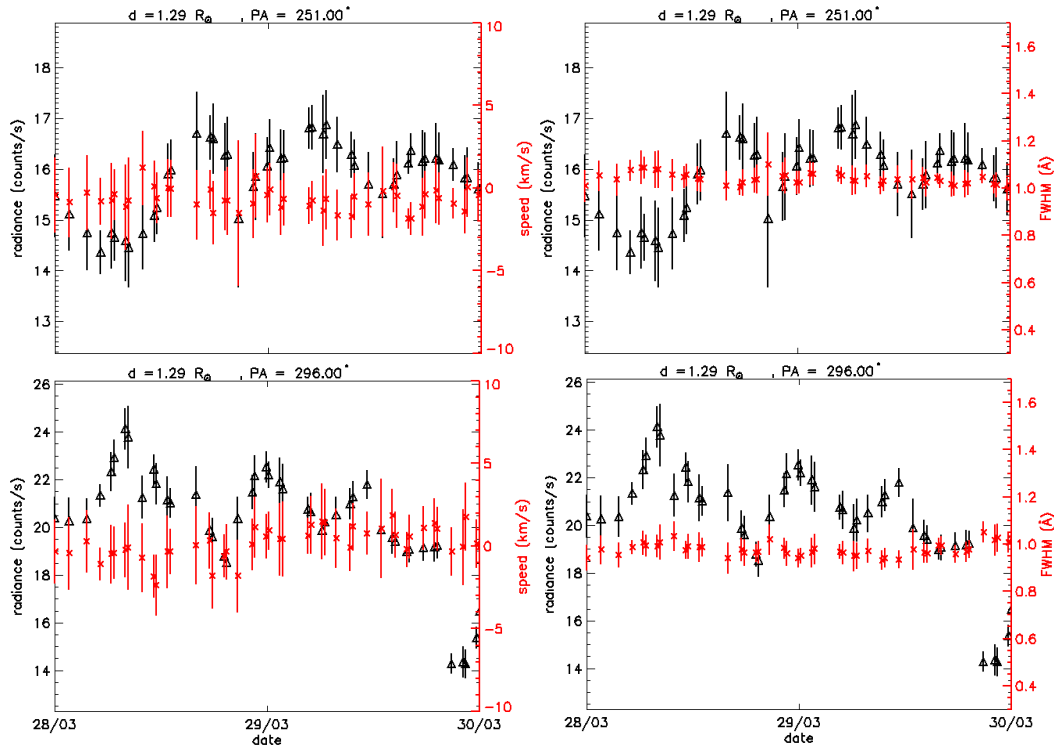
Figure 6.31 Radiance (black), speed (left, red) and FWHM (right, red) versus time of Fe XIV data for 2 different regions above the west limb in the solar corona.

We find that the speeds are in general around 0 km/s. The radiances for PA 296 (in the lower plots) are generally higher since at that PA there happened to be a bright AR.

At around 12:00, on 28th of March a decrease of the radiance is observed at PA 296. This is due to the depletion of plasma after the passage of a CME observed at 12:08 in the C2 field of view. We further note that the FWHM did not change much over the 3 days considered here.

6.3   Slow Solar Wind

The strong blue shift seen on speed maps on 28th of March 1998 (see Figure 6.11) is due to a streamer originating on the visible part of the Sun disk. In order to demonstrate this we check EIT and C2 images around this period. Here we show 2 examples of combined images in order to point where the streamer probably originated (see Figure 6.32).
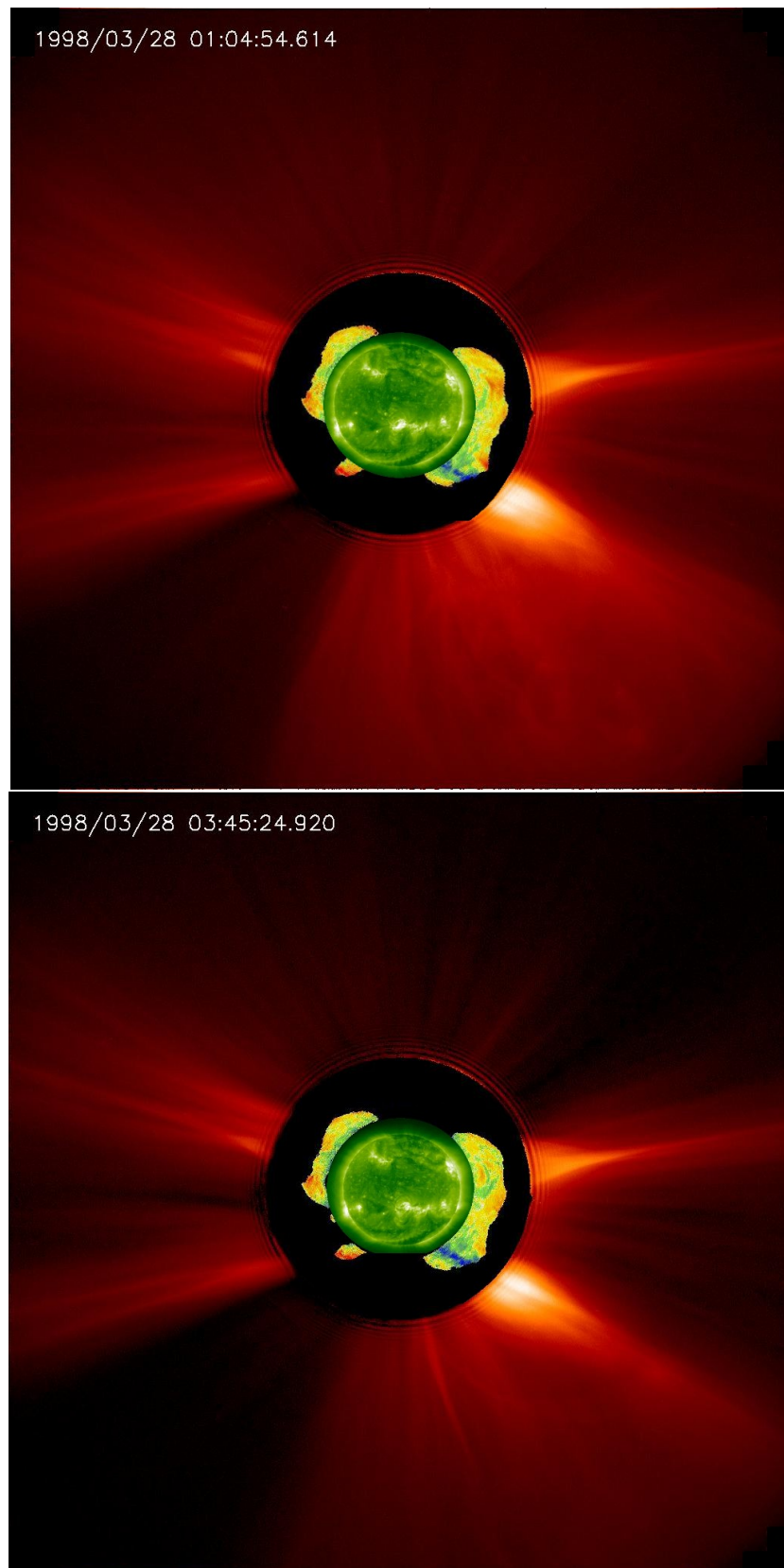
Figure 6.32 Combined EIT, C1 speed map and C2 images for data recorded on 28th of March 1998, at 2 different times.

In Figure 6.32 we see the continuation of the strong blue shift in the C1 speed map with the streamer in the C2 image. In the upper panel, at 01:04 UT the blue shift is less strong than in the

lower panel, at 03:45 UT. We can see very well the separation between 2 bright regions of the streamer in the C2 part of the lower panel. This separation cannot be seen in the upper panel taken 2 hours earlier. We conclude that the configuration of the magnetic field was changing such that plasma was allowed to escape. As the association between the flow and the streamer is very clear from the images above, we conclude that the plasma outflow from there is indeed related with the streamer.

In order to localize the region on the Sun from where the streamer originates, we trace back the flow seen in the C1 speed map to the EIT image. It seems that the flow originates at the interface between the active region and the CH as indicated in the left panel of Figure 6.33.
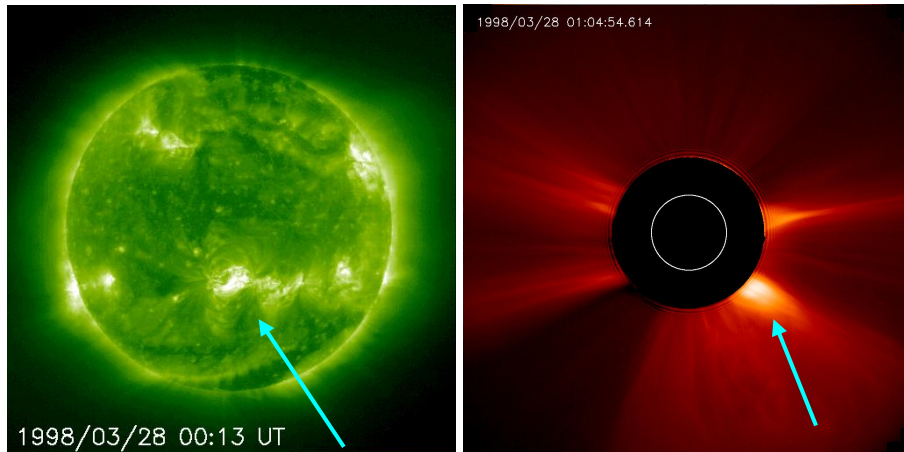
Figure 6.33 LASCO/EIT (left panel) and LASCO-C2 (right panel) images taken on 28th of March 1998. The white circle in C2 image indicates the disk of the Sun.

The EIT image shows two active region belts at middle latitudes north and south of the solar equator. The streamer seen in the south west side of the Sun in the C2 image originates on the visible part of the disk (see the arrow) at the interface between the AR and the CH. We make this affirmation after checking the previous images of EIT. There is no other active region where this streamer can originate. Any outward flow along this streamer would have a component towards Earth and thus cause the observed blue shift. The profiles along the streamer, at two different times are shown in Figure 6.34.
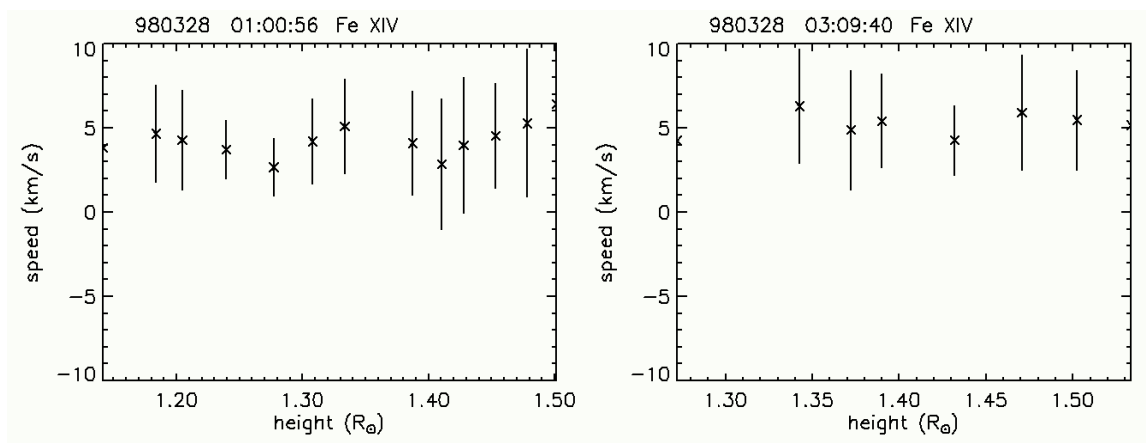
Figure 6.34 The speed profile along the streamer seen at south-west limb of the Sun, on 28th of March 1998 at 01:00 UT (left) and 03:09 UT (right).

We see that the speeds of the streamer along the LOS are positive, up to 7 km/s.

In order to get the radial velocity we determine the angle the streamer makes with the line of sight (see Figure 6.35).
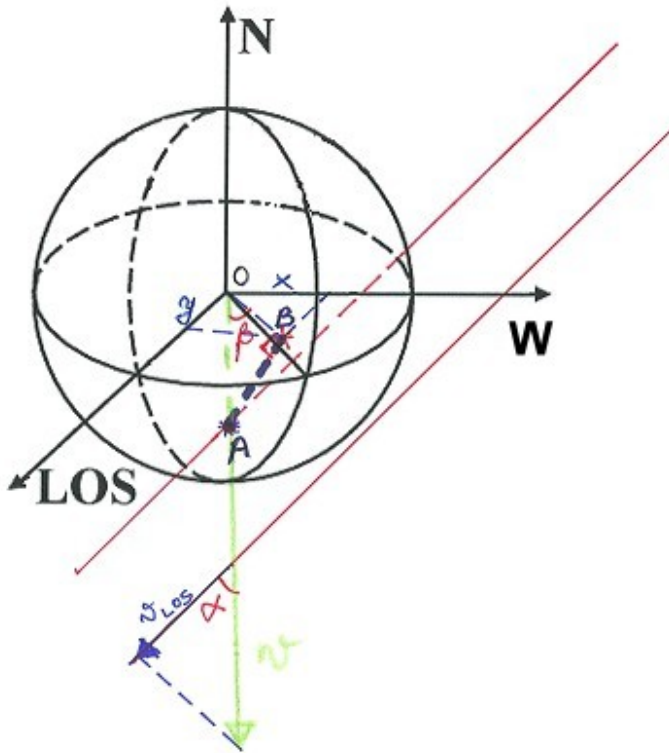
Figure 6.35 Schematic view of the radial speed (v) and the component on the line of sight (v_{LOS}).

The region we see on EIT images as the source of the radial flow is the point B in Figure 6.35. The corresponding point on the Sun surface is A. The line which passes through the center of the Sun (O) and point A give us the radial speed (v). LOS directions are represented by the black and red lines, perpendicular to the plane of the paper (NOW). The angle the radial speed makes it with the LOS is $\alpha = 90 - \beta$. The red line coincides with the AB line. In order to see them better we displaced them to a small angle.

In this particular case, for a LOS speed of 7 km/s and an angle α of 27º (as we see on EIT image) we obtain a radial speed of 7.9 km/s and a radial speed of 9.5 km/s for an angle of 43º.

These numbers are consistent with those reported by Chen et al. (2004). Frazin et al. (2003) measured speeds between 40 and 75 km/s at 4.6 $R_\odot$ and between 50 and 105 km/s at 5.1 $R_\odot$.

Speeds in the range 85 to 110 km/s were measured in UVCS data at a distance of 3.5 $R_\odot$ along a streamer on 20th, 21st of August 1996 (Abbo et al. 2003). For the data in 1996 and 1997, Abbo and Antonucci (2002) found wind velocities (for the regions surrounding the streamers) in the range 80 to 100 km/s for heights > 1.7 $R_\odot$. In streamers the outflow velocities of 50 - 90 km/s were found only above 2.3 $R_\odot$.

For the data in 1996 we saw in speed-time plots that due to the corona holes which are on both sides of the AR the plasma appears to flow along the interface of the CH and AR. We show two examples of combined EIT, C1 speed map and C2 images from the Fe XIV data in 1996.
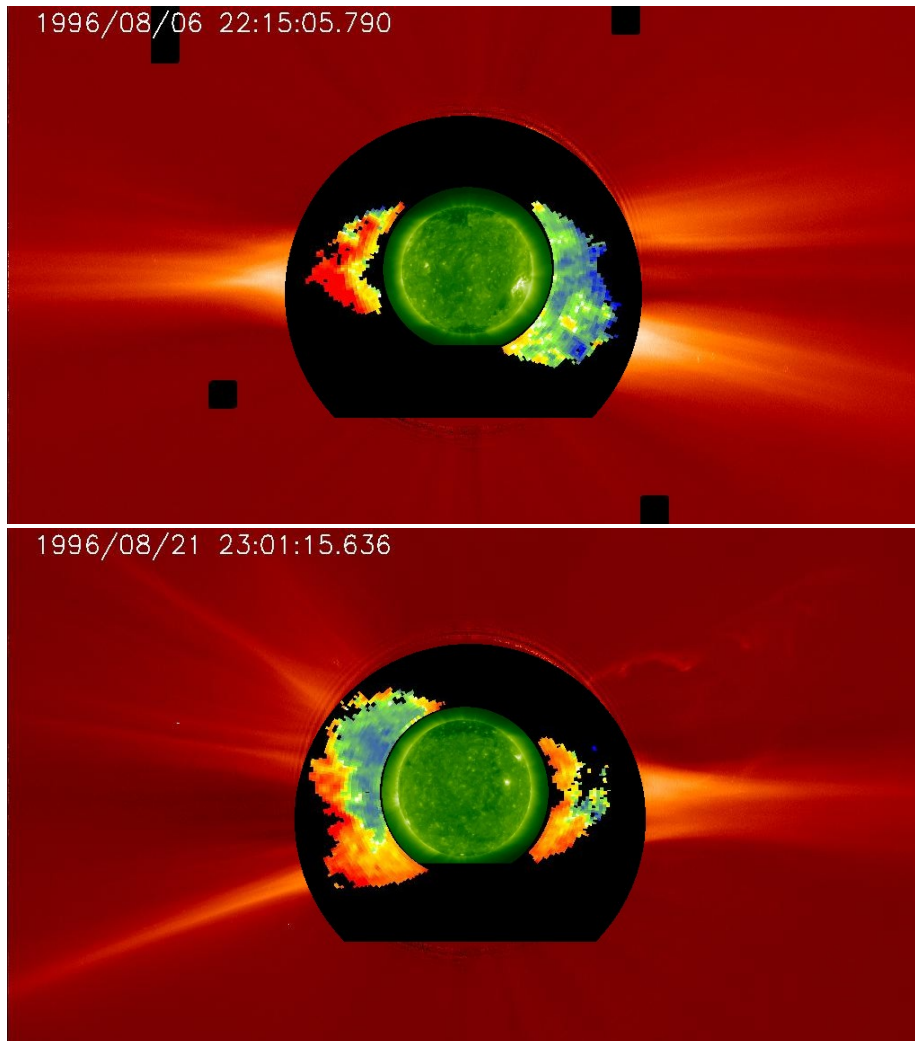
Figure 6.36 Combined EIT, C1 speed map and C2 images for data recorded on 6th of August 1996 (upper panel) and 21st of August 1996 (lower panel).

In the upper panel of the Figure 6.36 we see the AR at the edge of west limb. We think that the blue shift is due to the flow between the AR and the CH (on the right side of the AR - see Figure 6.27). In this case, at a LOS speed of 5km/s we get an angle α of 70º and a radial speed of 15 km/s. The same two regions are the regions from where flow is coming and is seen as blue shift in the lower panel of the Figure 6.36. For a LOS speed of 5 km/s at an angle α of 82º we get a radial speed of around 36 km/s.

The green corona in this period is seen in Figure 6.37. The images are processed with the wavelet technique in order to reveal the structures better.
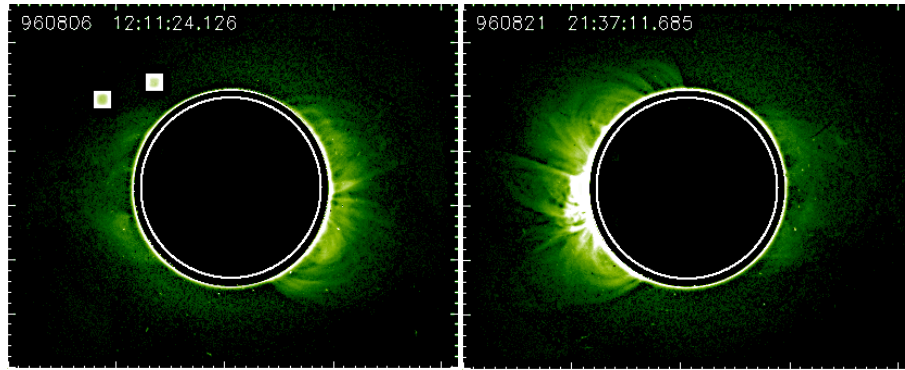
Figure 6.37 LASCO-C1 data recorded on 6th of August (left panel) and 21st of August 1996 (right panel). The images were processed using the wavelet technique.

Figure 6.37 shows a complex system of loops. However, we cannot yet decide whether there is flow emerging from the top of loops or from the interface with open magnetic field lines.

Discussions

As we mentioned in Chapter 1, the origin of slow solar wind (SSW) is not yet well known. There are several theories which try to explain the origin of the SSW.

From the observational point of view there are some explanations:

Sheeley et al. (1997) observed in LASCO-C2 data bright "blobs" moving out almost radially (see Figure 6.38). The authors call them "leaves in the wind", concluding that they are structures embedded in and flowing with the slow solar wind. An example of an elongated blob is shown in Figure 6.38.
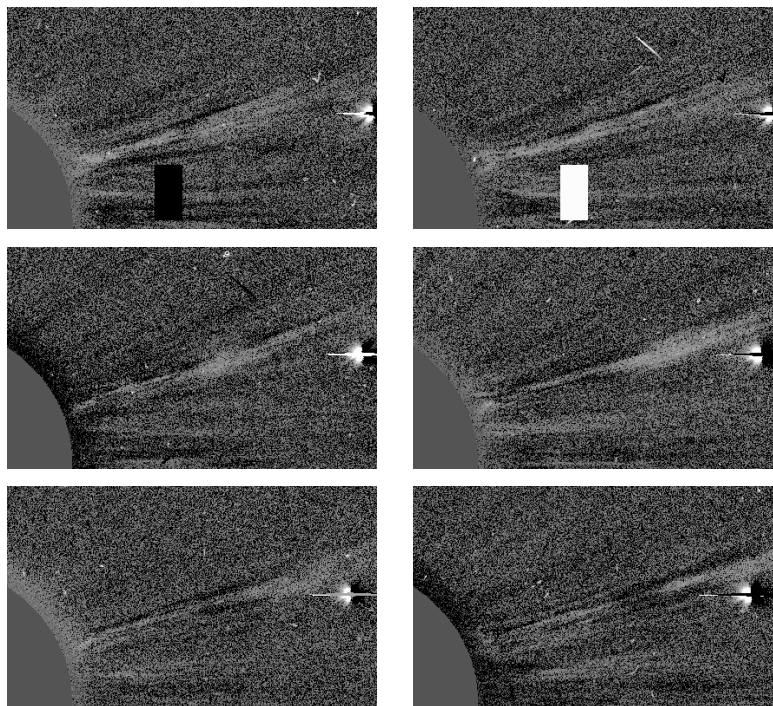
Figure 6.38 Running difference LASCO-C2 images, on 30th of October 1996, showing an elongated blob moving out at the NW side of the limb. The images were taken at 08:40, 09:25, 10:10, 11:10, 11:40, 1 2:35 UT, respectively. (from Sheeley et al. 1997).

The running difference images are built by subtracting the previous image in time from the following one. Any outward motions appears as a white part followed by a dark one in these images.

The formation of these blobs is explained by a global coronal magnetic field model based on resistive MHD theory, which implies that the field topology will be changed due to the magnetic reconnection process (shown in Figure 6.39, for illustration).
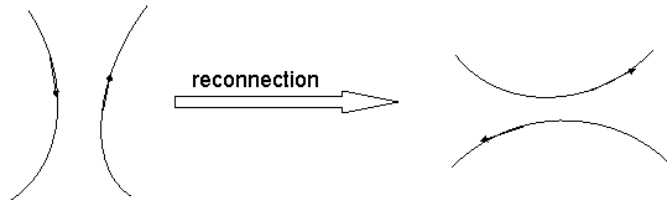
Figure 6.39 Schematic view of the magnetic reconnection process leading to a change of magnetic topology. The small arrows on the magnetic lines show the orientation of the magnetic field.

Generally the SSW is associated with streamers. Using UVCS data, Raymond et al. (1997), Noci et al. (1997) found that the flanks of the streamers are the source of the SSW (from Doppler dimming).

Woo and Martin (1997) from radio occultation measurements (using the data from Voyager 2), Bavassano et al. (1997) using data from Helios 2, Habbal et al. (1997) from radio occultation measurements combined with UVCS data and Strachan et al. (2002) using UVCS and LASCO data found that the SSW originates at streamer stalks (A_3 in Figure 6.40). Abbo et al. (2003) found also from observational evidence, that the SSW may have two types of sources:

1) the regions along the axis of streamer above $2.3 - 2.7$ $R_\odot$ (A_3 in Figure 6.40),

2) the regions along and adjacent to the streamer boundary (A_2 in Figure 6.40).
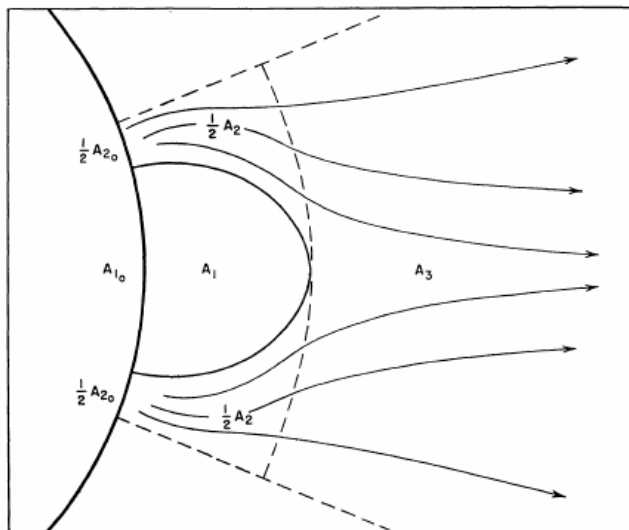
Figure 6.40 Schematic view of a cusp-like streamer (Pneuman 1968).

Several models were created in order to explain the source region of the SSW. The most realistic one appears to us to be the model of Fisk (1996). His model is based on two effects: the differential rotation of the photosphere and the super-radial expansion of the magnetic field underneath the source surface. The interplay of these two effects leads to latitudinal excursions of the magnetic field lines. The open magnetic field lines reconnect with equatorial closed magnetic field lines. The material stored in these loops escapes producing what we see as SSW.

Our analysis shows that the slow flow emerges in relation with an AR and a nearby CH, and we conclude that the release of the SSW can in fact be due to a reconnection process, in agreement with the model by Fisk (1996). However, we cannot decide from our observations whether the actual flow emerges from inside the streamer or from its outside boundaries.

On the other hand, our observation of the streamer in 1998 shows a split of the streamer right at that moment when we also observe a strong blue shift in our data. In this case, we would conclude that the flow emerges from the stalk of the streamer.

To summarize our conclusions:

We see slow solar wind originating:
   a)   at the level of streamer cusp? (Sheeley et al. 1997, Schmidt and Cargill 2000, Wiegelmann et al. 2000, Woo and Martin 1997, Bavassano et al. 1997, Habbal et al. 1997, Strachan et al. 2000, Eselevich and Eselevich 1999).
   b)   in the regions surrounding the streamer, close to the streamer boundary? (Wang 1994, Fisk et al. 1998, Ofman 2000).

Possible mechanisms:
   a)   magnetic reconnection process? (Fisk et al. 1998, Wu et al. 2000, Eselevich and Eselevich 1999, Suess and Nerney 1999).
   b)   reconnection in triple helmet streamers? (Wiegelmann et al. 2000).

6.4   Loop Observations Using Spectral Data

In the Fe XIV data in 1998 we had identified a big loop at the west limb of the Sun (see Figure 6.41). Here, we investigate it further, as it appeared on 28th of March, and on 29th of March when a CME occurred. The regions inside and outside the loop are investigated separately, and the results are shown in Figure 6.42.
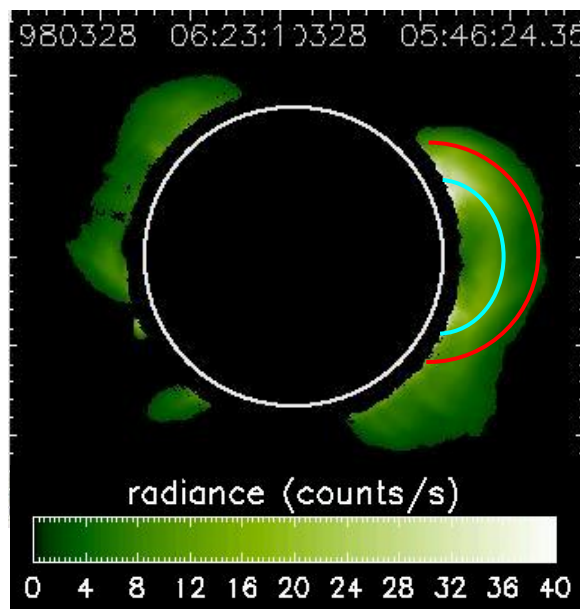
Figure 6.41 Radiance map recorded on 28th of March 1998. The blue curve shows the regions inside the loop and the red one the regions outside the loop.
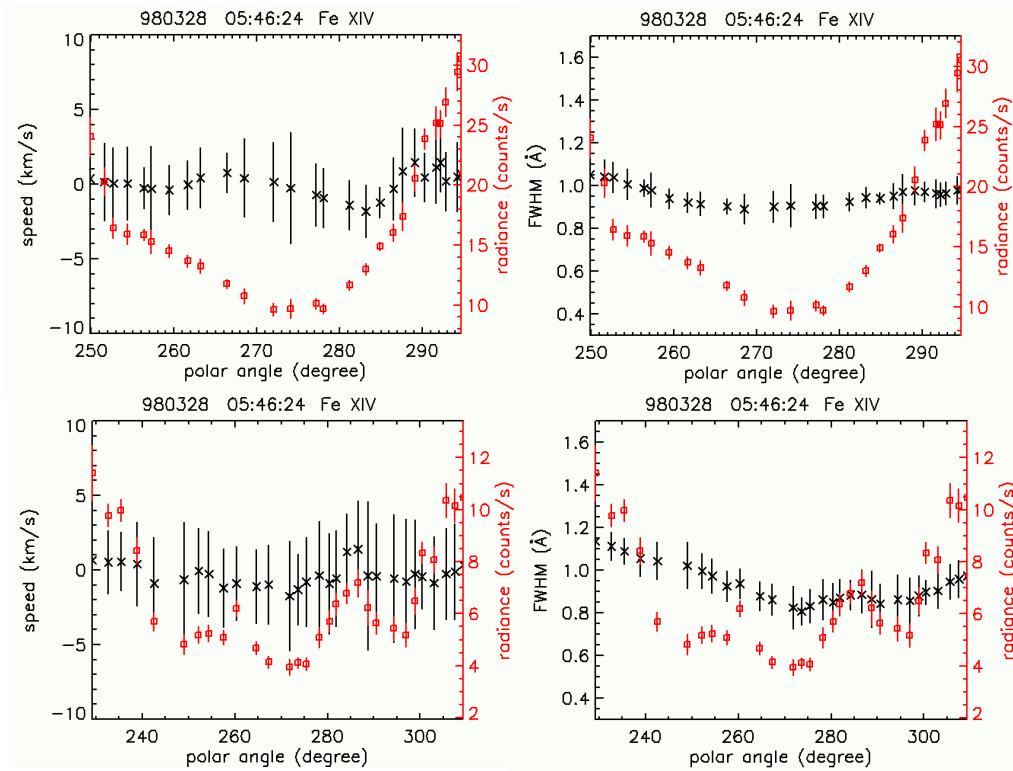
Figure 6.42 Polar cuts for a loop seen on the west side of the limb, on 28th of March (upper panels – blue loop of Figure 6.41) and for the outside regions (lower panels – red loop). The radiance is plotted in red color, speed (left) and FWHM (right) in black color.

The upper plots show the speed and radiance (upper left panel) and FWHM (upper right panel) along the loop. Similar plots are shown in the lower panels for the regions outside the loop (red curve in Figure 6.41). We see that the radiances inside the loop are much higher than outside. The speeds are generally around 0 km/s. The plasma inside the loop has the same temperature as outside (Figure 6.43).
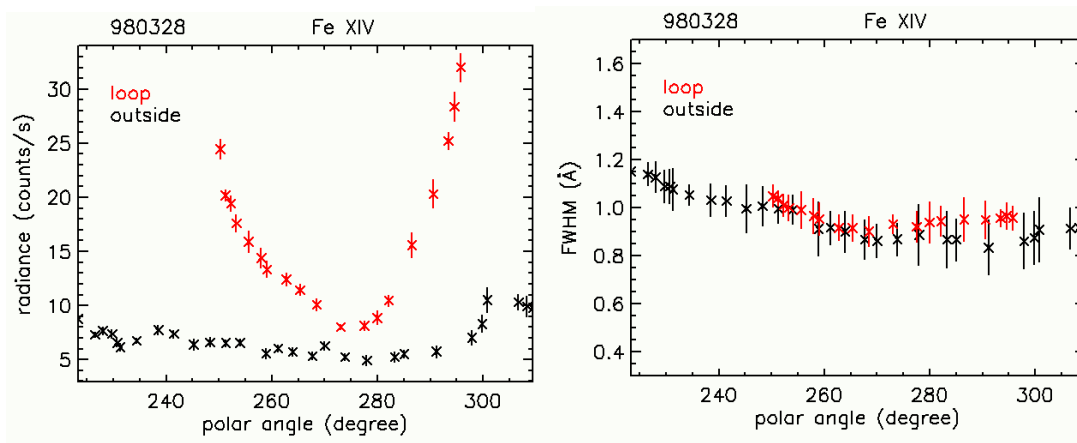
Figure 6.43 The radiance (left) and FWHM (right) cuts for the points inside (red) and outside the loop as shown by the semicircles in Figure 6.41.

Compared with the open structure at the south-west (strong blue shift in Figure 6.11) the plasma is cooler inside the loop (see Figure 6.44).
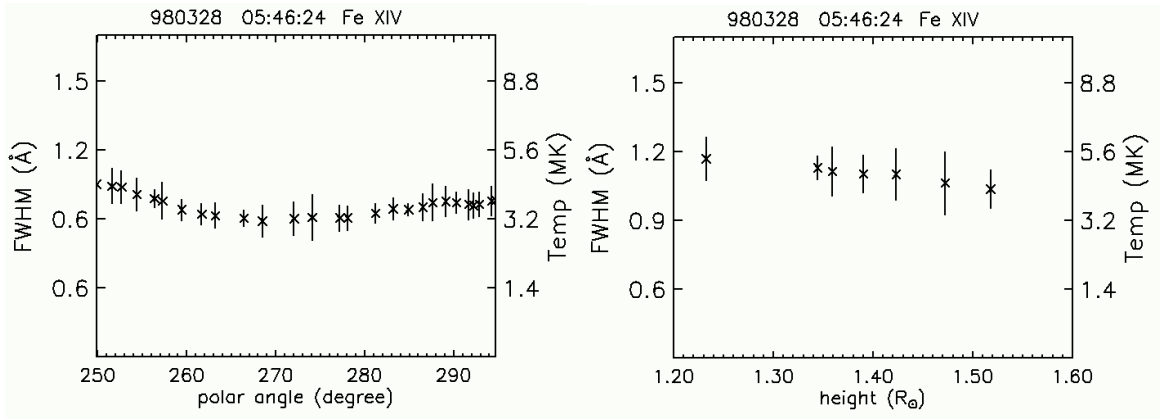
Figure 6.44 FWHM cuts for the loop (left) and for the streamer (right). The second axis shows the equivalent effective temperature scale.

Consistently with this result, Raju et al. (2000) found that the line widths in closed magnetic structures are smaller than those in open field structures. Singh et al. (2002) found that the width of the green line in both open and closed structures is almost the same, whereas the width of the red line is larger in the open structures as compared to the closed loop-like structures.

Similar trends as for data on 28th of March are found also for the loop on 29th of March (see Figure 6.45). The radiance is lower at the top of the loop, compared to its footpoints.
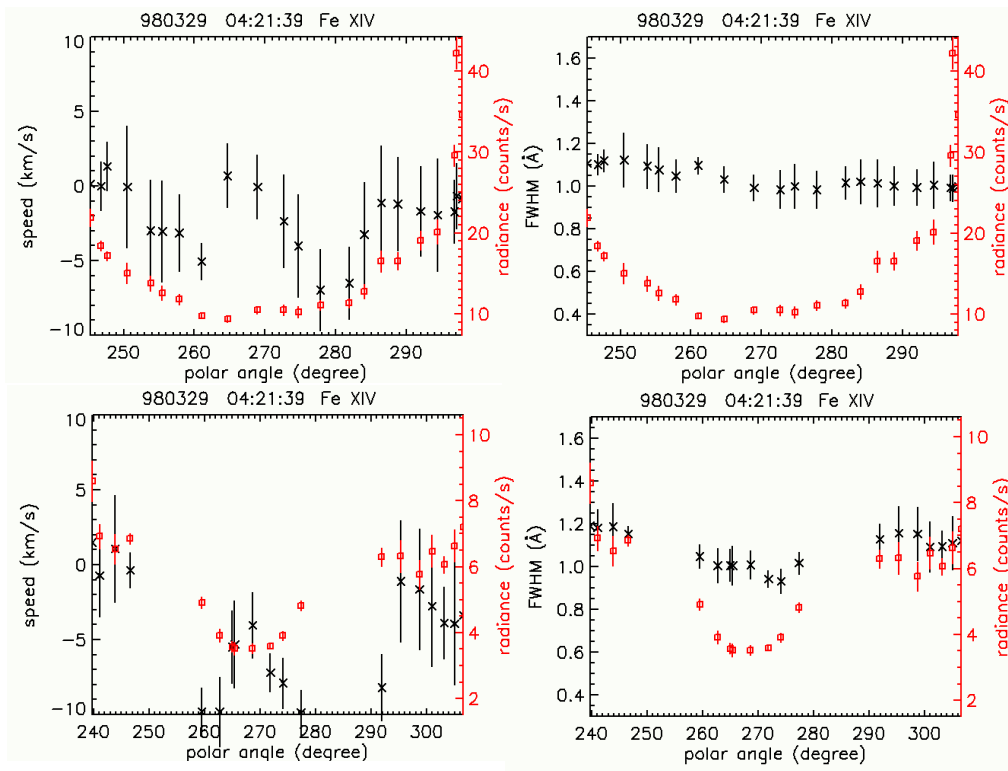
Figure 6.45 Polar cuts for a loop seen on west side of the limb, on 29th of March (left) and for the outside regions (right).

In this case we measure speeds up to -10 km/s which are due to a backside CME that happened to occur right at this time.

In general, the "temperatures" inside the loops are lower then outside, and the radiance at the top of the loop is less than at the legs of the loop.

6.5   Plumes Observations Using Spectral Data

Fe X data on 1996 show plumes mostly at the south pole. Unfortunately, the radiances are too small in these regions in order to get a reasonable fit. Because of this no conclusive results could be obtained. A better cadence or a higher exposure time is needed in order to analyze the plumes.

6.6   CME Observations Using Spectral Data

6.6.1 The CMEs on 28th of March 1998

Due to the high speeds of the CMEs and due to the limited spectral range of the instrument the CMEs are very difficult to detect. In the period of March 1998 we were lucky to catch at least the passage of three CMEs. They were identified in our spectral scans due to large blue or red shifts in speed maps. Their observation was confirmed by the EIT and C2 images.

On 28th of March 1998, 14:04 UT we observe in the speed maps a strong red shift on the west side of the Sun (see Figure 6.49). LASCO-C2 images show a CME rising around 14:00 (see the height time (HT) diagram (http://cdaw.gsfc.nasa.gov/CME_list/) in Figure 6.47). By checking the EIT images around this date we observe that the active region from where the CME probably originates is at the limb. If we extrapolate the height time diagram back we see that the CME passes a distance of 2 $R_\odot$ at around 14:00.
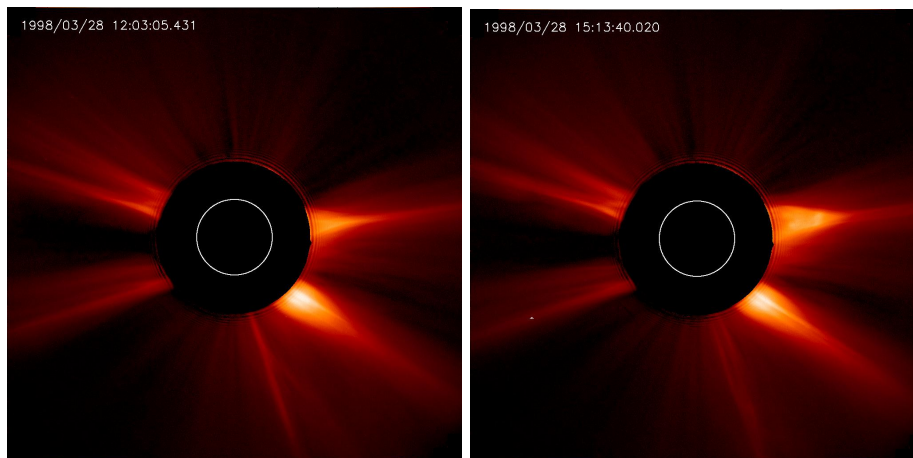
Figure 6.46 C2 image showing the CME (right) at WNW limb. The image on the left shows the white light corona before the occurrence of CME.

The HT diagram shows the behaviour of CME with time and height (see Figure 6.47).
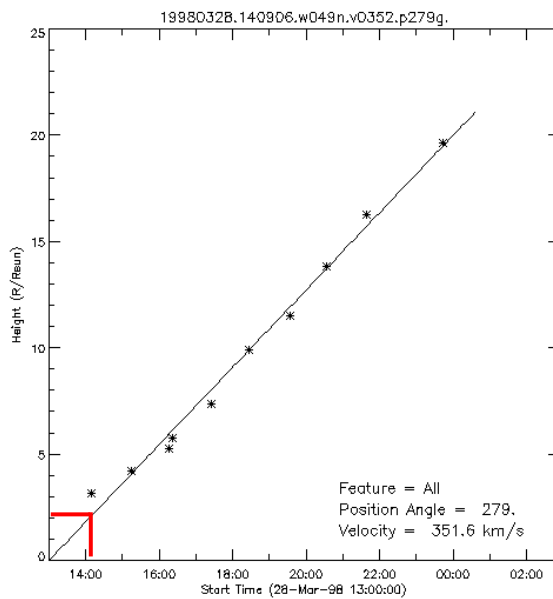
Figure 6.47 HT diagram of the CME from NRL CME catalogue, as seen in C2 and C3 field of views. The line shows the linear fit to the data points. It is extrapolated back in time in order to see the onset of CME in C1 field of view. The red lines show the time of the CME at a distance of 2 $R_\odot$.

If we look now at EIT images we see the bright region at the north west limb of the Sun. This is the place from where the CME starts.
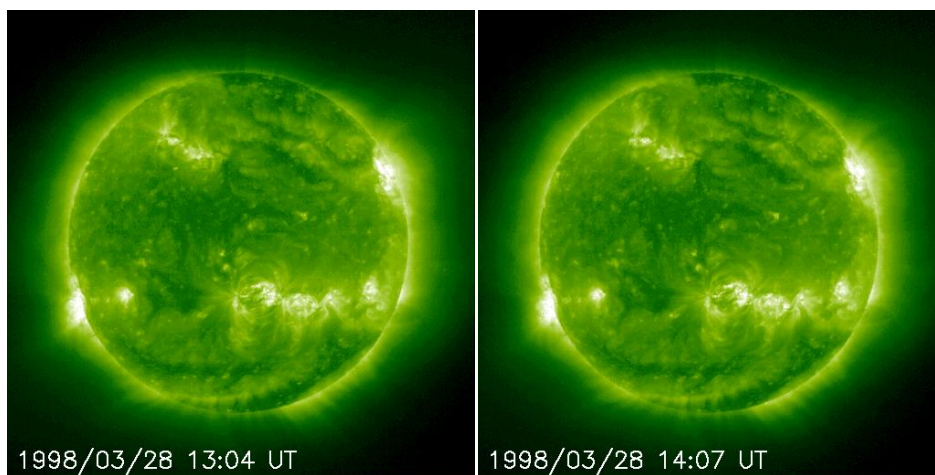
Figure 6.48 EIT images showing the active region on the north west limb of the Sun.

For this period of time we have spectral scans which show the CME in the field of view of C1 by strong red shifts seen in the speed maps. We show all the maps in order to characterize the CME on the speed, temperature and changes in coronal structures.
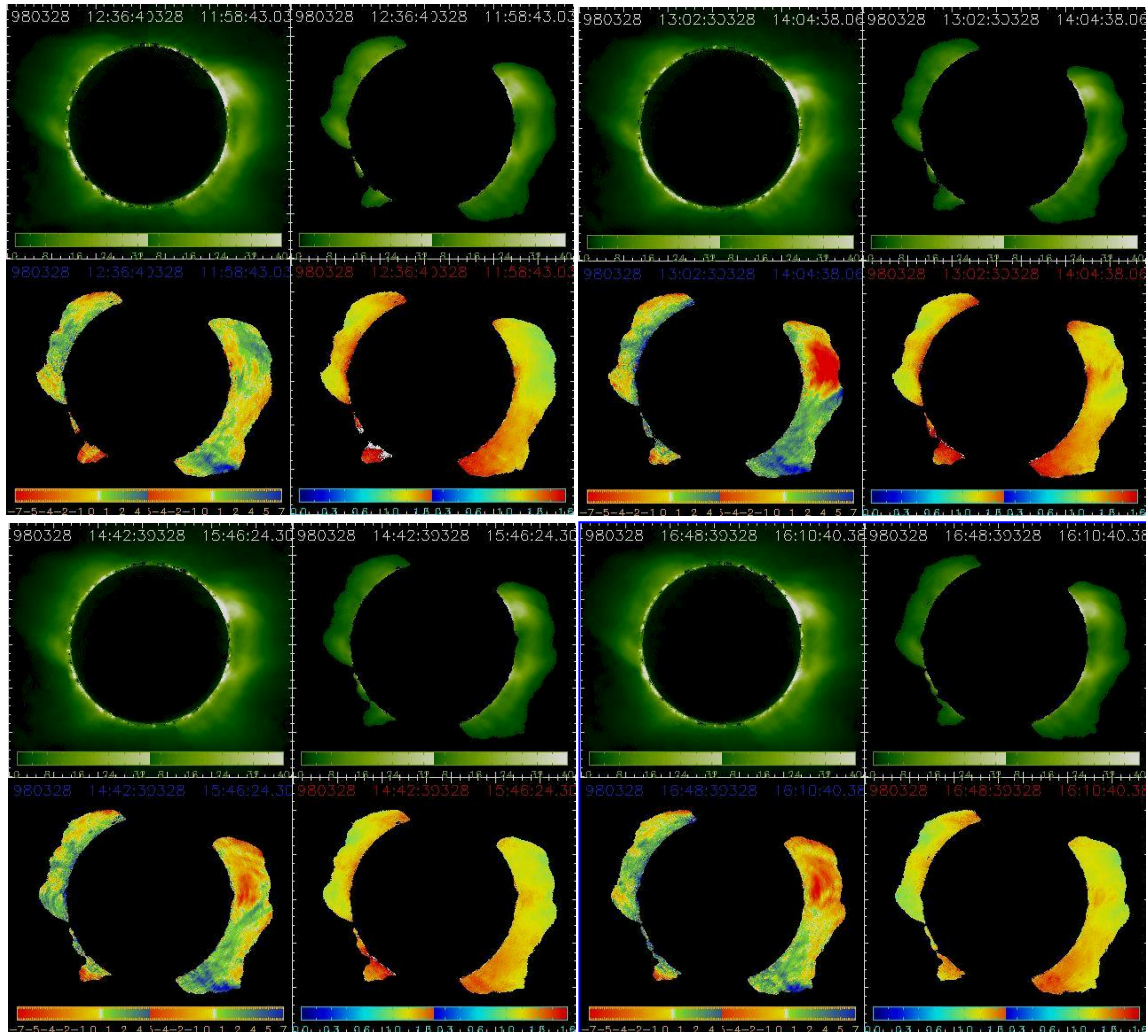
Figure 6.49 Four emission maps (both east and west images are combined in one image) taken on 28th of March 1998. Each panel has four images showing the routine data (upper left), the radiance map (upper right), the speed map (lower left), the FWHM map (lower right). The times the images are taken are: 11:58 UT (upper left panel), 14:04 (upper right panel), 15:46 (lower left panel) and 16:10 (lower right panel).

There are almost no changes in coronal structures visible (see the radiance maps: green color in Figure 6.49). However, the speed maps (lower left images of each data set) are changing from almost a blue shift (upper left panel) to a very strong red shift at around 14:00 (upper right panel). The red shift is there also on the other 2 panels until 16:48 UT. We can conclude that speed maps show significant flows although the top of CME had already left the C1 FOV about 2 hours earlier. Unfortunately, there was no spectral scan taken at the time when the CME itself went through the C1 filed of view. In the width maps we find an increase of the line width while the CME material was passing.

Later on, at around 22:41 another CME (a very faint halo CME) is passing the field of view of C2, (Figure 6.50). This CME cannot be identified in our C1 spectral data. Instead, an outflow starting at about the same time (see Figure 6.51) can be observed in speed maps as a red shift.
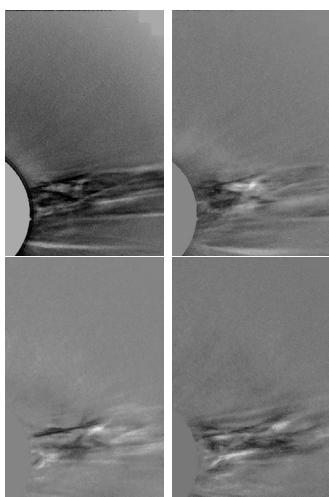
Figure 6.50 Running difference images showing the CME on the WNW limb of the Sun. The frames are recorded on 28th – 29th of March 1998 at 21:35 UT (upper left), 22:41 UT (upper right), 23:36 UT (lower left) and 00:39 UT (lower right).

The speed maps show a strong red shift in this period (see Figure 6.51).
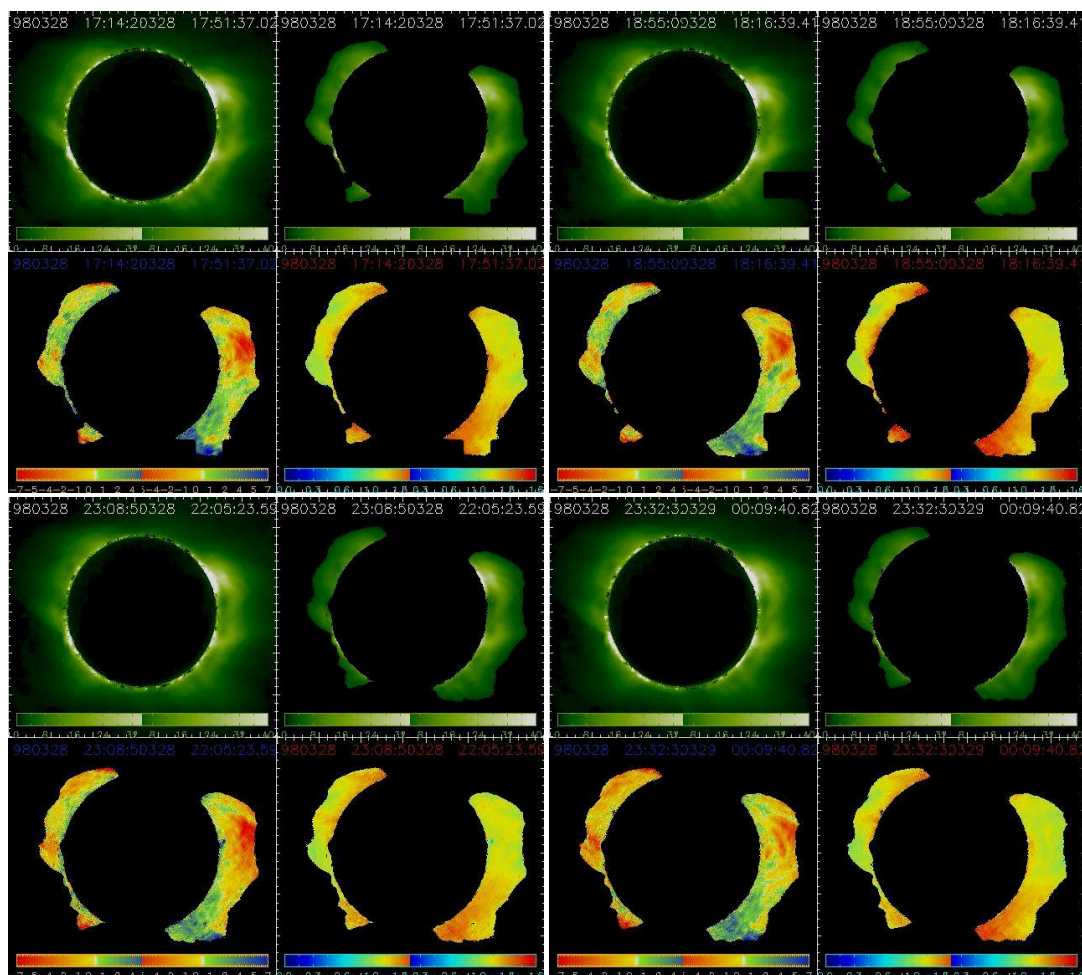
Figure 6.51 The same as in Figure 6.49. The data are recorded on 28th and 29th of March 1998 at times: 17:51 UT (upper left panel), 18:16 UT (upper right panel), 22:05 UT (lower left panel), 00:09 UT (lower right panel).

It is observed that in the upper right panel the outflow following the CME discussed above is still seen. Starting with 16:16 UT a new CME is observed (see the upper right panel). Its features are

still visible at around 00:09 UT on 29th of March 1998. Again, the green corona does not show any visible changes in the radiance maps.

6.6.2 The Halo CME on 29th of March 1998

On 29th of March we observe in the C2 data a halo CME beginning at 03:48 UT (see Figure 6.52).

Figure 6.52 LASCO-C2 images recorded on 29th of March 1998. Left side image is taken at 02:45 UT (before CME) and the right side image is taken at 03:48 UT (CME in progress).

If we look at the emission maps then we observe a strong red shift on 29th of March 1998, 04:21 UT. Again the green corona does not change significantly in the time of CME.

Figure 6.53 The same as in Figure 6.49. The data are recorded on 29th of March 1998 at times: 02:16 UT (upper left panel), 02:40 UT (upper right panel), 04:21 UT (lower left panel), 06:30 UT (lower right panel).

still visible at around 00:09 UT on 29th of March 1998. Again, the green corona does not show any visible changes in the radiance maps.

6.6.2 The Halo CME on 29th of March 1998

On 29th of March we observe in the C2 data a halo CME beginning at 03:48 UT (see Figure 6.52).

Figure 6.52 LASCO-C2 images recorded on 29th of March 1998. Left side image is taken at 02:45 UT (before CME) and the right side image is taken at 03:48 UT (CME in progress).

If we look at the emission maps then we observe a strong red shift on 29th of March 1998, 04:21 UT. Again the green corona does not change significantly in the time of CME.

Figure 6.53 The same as in Figure 6.49. The data are recorded on 29th of March 1998 at times: 02:16 UT (upper left panel), 02:40 UT (upper right panel), 04:21 UT (lower left panel), 06:30 UT (lower right panel).

Unfortunately, there were no spectral data taken at the time when the CME was in the field of view of C1 (around 3:00 as extrapolated from the HT diagram shown in Figure 6.54). Nevertheless, we can see plasma following the CME in the 2 lower panels of Figure 6.53 by the strong red shifts in the speed maps.
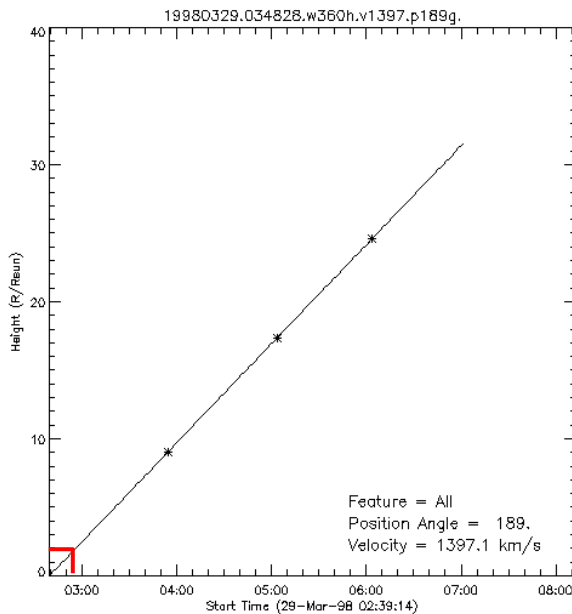
Figure 6.54 The HT diagram for the CME on 29th of March 1998. The data are fitted with a straight line.

From Figure 6.54 we note that the front speed of this CME was almost 1400 km/s, qualifying it as an extremely fast event, indeed. During the scanning time (15 minutes) of the C1 spectrum, the CME material must have moved considerably, which makes any interpretation of this spectrum highly questionable.

Summary and Conclusions

In this thesis, the dynamics of the green and red corona was studied using the spectral data from the LASCO-C1 instrument. To our knowledge, this is the first detailed study using LASCO-C1 spectral data.

The corona at activity minimum (1996) and during the ascending phase of the activity cycle (1998) was studied. In general, the corona in 1998 has higher radiances compared with corona in 1996. The radiances of Fe XIV increase by 75 % from 1996 to 1998, that of FeX by 80 %. We found flows along the line of sight in the range of -10 to 10 km/s. The streamers which were moving towards us could be detected by the blue shifts and away from us by the red shifts. By localizing the source region on the EIT images we could determine the radial flow speed, which in the case of the south-west streamer in 1998 was of around 9 km/s**.**

The line widths, if interpreted as "effective temperatures" were found to be much larger than the typical temperatures at which Fe X and Fe XIV ions form (1 MK for Fe X and 2 MK for Fe XIV). The excess is due to non-thermal motions in the plasma (like turbulences, wave motions, etc.).

In general, the corona in 1998 is "hotter" than the corona in 1996. For the data in 1998 we find that closed magnetic features are cooler than open magnetic features.

We observe that in general the Fe X line width is increasing with radial distance, while Fe XIV line width is decreasing. We put up a simple model demonstrating that line of sight effects can contribute to the line width decrease with height. Also, the variation of the radiance with height may be important in this context. However, the steep decrease we find at times in our data cannot yet be explained. Other effects have to be taken into account.

Due to the high speeds of CMEs, it is almost impossible to encounter one with the C1 instrument or even perform a spectral scan during its passage. It was mere luck that for 3 back side CMEs in 1998 we could measure large scale red shifts in the flow following these CMEs in the C1 speed maps. The corona structure as apparent in the C1 filed of view did not change much during these events. No significant trend in the line width maps was observed.

In speed maps we could also detect streamer material flowing away or towards the observer. As the slow solar wind is thought to come from regions associated with streamers, we studied these cases in detail. We found in the case of a particular streamer in 1998 that it originated in a region on the Sun where both closed (active regions) and open (coronal holes) magnetic fields were nearby. The streamer seen in C2 images changed its configuration at the same time when strong blue shifts were observed in C1 speed maps. Radial speeds of around 9 km/s at a distance of 1.3 $R_\odot$ were calculated.

For the investigated time period in 1996 there was on the disk only one active region flanked by two coronal holes. Our spectral analysis shows that there is outflow at the interface between the active region and the coronal holes. In the C2 images no change of this coronal streamer or any sign of outflow could be observed.

We conclude that the slow solar wind flow emerges near the interface between closed and open magnetic field regions. It is probably released by a magnetic reconnection process. In the case of the streamer in 1998 we found evidence for outflow from the cusp of the streamer.

References

Abbo, L., Antonucci, E., Mikic, Z., Riley, P., Dodero, M. A., Giordano, S., Acceleration region of the slow solar wind in corona., Memorie della Societa Astronomica Italiana, 74, 733, 2003

Abbo, Lucia; Antonucci, Ester, The streamer boundary and the source of the slow wind, In: Proceedings of the SOHO 11 Symposium on From Solar Min to Max: Half a Solar Cycle with SOHO, 11-15 March 2002, Davos, Switzerland. A symposium dedicated to Roger M. Bonnet. Edited by A. Wilson, ESA SP-508, Noordwijk: ESA Publications Division, ISBN 92-9092-818-2, 477, 2002

Antonucci, E., Kohl, J. L., Noci, G., Tondello, G., Huber, M. C. E., Gardner, L. D., Nicolosi, P., Giordano, S., Spadaro, D., Ciaravella, A., Raymond, C. J., Naletto, G., Fineschi, S., Romoli, M., Siegmund, O. H. W., Benna, C., Michels, J., Modigliani, A., Panasyuk, A., Pernechele, C., Smith, P. L., Strachan, L., Ventura, R., Velocity Fields in the Solar Corona during Mass Ejections as Observed with UVCS-SOHO, Astrophysical Journal Letters, 490, L183, 1997

Aschwanden, M. J., Nightingale, R. W., Alexander, D., Evidence for Nonuniform Heating of Coronal Loops Inferred from Multithread Modeling of TRACE Data, The Astrophysical Journal, 541, 1059, 2000

Banerjee, D., Teriaca, L., Doyle, J. G., Wilhelm, K., Broadening of SI VIII lines observed in the solar polar coronal holes, Astronomy and Astrophysics, v.339, p.208-214 (1998)

Baum, W. A., Johnson, F. S., Oberly, J. J., Rockwood, C. C., Strain, C. V. et al., Solar Ultraviolet Spectrum to 88 kilometers., Phys. Rev., 70, 781, 1946

Bavassano, B., Woo, R., Bruno, R., Heliospheric plasma sheet and coronal streamers., Geophysical Research Letters, 24, 1655, 1997

Boland, B.C., Engstrom, S. F. T., Jones, B. B., Wilson, R., The Heating of the Solar Corona. I. Observa- tion of Ion Energies in the Transition Zone, Astronomy and Astrophysics, 22, 161 1973

Boland, B. C., Dyer, E. P., Firth, J. G., Gabriel, A. H., Jones, B. B., Jordan, C., McWhirter, R. W. P., Monk, P., Turner, R. F., Further measurements of emission line profiles in the solar ultraviolet spectrum, Royal Astronomical Society, Monthly Notices, 171, 697, 1975

Brage, Tomas, Judge, P. G., Brekke, P., Intercombinations and Allowed Transitions in O IV, Astrophysical Journal, 464, 1030, 1996

Brekke, P., Thompson, W. T., Woods, T. N., Eparvier, F. G., The Extreme-Ultraviolet Solar Irradiance Spectrum Observed with the Coronal Diagnostic Spectrometer (CDS) on SOHO., The Astrophysical Journal, 536, 959, 2000

Broussard, R. M., Tousey, R., Underwood, J. H., Sheeley, N. R., Jr., A survey of coronal holes and their solar wind associations throughout sunspot cycle 20., Solar Physics, 56, 161, 1978

Brueckner, G. E., Ultraviolet emission line profiles of flares and active regions, In: Solar gamma-, X-, and EUV radiation, Proceedings of the Symposium, Buenos Aires, Argentina, June 11-14, 1974. (A76-10126 01-92) Dordrecht, D. Reidel Publishing Co., 1975, p. 135-151

Brueckner, G. E., Howard, R. A., Koomen, M. J., Korendyke, C. M., Michels, D. J., Moses, J. D., Socker, D. G., Dere, K. P., Lamy, P. L., Llebaria, A., Bout, M. V., Schwenn, R., Simnett, G. M., Bedford, D. K., Eyles, C. J., The Large Angle Spectroscopic Coronagraph (LASCO)., Solar Physics, 162, 357, 1995

Chae, J., Schühle, U., Lemaire, P., SUMER Measurements of Nonthermal Motions: Constraints on Coronal Heating Mechanisms, The Astrophysical Journal, 505, 957, 1998

Charvin, P., Étude de la polarisation des raies interdites de la couronne solaire. Application au cas de la raie verte lambda 5303., Annales d'Astrophysique, 28, 877, 1965

Charvin, P., Experimental Study of the Orientation of Magnetic Fields in the Corona., Solar Magnetic Fields. Symposium no. 43, held at the College de France Paris, France, August 31 to September 4, 1970. Edited by Robert Howard. International Astronomical Union. Symposium no. 43, Dordrecht, Reidel, p.580, 1971

Chen, Y., Esser, R., Strachan, L., Hu, Y., Stagnated Outflow of O^{+5} Ions in the Source Region of the Slow Solar Wind at Solar Minimum, The Astrophysical Journal, 602, 415, 2004

Cook, J. W., Socker, D. G., Korendyke, C. M., Howard, R. A., Brueckner, G. E., Karovska, M., Wood, B. E., Search for Velocity Variations in Fe XIV 5304 A. Coronagraph Observations Near Activity Minimum., Advances in Space Research, 25, 1883, 2000

Curdt, W., Brekke, P., Feldman, U., Wilhelm, K., Dwivedi, B. N., Schühle, U., Lemaire, P., The SUMER spectral atlas of solar-disk features., Astronomy and Astrophysics, 375, 591, 2001

Dahlburg, R. B., Karpen, J. T., Einaudi, G., Bonicelli, P., Acceleration of the slow solar wind., Solar Jets and Coronal Plumes, Proceedings of an International meeting, Guadeloupe, France, 23-26 February 1998, Publisher: Paris: European Space Agency (ESA), 1998, ESA SP-421, p.199

de Boer, K. S., Olthof, H., Pottasch, S. R., Abundances in the Solar Corona, Astronomy and Astrophysics, 16, 417, 1972

Dere, K. P., Mason, H. E., Nonthermal velocities in the solar transition zone observed with the high-resolution telescope and spectrograph, Solar Physics, 144, 217, 1993

Del Zanna, G., Bromage, B. J. I., The Elephant's Trunk: Spectroscopic diagnostics applied to SOHO/CDS observations of the August 1996 equatorial coronal hole, Journal of Geophysical Research, 104, 9753, 1999

Domingo, V., Fleck, B., Poland, A. I., The SOHO Mission: an Overview, Solar Physics, 162, 1, 1995

Doschek, G. A., Warren, H. P., Laming, J. M., Mariska, J. T., Wilhelm, K., Lemaire, P., Schuehle, U., Moran, T. G., Electron Densities in the Solar Polar Coronal Holes from Density Sensitive Line Ratios of Si8 and Si10, Astrophysical Journal Letters, 482, L109, 1999

Doschek, G. A., Vanhoosier, M. E., Bartoe, J.-D. F., Feldman, U., The emission-line spectrum above the limb of the quiet sun - 1175-1940 A, Astrophysical Journal Supplement Series, 31, 417, 1976

Doschek, G. A., Feldman, U., The coronal temperature and nonthermal motions in a coronal hole compared with other solar regions, Astrophysical Journal, Part 2 - Letters to the Editor, 212, L143, 1977

Edlén, B., Mg I-ähnliche Spektren der Elemente Titan bis Cobalt, Ti XI, V XII, Cr XIII, Mn XIV, Fe XV und Co XVI, Z. Phys., 103, 536, 1936

Edlén, B., S I-ähnliche Spektren der Elemente Titan bis Eisen, Ti VII, V VIII, Cr IX, Mn X, und Fe XI, Z. Phys., 104, 188, 1937

Edlén, B., Swings, P., Term Analysis of the Third Spectrum of Iron (Fe III)., Astrophysical Journal, 95, 532, 1942

Eselevich, V. G., Eselevich, M. V., An investigation of the fine ray structure of the coronal streamer belt using LASCO data, Solar Physics, 188, 299, 1999

Esser, R., Brickhouse, N. S., Habbal, S. R., Altrock, R. C., Hudson, H. S., Using Fe X 6374 Å and Fe XIV 5303 Å spectral line intensities to study the effect of line of sight integration on coronal temperature inferences., Journal of Geophysical Research, 100, 19829, 1995

Feldman, U., Laming, J. M., Mandelbaum, P., Goldstein, W. H., Osterheld, A., A burst model for line emission in the solar atmosphere. II - Coronal extreme ultraviolet lines., Astrophysical Journal, 398, 692, 1992

Fisher, R., Musman, S., Detection of coronal holes from 5303-A-wavelength Fe XIV observations., Astrophysical Journal, 195, 801, 1975

Fisher, R. R., Lambda 5303 Fe XIV density models of the inner solar corona., Solar Physics, 57, 119, 1978

Fisk, L. A., Motion of the footpoints of heliospheric magnetic field lines at the Sun: Implications for recurrent energetic particle events at high heliographic latitudes., Journal of Geophysical Research, 101, 15547, 1996

Fisk, L. A., Schwadron, N. A., Zurbuchen, T. H., On the Slow Solar Wind, Space Science Reviews, 86, 51, 1998

Frazin, R. A., Cranmer, S. R., Kohl, J. L., Empirically Determined Anisotropic Velocity Distributions and Outflows of O^{5+} Ions in a Coronal Streamer at Solar Minimum, The Astrophysical Journal, 597, 1145, 2003

Gibson, S. E., Fludra, A., Bagenal, F., Biesecker, D., Zanna, G. Del, Bromage, B., Solar minimum streamer densities and temperatures using Whole Sun Month coordinated data sets, Journal of Geophysical Research, 104, 9691, 1999

Golub, L., Nystrom, G., Herant, M., Kalata, K., Lovas, I., Sub-arcsecond observations of the solar X-ray corona., Nature, 344, 842, 1990

Gray, D. F., The observation and analysis of stellar photospheres, Cambridge University Press, 1992

Gringauz, K. I., Kurt, V. G., Moroz, V. I., Shklovskii, I. S., Results of Observations of Charged Particles Observed Out to R = 100, 000 km, with the Aid of Charged-Particle Traps on Soviet Space Rockets., Astronomicheskii Zhurnal, 37, 716, 1960

Grotrian, W., Zur Frage der Deutung der Linien im Spektrum der Sonnenkorona, Die Naturwissenschaften, 27, 214, 1939

Guhathakurta M., Fisher, R. R., Altrock, R. C., Large-scale coronal temperature and density distributions, 1984-1992., Astrophysical Journal, 414, L145, 1993

Habbal, S. R., Woo, R., Fineschi, S., O'Neal, R., Kohl, J., Noci, G., Korendyke, C., Origins of the Slow and the Ubiquitous Fast Solar Wind., Astrophysical Journal Letters, 489, L103, 1997

Hara, H., Ichimoto, K., Microscopic Nonthermal Plasma Motions of Coronal Loops in a Solar Active Region., The Astrophysical Journal, 513, 969, 1999

Harrison, R. A., Hood, A. W., Pike, C. D., Off-limb EUV line profiles and the search for wave activity in the low corona, Astronomy and Astrophysics, 392, 319, 2002

Hassler, D. M., Rottman, G. J., Shoub, E. C., Holzer, T. E., Line broadening of MG X 609 and 625 A coronal emission lines observed above the solar limb, Astrophysical Journal, Part 2 - Letters, 348, L77, 1990

Ichimoto, K., Ohtani, H., Ishigaki, T., Maemura, H., Noguchi, M., An imaging observation of the solar corona in the green line with a Fabry-Perot interferometer on a coronagraph, PASJ: Publications of the Astronomical Society of Japan, 47, 383, 1995

Jones, H. P., Recent studies of magnetic canopies., (R. G. Giovanelli Commemorative Colloquium, Tucson, AZ, Jan. 17, 18, 1985), Australian Journal of Physics, 38, 919, 1985

Kneer, F., Stolpe, F., High Resolution Observations of Small-Scale Magnetic Elements and Interpretation, Solar Physics, 164, 303, 1996

Kneer, F., Hasan, S. S., Kalkofen, W., Spectral line radiation from solar small-scale magnetic flux tubes., Astronomy and Astrophysics, 305, 660, 1996

Kohl, J. H., Gardner, L. D., Fineschi, S., Raymond, J. C., Noci, G., Romoli, M., Antonucci, E., Tondello, G., Nicolosi, P., Huber, M. C. E., Measurements of H I and O VI velocity distributions in the extended solar corona with UVCS/SOHO and UVCS/Spartan 201., Advances in Space Research, 20, 3,1997

Kohl, J. L., Noci, G., Antonucci, E., Tondello, G., Huber, M. C. E., Gardner, L. D., Nicolosi, P., Strachan, L., Fineschi, S., Raymond, J. C., Romoli, M., Spadaro, D., Panasyuk, A., Siegmund, O. H. W., Benna, C., Ciaravella, A., Cranmer, S. R., Giordano, S., Karovska, M., Martin, R., Michels, J., Modigliani, A., Naletto, G., Pernechele, C., Poletto, G., Smith, P. L., First Results from the SOHO Ultraviolet Coronagraph Spectrometer., Solar Physics, 175, 613, 1997

Kohl, J. L., Noci, G., Antonucci, E., Tondello, G., Huber, M. C. E., Cranmer, S. R., Strachan, L., Panasyuk, A. V., Gardner, L. D., Romoli, M., Fineschi, S., Dobrzycka, D., Raymond, J. C., Nicolosi, P., Siegmund, O. H. W., Spadaro, D., Benna, C., Ciaravella, A., Giordano, S., Habbal, S. R., Karovska, M., Li, X., Martin, R., Michels, J. G., Modigliani, A., Naletto, G., O'Neal, R. H., Pernechele, C., Poletto, G., Smith, P. L., Suleiman, R. M., UVCS/SOHO Empirical Determinations of Anisotropic Velocity Distributions in the Solar Corona., Astrophysical Journal Letters, 501, L127, 1998

Koutchmy, S., Livshits, M., Coronal Streamers., Space Science Reviews, 61, 393, 1992

Krieger, A. S., Timothy, A. F., Roelof, E. C., A Coronal Hole and Its Identification as the Source of a High Velocity Solar Wind Stream., Solar Physics, 29, 505, 1973

Lyot, B., Compt. Rend. Acad. Sci., 193, 1169, 1931

Mariska, J. T., The solar transition region., Cambridge University Press, 1992

Mason, H. E., Fossi, B. C. Monsignori, Spectroscopic diagnostics in the VUV for solar and stellar plasmas., Astronomy and Astrophysics Review, 6, 123, 1994

Neugebauer, M., Snyder, C. W., Mariner-2 Measurements of the Solar Wind., The Solar Wind, Proceedings of a conference held 1-4 April, 1964 at the California Institute of Technology. Edited by Robert J. Mackin, Jr. and Marcia Neugebauer. Oxford: Permanon Press, 1966, p.3

Noci, G., Energy Budget in Coronal Holes., Solar Physics, 28, 403, 1973

Noci, G., Kohl, J. L., Antonucci, E., Tondello, G., Huber, M. C. E., Fineschi, S., Gardner, L. D., Korendyke, C. M., Nicolosi, P., Romoli, M., Spadaro, D., Maccari, L., Raymond, J. C., Siegmund, O. H. W., Benna, C., Ciaravella, A., Giordano, S., Michels, J., Modigliani, A., Naletto, G., Panasyuk, A., Pernechele, C., Poletto, G., Smith, P. L., Strachan, L., The quiescent corona and slow solar wind, Fifth SOHO Workshop: The Corona and Solar Wind Near Minimum Activity. held at Institute of Theoretical Astrophysics. University of Oslo, Norway, 17-20 June, 1997. Edited by A. Wilson, European Space Agency, 1997, p.75

Ofman, L., Source regions of the slow solar wind in coronal streamers., Geophysical Research Letters, 27, 2885, 2000

O'Shea, E., Banerjee, D., Poedts, S., Variation of coronal line widths on and off the disk, Astronomy and Astrophysics, 400, 1065, 2003

Parker, E. N., Dynamics of the Interplanetary Gas and Magnetic Fields., Astrophysical Journal, 128, 664, 1958

Pneuman, G. W., Some General Properties of Helmeted Coronal Structures., Solar Physics, 3, 578, 1968

Press, W. H., Flannery, B. P., Teukolsky, S. E., Vetterling, W. T., Numerical Recipes in Fortran, Cambridge University Press, 1992

Raju, K. P., Desai, J. N., Chandrasekhar, T., Ashok, N. M., The excitation mechanism of Fe XIV 5303 A forbidden line in the inner regions of solar corona., Journal of Astrophysics and Astronomy, 12, 311, 1991.

Raju, K. P., Sakurai, T., Ichimoto, K., Singh, J., The Physical Conditions in a Polar Coronal Hole and Nearby Regions from Norikura and SOHO Observations., The Astrophysical Journal, 543, 1044, 2000

Raymond, J. C., Kohl, J. L., Noci, G., Antonucci, E., Tondello, G., Huber, M. C. E., Gardner, L. D., Nicolosi, P., Fineschi, S., Romoli, M., Spadaro, D., Siegmund, O. H. W., Benna, C., Ciaravella, A., Cranmer, S., Giordano, S., Karovska, M., Martin, R., Michels, J., Modigliani, A., Naletto, G., Panasyuk, A., Pernechele, C., Poletto, G., Smith, P. L.,

Suleiman, R. M., Strachan, L., Composition of Coronal Streamers from the SOHO Ultraviolet Coronagraph Spectrometer, Solar Physics, 175, 645, 1997

Sahal-Brechot, S., Role of collisions in the polarization degree of the forbidden emission lines of the Solar Corona. II - Depolarization by electron impact and calculation of the polarization degree of the Green line of Fe XIV., Astronomy and Astrophysics, 36, 355, 1974

Sahal-Brechot, S., Role of Collisions in the Polarization Rate of the Forbidden Emission Lines of the Solar Corona. I. Depolarization by Proton Impact. Application to the Green Line of Fe XIV and to the Infrared Lines of Fe XIII., Astronomy and Astrophysics, 32, 147, 1974

Schmidt, J. M., Cargill, P. J., A model for accelerated density enhancements emerging from coronal streamers in Large-Angle and Spectrometric Coronagraph observations, Journal of Geophysical Research, 105, 10455, 2000

Schrijver, C. J., Title, A. M., Berger, T. E., Fletcher, L., Hurlburt, N. E., Nightingale, R. W., Shine, R. A., Tarbell, T. D., Wolfson, J., Golub, L., Bookbinder, J. A., Deluca, E. E., McMullen, R. A., Warren, H. P., Kankelborg, C. C., Handy, B. N., de Pontieu, B., A new view of the solar outer atmosphere by the Transition Region and Coronal Explorer, Solar Physics, 187, 261, 1999

Schwenn, R., Inhester, B., Plunkett, S. P., Epple, A., Podlipnik, B., Bedford, D. K., Eyles, C. J., Simnett, G. M., Tappin, S. J., Bout, M. V., Lamy, P. L., Llebaria, A., Brueckner, G. E., Dere, K. P., Howard, R. A., Koomen, M. J., Korendyke, C. M., Michels, D. J., Moses, J. D., Moulton, N. E., Paswaters, S. E., Socker, D. G., Cyr, O. C. St., Wang, D., First View of the Extended Green-Line Emission Corona At Solar Activity Minimum Using the Lasco-C1 Coronagraph on SOHO., Solar Physics, 175, 667, 1997

Schwenn, R., Marsch, E., (Eds.), Physics of the Inner Heliosphere, Springer-Verlag Berlin Heidelberg, 1991

Sheeley, N. R., Jr., Wang, Y.-M., Hawley, S. H., Brueckner, G. E., Dere, K. P., Howard, R. A., Koomen, M. J., Korendyke, C. M., Michels, D. J., Paswaters, S. E., Socker, D. G., St. Cyr, O. C., Wang, D., Lamy, P. L., Llebaria, A., Schwenn, R., Simnett, G. M., Plunkett, S., Biesecker, D. A., Measurements of Flow Speeds in the Corona between 2 and 30 R sub sun, Astrophysical Journal, 484, 472, 1997

Singh, J., Clues to the mode of excitation of Fe X ions in the solar corona from the 1980 eclipse observations., Solar Physics, 95, 253, 1985

Singh, J., Ichimoto, K., Imai, H., Sakurai, T., Takeda, A., Spectroscopic Studies of the Solar Corona I. Spatial Variations in Line Parameters of Green and Red Coronal Lines., Publ. of the Astronomical Society of Japan, 51, 269, 1999

Singh, J., Sakurai, T., Ichimoto, K., Takeda, A., Spectroscopic Studies of the Solar Corona III. Density Diagnostics Using the Infrared Lines of Fe XIII., Publications of the Astronomical Society of Japan, 54, 807, 2002

Snyder, C. W., Neugebauer, M., Rao, U. R., The Solar Wind Velocity and Its Correlation with Cosmic-Ray Variations and with Solar and Geomagnetic Activity., Journal of Geophysical Research, 68, 6361, 1963

Solanki, S. K., Steiner, O., How magnetic is the solar chromosphere?., Astronomy and Astrophysics, 234, 519, 1990

Stenborg, G., Schwenn, R., Inhester, B., Srivastava, N., On the Rotation Rate of the Emission Solar Corona, Magnetic Fields and Solar Processes. The 9th European Meeting on Solar Physics, held 12-18 September, 1999, in Florence, Italy, p.1107, 1999

Stenborg, G., Cobelli, P. J., A wavelet packets equalization technique to reveal the multiple spatial-scale nature of coronal structures., Astronomy and Astrophysics, 398, 1185, 2003

Stix, M., The Sun - An introduction, Springer-Verlag Berlin Heidelberg New York, 2002

Strachan, L., Suleiman, R., Panasyuk, A. V., Biesecker, D. A., Kohl, J. L., Empirical Densities, Kinetic Temperatures, and Outflow Velocities in the Equatorial Streamer Belt at Solar Minimum., The Astrophysical Journal, 571, 1008, 2002

Suess, S. T., Nerney, S., MHD Streamer Structure, Slow Solar Wind, and the Streamer Brightness Boundary., Magnetic Fields and Solar Processes The 9th European Meeting on Solar Physics, held 12-18 September, 1999, in Florence, Italy. Edited by A. Wilson. European Space Agency, ESA SP-448, 1999., p.1101

Teriaca, L., Banerjee, D., Doyle, J. G., SUMER observations of Doppler shift in the quiet Sun and in an active region, Astronomy and Astrophysics, 349, 636, 1999

Teriaca, L., Structure and dynamics of the solar outer atmosphere as inferred from EUV observations, PhD Thesis, The Queen´s University of Belfast, 2001

Waldmeier, M., Die Sonnenkorona (II)., Birkhäuser Verlag Basel und Stuttgart, 1957

Waldmeier, M., The Asymmetry of Solar Activity in the Years 1959-1969., Solar Physics, 20, 332, 1971

Waldmeier, M., The coronal hole at the 7 March 1970 solar eclipse., Solar Physics, 40, 351, 1975

Wang, Y.-M., Sheeley, N. R., Jr., Hawley, S. H., Kraemer, J. R., Brueckner, G. E., Howard, R. A., Korendyke, C. M., Michels, D. J., Moulton, N. E., Socker, D. G., Schwenn, R., The

Green Line Corona and Its Relation to the Photospheric Magnetic Field., Astrophysical Journal, 485, 419, 1997

Wang, Y.-M., Two types of slow solar wind, Astrophysical Journal Letters, 437, L67, 1994

Warren, H. P., Mariska, J. T., Wilhelm, K., Observations of Doppler Shifts in a Solar Polar Coronal Hole, Astrophysical Journal Letters, 490, L187, 1997

Wiegelmann, T., Schindler, K., Neukirch, T., Helmet Streamers with Triple Structures: Simulations of resistive dynamics, Solar Physics, 191, 391, 2000

Wilhelm, K., Marsch, E., Dwivedi, B. N., Hassler, D. M., Lemaire, P., Gabriel, A. H., Huber, M. C. E., The Solar Corona above Polar Coronal Holes as Seen by SUMER on SOHO, Astrophysical Journal, 500, 1023, 1998

Wilhelm, K., Kalkofen, W., Observations of the upper solar chromosphere with SUMER., Astronomy and Astrophysics, 408, 1137, 2003

Wilhelm, K., Dwivedi, B. N., Teriaca, L., On the widths of the Mg X lines near 60 nm in the corona, Astronomy and Astrophysics, 415, 1133, 2004

Woo, R., Martin, J. M., Source regions of the slow solar wind, Geophysical Research Letters, 24, 2535, 1997

Wu, S. T., Wang, A. H., Plunkett, S. P., Michels, D. J., Evolution of Global-Scale Coronal Magnetic Field due to Magnetic Reconnection: The Formation of the Observed Blob Motion in the Coronal Streamer Belt., The Astrophysical Journal, 545, 1101, 2000

Zeeman, P., Winawer, B., The Magnetic Separation of Absorption Lines in Connection with Sun-Spot Spectra., Astrophysical Journal, 32, 329, 1910

Acknowledgements

Thanks in only a few lines, to all people, is easily the most difficult task, especially at the end the "thesis writing session". There were myriad people, who during the three years of my PhD, were near me, helping me in all the difficult moments (and there have been a lot of them!!).

My first thanks go to Rainer Schwenn, for his tremendous support all throughout the thesis. I was impressed by his clarity of thoughts (about everything!). A short discussion with him simplified, what for me, were seemingly complicated concepts. I was seriously trying to follow all his advices, but ….. my German…., surely I will learn it one day!

My second thesis advisor is Franz Kneer. I realize that the talks I gave in his group at the Göttingen Observatory enabled me to gain a lot of confidence in myself. Also his expert views during my thesis and on my report helped me gain insights into new things.

I owe a large part in the successful completion of my thesis to Luca Teriaca. His elaborate tutorials on spectral lines, data and error analysis were invaluable.

As can be seen from my thesis, IDL was the key language of programming I used. I thank Guillermo for giving me my first "friendly introduction" to IDL. He also taught me a lot about image processing, especially wavelets. He made the atmosphere more "noisy" in our, usually quiet office. Maybe he thought he had the a'trous algorithm at his disposal to denoise the noise he adds!!

I learnt a lot of things from Bernd Inhester, be it mathematical concepts, Fortran, or general physics. I cannot figure out if there is something on the planet he does not know. His ability to explain stuff and the freedom he gives the students at the Max Planck to approach him at any time is truly admirable.

Borut was here any time I needed him. There are times I disturbed him a bit too much, but he never complained. His thorough knowledge of the intricacies of operating systems and workings of the network made life a lot simpler.

I would like to thank David for the nice tutorial to Levenberg-Marquardt method.

There are many friends who helped me during this time. With Johanita and Racim, among the rare 3 to 4 year olds in Lindau, I had very nice moments, playing, laughing, and fighting. They made my stay in Lindau very pleasant.

Hebe, my office mate, was maybe the closest to me during this period. She helped me a lot with everything. I have to thank her also for the wonderful cakes I enjoyed during the parties and the dinners and for teaching me very nice Argentinian recipies.
My wonderful friends: Ana, Roopali, Laura (also my apartment mates) were there all the time, supporting me in all situations, be it academic or personal. The long and nice discussions did reduce my "Lindau damping".

Many thanks to my dear Indian friend Durgesh, who cooks authentic Indian food. He always makes the atmosphere more lively and entertaining with his jokes, laughter and frequent coffee breaks!!.

I want to thank the Matthews and Mecheris, two families who stayed in Lindau during my PhD, for their support and company.

Rajat, a strange guy, again from India they say, was …what can I say… "strange". He explained to me the ideas of theories ranging from chaos, cosmology, wavelets…to…information.

There are scores of other people, students and post-docs, whose names I have not mentioned here but with whom I have shared many cherishable moments, including a billion birthdays, parties and coffee breaks. All these things made the three years in the institute a wonderful one.

I would also like to thank Dieter Schmitt for all his help during this time and for the nice retreat weeks he organized. I learnt many details about the Sun, planets, cosmology, data analysis…. I would like to express my gratitude to the research school and Max-Planck-Institute for the financial support.

My highest and sincere gratitude goes to my parents and my brother. Without their help I would not be here. I would like to tell them, in Romanian: "Va multumesc foarte mult pentru ca ati fost alaturi de mine in toate momentele, bune sau rele, de pana acum."

My thanks go also to my teacher at the university, Mircea Russu and to my nice boss in the romanian Observatory: Georgeta Maris. They were the first to introduce me to the mysterious world of astrophysical dynamics.

I would like to thank the SOHO/LASCO/EIT consortium for providing the data and the software libraries. SOHO is a project of international cooperation between ESA and NASA. I acknowledge the use of data from the American-Japanese satellite Yohkoh. TRACE is a mission of the Stanford-Lockheed Institute for Space Research, and part of NASA Small Explorer program.

Publications and Contributions

Parts of the results of this thesis were taken from the following publications and conference contributions.

1. Publications

Mierla M., Schwenn R., Teriaca L., Stenborg G., Podlipnik B., Using LASCO C1 Spectroscopy for Coronal Diagnostics, Advances in Space Research, accepted

Tripathi D., Bothmer V., Solanki S. K., Schwenn R., *Mierla M.,* G. Stenborg, Plasma dynamics in prominence associated coronal mass ejection, Proceedings of IAU 223. St. Petersburg, Russia, 2004

Tripathi D., Bothmer V., Solanki S. K., Schwenn R., *Mierla M.*, Stenborg G., SoHO/EIT observation of a coronal inflow, Proceedings of IAU 226. Bejing, China, 2004

2. Conferences

Mierla M., Schwenn R., Stenborg G., Teriaca L., Podlipnik B., Dynamic properties of the solar corona: SOHO/LASCO observations, COSPAR, (COSPAR04-A-02275, D1.1-0066-04), 2004

Mierla M., Stenborg G., Schwenn R., Cobelli P., Podlipnik B., Towards unambiguous characterization of coronal structures: A new approach based on a wavelet packets equalization technique, EGS-AGU-EUG Joint Assembly, 2003 EAE03-A-04997, 2003

Mierla M., Schwenn R., Stenborg G., Inhester B., Podlipnik B., On a method to check the reliability of the wavelength calibration needed for spectral analysis of LASCO C1 data, LASCO/EIT Workshop, Birmingham, Anglia, 2002, oral presentation

Lebenslauf

Personliche Daten

Name:	Mierla
Vorame:	Marilena
Geburtsdatum	26.March 1977
Geburtsort	Targu-Carbunesti, Romania
Staatsangehörigkeit	Romanian

Schulbildung

1983 – 1987	Primary School Turburea, Gorj, Romania
1987 – 1991	General School, Turburea, Gorj, Romania
1991 – 1995	High School, Targu-Jiu, Gorj, Romania

Studium

1995 – 1999	Physics University, Bucharest, Romania
1999-2000	Master at Faculty of Mathematical, Physical and Natural Sciences, Turin University and Turin Observatory
Feb. 2002 - Jan. 2005	Stipendium des Max-Planck-Institut für Sonnensystemforschung

Berufstätigkeit

April 2001-February 2002	Assistant-researcher at Romanian Observatory, Bucharest